May 2020

The Materials Science and Engineering of Advanced YB-Doped Glasses and Fibers for High-Power Lasers

Thomas Wade Hawkins
Clemson University, twhawki@gmail.com

Recommended Citation

Hawkins, Thomas Wade, "The Materials Science and Engineering of Advanced YB-Doped Glasses and Fibers for High-Power Lasers" (2020). *All Dissertations*. 2585.
https://tigerprints.clemson.edu/all_dissertations/2585

THE MATERIALS SCIENCE AND ENGINEERING OF ADVANCED YB-DOPED GLASSES AND FIBERS FOR HIGH-POWER LASERS

A Dissertation
Presented to
the Graduate School of
Clemson University

In Partial Fulfillment
of the Requirements for the Degree
Doctor of Philosophy
Materials Science and Engineering

---

by
Thomas Wade Hawkins
May 2020

Accepted by:
Dr. Liang Dong, Committee Chair
Dr. John Ballato
Dr. Peter Dragic
Dr. Stephen Foulger
Dr. Philip Brown

ABSTRACT

This research studies and yields new understandings into the materials science and engineering of advanced multicomponent glass systems, which is critical for next generation fiber lasers operating at high output powers. This begins with the study and development of Yb-doped glasses in the Al_2O_3-P_2O_5-SiO_2 (APS) ternary system, fabricated using modified chemical vapor deposition (MCVD), that, despite being highly doped, possess an average refractive index matched to that of silica (SiO_2). The highly doped active core material was subsequently processed through a multiple stack-and-draw process to realize a single fiber with high doping, compositionally-tailored index, and scalability for fiber lasers. Based on the knowledge gained in this first focal area, further strategic compositional tailoring to influence the glass' photoelastic and thermo-optic coefficient, was performed in order to understand and realize significant decreases in Brillouin and thermal-Rayleigh scattering, which instigate parasitic stimulated Brillouin scattering (SBS) and transverse mode instabilities (TMI) in high power fiber lasers. In addition to understanding the composition / structure / properties of these glasses, a double-clad fiber laser will be fabricated, scaled to over 1 kW of output laser power, and studied in order to relate the materials science and engineering of multiple glass systems and fibers designs to laser performance and properties.

DEDICATION

This dissertation is dedicated to my wife Wendy and my son Wade. They are the foundation of solid support along this journey. Without her ability to encourage me to change perspectives when needed, refocus, and just sometimes stop to assess how fortunate I am, there is almost no chance this dissertation would have been written. This really is for the two of you, and I could not have finished this without the two of you in my life.

ACKNOWLEDGMENTS

I would like to acknowledge and give thanks to my advisor, Dr. Liang Dong on this research. He afforded me the opportunity to vary my research paths and focus on materials aspects of fiber laser research. More importantly, he encouraged me to engage further into the research that more clearly aligned with my focus and goals for deeper understanding as they reflect the materials.

I would also like to thank Dr. John Ballato for his guidance and mentorship on the writing process to create a compelling story with my research, as well as one that meets both the goals of a PhD in Materials Science and Engineering, but also one that aligns with our optical fiber understanding and fabrication strengths in the labs.

I'd like to thank my committee members, Dr. Peter Dragic, Dr. Stephen Foulger, and Dr. Phil Brown, for their time supporting and feedback on my research.

I want to thank both present and past group members that have been around through the course of my work on this dissertation. Pretty much all of you have already graduated and moved on to your own professional careers, but I thank you for your guidance and support on this work, even if it was just confidence that I would get it done.

Finally I would like to thank and acknowledge the Army Research Lab and Joint Technology Office for their financial support for this research.

TABLE OF CONTENTS

Table of Contents (Continued) Page

LIST OF TABLES

LIST OF FIGURES

Figure Page

CHAPTER ONE

HIGH-POWER FIBER LASERS: BACKGROUND, RARE EARTH PROPERTIES, AND OPTICAL NONLINEARITIES

1.1 Brief history of Optical Fibers

Optical fibers have been in existence for over fifty years. However, the concept of light-based communications has been around much longer, starting with Alexander Graham Bell in 1880 [1]. In that work, he reports the use of transmission of sound via sunlight (called the “photophone”).

Modern optical communications were built around the concept of using light to transfer bits of information over long distances. Starting with the work of Townes on the maser and progressing to the lasing with his and Schawlow’s work on an optical maser [2], in their research, infrared output was generated in an optical cavity.

After the pioneering work of Townes and Schawlow, Maiman created the first laser in a ruby crystal by pumping with a flash lamp. While a maser used a RF source to generate microwave output, the first laser used a flashlamp to stimulate the optical emissions [3]. Following Maiman’s work, which relied on a crystalline gain medium, Snitzer developed the first glass laser, a necessary predecessor to modern fiber lasers [4]. Using Neodymium (Nd) as the active rare earth dopant in a barium silicate glass, he was able to achieve the necessary population inversion of ions to lase in a narrow linewidth spectrum. The creation of these laser sources and their functionality was critical to the evolution of optical technology as we know it today. Charles Kao further enabled this evolution by defining the loss limits that materials need to achieve in order to build an effective medium for optical communications [5]. Kao and Hockham calculated the threshold of loss for a glass medium to be an effective waveguide at less than 20 dB/km. If purification of the glass could reach this level, optical fiber communications would be viable [6]. Today, for reasons that are discussed in the next section, losses in communication fibers are well below 0.18 dB/km [Record loss today ~ 0.14 dB/km: Tamura, et al., “The first 0.14-dB/km loss optical fiber and its impact on submarine transmission,” Journal of Lightwave Technology 36, 44 – 49 (2018).].

1.2 Optical Fiber Fabrication.

With Kao’s bar of < 20 dB/km, it was then a matter of creating the necessary processes that would yield the requisite high purity glass from which to make low loss optical fiber. The principal processes that led to these low loss glasses were Outside Vapor Deposition (OVD) at Corning and Modified Chemical Vapor Deposition (MCVD) at Corning and Bell Labs [7 – 10]. In the case of OVD, a high purity silica seed rod is rotated, and the high purity soot is deposited on the exterior. In the case of MCVD, the soot is deposited on the interior of a high purity substrate tube. In Figure 1.1, a cross section and graphical representation of the deposition process is shown.

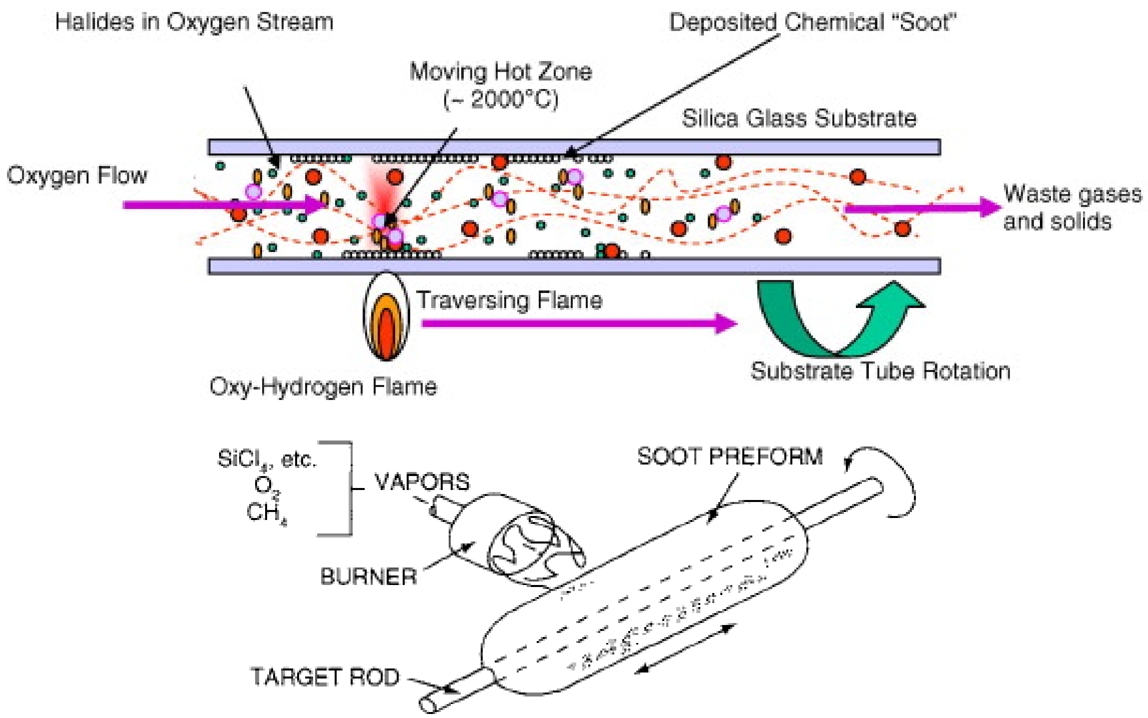

Figure 1.1: MCVD (top) and OVD (bottom) [11]

Prior to these vapor phase approaches, conventional glass batching and melting processes proved incapable of achieving low loss due to impurities. While both MCVD and OVD are different in how the soot is deposited, they share the same enabling chemistry, which is based on large vapor pressure differences between the glass precursors and those of impurities [12]. Standard chemical precursors for generating the glass soot (a fine, porous silica powder) for the core are silicon tetrachloride ($SiCl_4$), germanium tetrachloride ($GeCl_4$), and phosphorous oxychloride ($POCl_3$). The oxidation reactions for $SiCl_4$, $GeCl_4$ and $POCl_3$ are: [13]

$$\mathrm{SiCl_4(g) + O_2 \rightarrow SiO_2(s) + 2Cl_2}$$
$$\mathrm{GeCl_4(g) + O_2 \rightarrow GeO_2(s) + 2Cl_2}$$
$$\mathrm{2POCl_3(g) + \tfrac{3}{2}O_2 \rightarrow P_2O_5(s) + 3Cl_2}$$

Figure 1.2: Precursor oxidation reaction for Chemical Vapor Deposition

Each of the oxides formed in the above reactions are chosen for specific reasons associated with their contribution to the physical and optical properties of the resultant glass. SiO_2 is chosen as it provides superb glass-formation, high strength, and low optical loss. GeO_2 and P_2O_5 are both used to increase the refractive index of the glass relative to SiO_2, which is required for waveguiding via total internal reflection. However, their influence on optical and physical properties of the host glass are not the same, as is shown in later Chapters. These precursors possess high vapor pressures, which facilitate purification of the vapor stream since the most problematic impurities exhibit vapor pressures that are many orders of magnitude smaller; thus resulting in near-intrinsic glasses, hence intrinsically low loss [20]. Using these vapor deposition methods, transmission losses in conventional (telecommunication) fibers are now at 0.14 dB/km, a considerable improvement from the origins envisioned by Kao's original loss targets for a functional system [14, 76].

Fibers for communications generally are passive; i.e., their compositions are designed for carrying the light over very long distances. There are applications, such as fiber amplifiers and lasers, where the (core) glass composition is doped with a light-emissive (active) ions, such as a rare-earth. For such active fibers, rare earth doping level is generally high, which necessitates a more multicomponent glass composition than the germanosilicates used for communications fibers. Of particularly interest for laser fibers are glasses in the Al_2O_3-P_2O_5-SiO_2 alumino-phospho-silicates (APS) ternary system given their tolerance for Yb doping and a variety of other physical and optical characteristics that will be discussed later [8, 9, 12, 15]

In order to achieve the requisite refractive index and dopant levels with low levels of impurities in the glass, MCVD is an ideal fabrication tool [10]. Developed in the 1970's, this process utilizes high vapor pressure chemicals, heat, and oxygen to generate a high purity glass. The process begins with a high-quality silica (SiO_2) glass substrate tube. Oxygen (O_2) and Helium (He) are generally used as a carrier gas for the precursors and to improve thermal distribution within the tube, respectively. High purity chemical precursors such as $SiCl_4$, $GeCl_4$, and $POCl_3$ are combined with oxygen to create the oxide, which deposits onto the interior of the substrate tube (Figure 1.2). The soot is built up in layers to create the core of the preform, and the compositional profile is determined by the flows of precursors, speeds of the burner, and temperature. Once the core is deposited, it is still very porous, and it is ready to be doped with a rare earth solution to create the active core glass.

The most common method for doping rare earths into the porous glass soot is called "solution doping," and typically involves dissolving aluminum chloride ($AlCl_3$) and a rare earth salt (e.g., $YbCl_3$) in deionized water [16]. This solution is pumped into the substrate tube gradually and allowed to soak into the porous soot. For completeness, the purpose of the $AlCl_3$, which forms Al_2O_3 during further glass processing, is to lessen the immiscibility of lanthanide oxides in the SiO_2. The silica glass network does not intrinsically accommodate much rare earth dopants without appropriate glass modifiers [17].

Once glass is fabricated via MCVD, it must be drawn into fibers. A typical draw tower consists of a vertical structure with a high temperature furnace mounted to the exterior. Along with the furnace is a coating applicator, UV light source for curing the coating, as well as a series of guide wheels, a capstan, and take-up drum that allows for fiber collection. A typical draw tower configuration along with the draw tower at Clemson is shown in Figure 1.3.

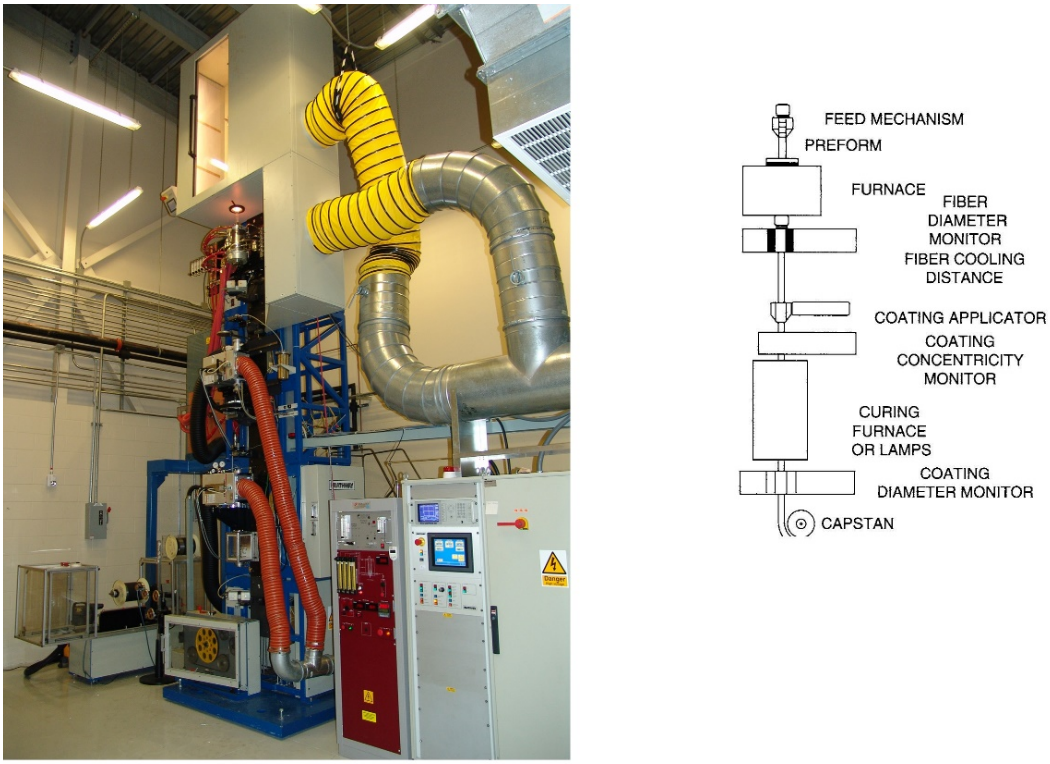

Figure 1.3: Clemson draw tower and typical tower layout [18]

1.3 Fiber Lasers

Snitzer is credited with pioneering fiber laser development in the 1960's and beyond. His earlier laser research using Nd glass indicated that amplification in a fiber was possible [19, 31]. His work, along with the reduced losses in the optical material itself, opened the door to creating new lasers using various rare earths that could be readily incorporated into the glass host.

Building on the foundational work of Townes (maser), Maiman (laser), Snitzer (glass laser), and Kao (optical fiber), there have been steady advances in optical fiber laser sources [2, 4, 5]. The modern fiber laser has integrated itself into a variety of applications, and it has in many ways become indispensable due to the size, power output, lifetimes, ease of use, and uniform fabrication methods. Some of the more prominent uses for fiber lasers are in defense, telecommunications, surgery, and industrial cutting [21, 54].

While applications continue to expand, so too are demands for higher output powers. This is especially the case in defense directed energy systems, which are driven by the need for speed-of-light munitions to counter a range of threats. However, at the requisite power levels, which exceed 1 kW (> 100 kW preferred), a host of otherwise weak optical nonlinearities limit performance. Of greatest consequence are Stimulated Brillouin Scattering (SBS), Stimulated Raman Scattering (SRS), and Transverse Mode Instability (TMI) [22 – 25]. For multi-kW systems, even a few percent reduction in these parasitic nonlinearities are worth the effort, as the increased power outputs and lifetimes of the fiber lasers justify the reduction.

To combat these limitations, the global fiber laser community generally has focused on complex fiber designs to improve performance, such as Large Mode Area fibers (LMA) with cores up to 50 microns as well as those that are low-moded [26 – 28]. Such designs have continued to increase the threshold powers at which the aforementioned parasitics arise. However, they can be further complemented with an optimized approach to core laser glass materials development.

1.4 Rare Earths for Fiber Lasers

1.4.1 Ytterbium Fiber Lasers

Most fiber lasers and amplifiers employ some form of RE doping to achieve gain. The most common methods of RE dopant inclusion is either solution doping, where a salt is dissolved in a liquid such as deionized water or methanol, or vapor phase where an aerosol chelate is incorporated into the core *in-situ* [16, 29, 30].

Most modern high-power fiber laser systems and research around them involve the use of trivalent ytterbium (Yb^{3+}) to achieve amplification and lasing. Modern commercial laser systems in excess of 100kW are now available using Yb as the active gain medium, which did not exist just 10 years ago [32 – 35].

A primary feature of the Yb as a major active dopant for high power (fiber) lasers is the simplicity of its energy level structure, as indicated in Figure 1.3. The principal Yb^{3+} energy levels are shown in Figure 1.3. Yb^{3+} possesses two main states that are of greatest interest to the high-power fiber laser community: the ${}^2F_{7/2}$ ground state and the

$^4F_{5/2}$ excited state. Absorption and emission between these levels occurs at a wavelength of about 1000 nm.

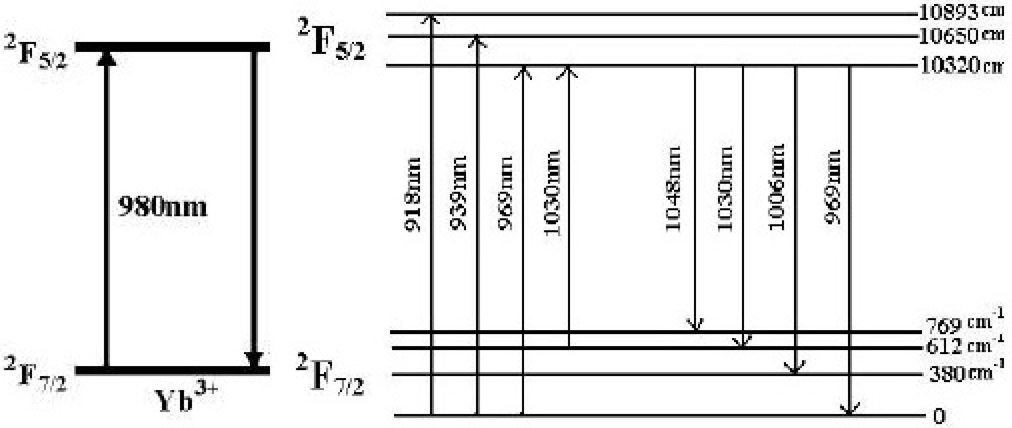

Figure 1.4: Energy level diagram of Yb^{3+} with Stark Levels [39] [40]

This simple two-level system acts as a quasi-3 level system given transitions between the Stark levels of the excited and ground states. Further, given this energy level structure, there would not be any excited state absorption and upconversion which reduce lasing efficiency in other dopant systems [20]. This lack of additional nearby energy levels allows for greater dopant concentrations to be used, which reduces the length of fiber required to achieve optimal lasing or amplification. This system also exhibits low quantum defects during operation, another added benefit in high-power regime as these defects lead to heating in the fiber, which decrease efficiency and maximum powers that can be achieved [36 – 38].

Other features that have led to the popularity of Yb^{3+} in high energy fiber laser systems also include the relatively large energy gap between the excited state and ground state to the phonon energy of the host glass and long upper state lifetime, which lead to high efficiency and also a relative ease of population inversion. The additional stark energy levels within the ${}^2F_{5/2}$ and ${}^2F_{7/2}$ enable absorption and lasing at multiple wavelengths.

1.4.2 Erbium Fiber Lasers

Erbium doped fibers are the cornerstone of long-haul optical fiber systems. They have matured since their creation, and have become a necessary component in modern systems due to their emission window overlapping the lowest loss wavelengths in silica optical fibers [41]. In this wavelength range of 1550nm, the silica host glass exhibits its lowest loss. This emission range is broad and enables a range of amplification that is suitable for wavelength division multiplexing (WDM), a feature that is vital to current communication networks. Typical emission ranges for Er amplifiers span approximately 1500 – 1600nm.

Unlike its counterpart of Yb, the Er energy level system contains numerous possible routes for upconversion and lasing. Much of the focus of the research into the material as a laser is at the 1550nm wavelength range. In this system, the output for high power lasing is from the ${}^4I_{13/2}$ – ${}^4I_{15/2}$ transition. Typically, the electron is excited to the higher ${}^4I_{11/2}$ level, where it nonradiatively decays to the lower level. The lasing emission is in the range of 1525-1575nm, depending on the host. In Figure 1.5, the Er, Yb, and Tm energy level diagrams are shown. Note much larger number of levels in Er compared to either that of the Yb or the Tm. [21]

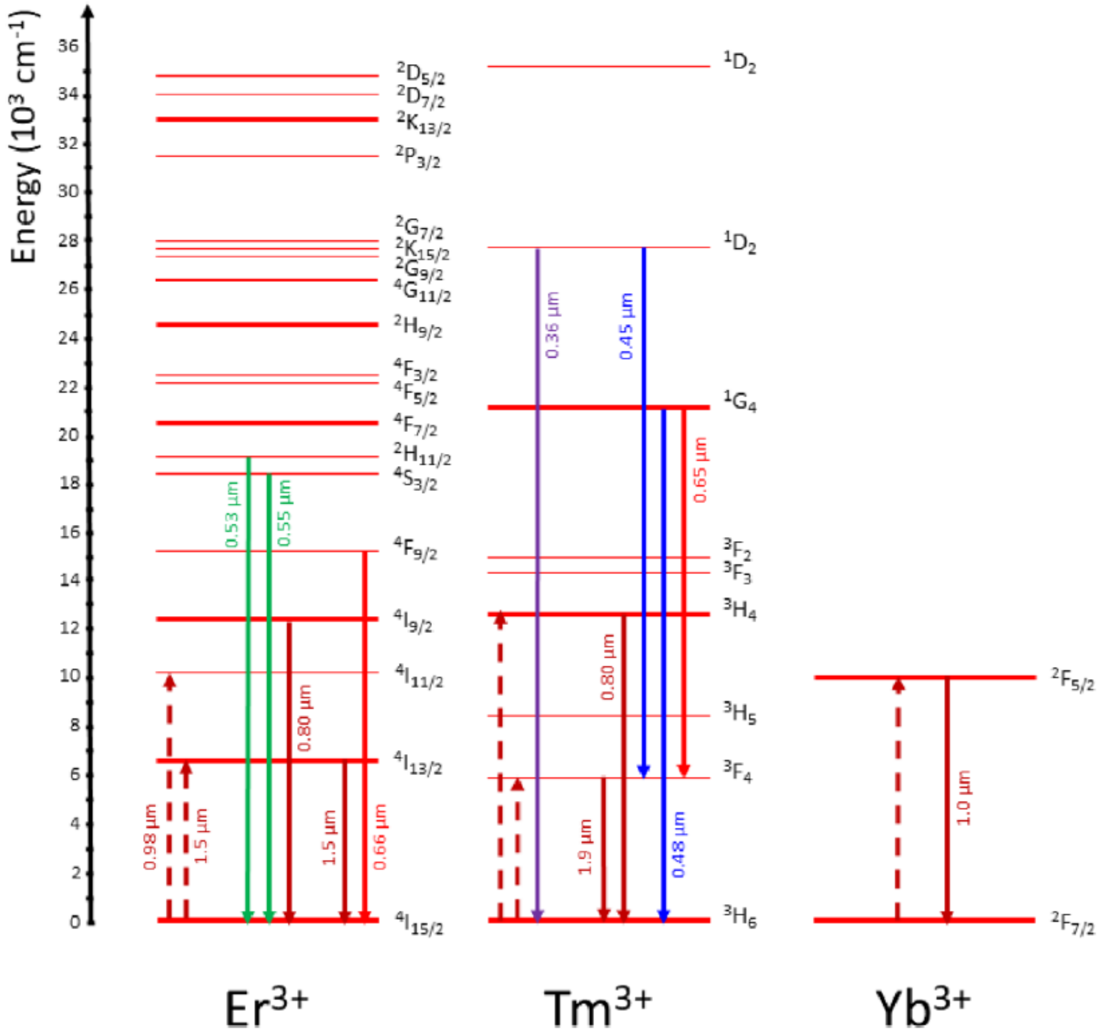

Figure 1.5: Rare Earth energy levels of Erbium, Thulium and Ytterbium [42]

Modern Er fiber lasers have not seen the success in high power scaling as their Yb doped counterparts. This is due to the lack of realization of the high efficiencies in these Er systems, making multi kW powers difficult to achieve. They also suffer from upconversion to higher energy levels other than the $^4I_{13/2}$ – $^4I_{15/2}$ which further reduces the efficiency and limits the output of erbium doped fiber lasers [20]. This effect often leads to unwanted emission in the visible wavelengths, or nonradiative relaxation in the form of excess heat. [42]

Erbium fiber laser systems can be improved in efficiency of lasing by incorporating Yb into the host glass. This co-doping of two RE ions increases the overall efficiency of the system. In a co-doped glass of Yb and Er, the incoming pump light excites the Yb up to the $^2F_{5/2}$. Due to the proximity of the Yb ions to those of the Er ions, provided they are in sufficiently high concentrations, an Yb ion excites an Er ion to the $^4I_{11/2}$ energy level, where it nonradiatively relaxes to $^4I_{13/2}$, then emits at 1550nm. This system increases power by allowing for higher power, more reliable pump light from 980nm sources to be used to lase at 1550nm [15, 43, 44]. In Figure 1.6, an example of this sensitization process is shown. This process of Yb and Er co-doping is fundamental to making high-power fiber lasers at 1550nm with these materials. However, while used for amplifiers and lower power laser systems, this is a less viable route for high power systems because of the heat generated as a result of the large quantum defect pumping at about 980 nm and lasing around 1550 nm.

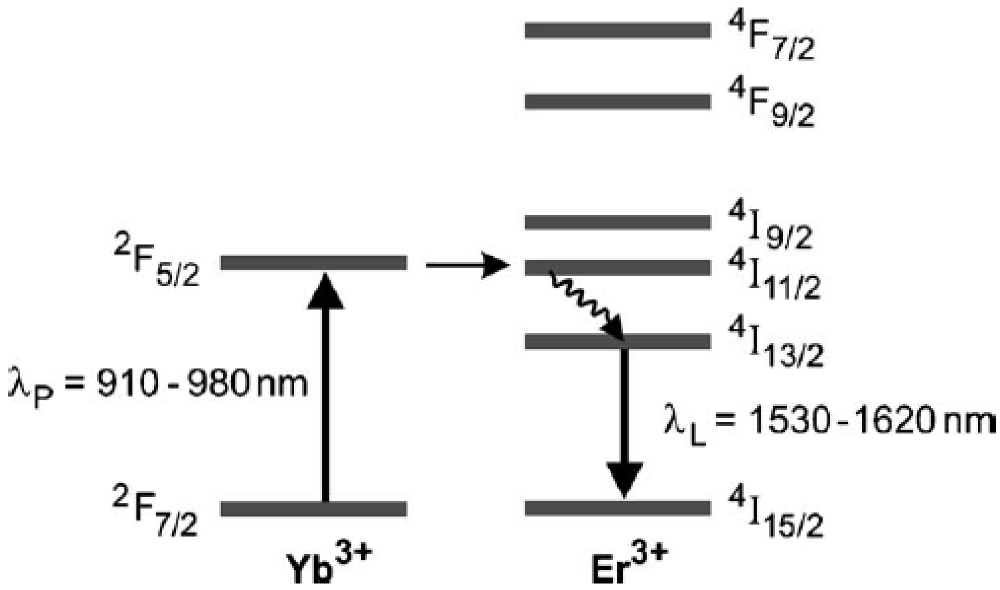

Figure 1.6: Energy level diagrams and energy transfer pathway for an Er-Yb codoped system [21]

1.4.3 Thulium and Holmium Fiber Lasers

Thus far the discussion of rare earths in fiber lasers has been in systems that most commonly operate at a wavelength below 2 μm. Ytterbium fiber lasers are the current standard for high power, narrow linewidth due to the simplicity of the energy level diagram and the availability of high brightness and low cost pump sources at approximately 1 μm. Erbium fiber lasers, while less powerful in terms of brightness and peak power, function well at 1.55 μm and are made accessible to the high-power and low cost pumps by co-doping with Yb. The Er systems are ideally suited for telecommunications due to the overlap of the output light to that of the lowest loss window for silica.

The next generation of high-power fiber laser research is focusing on the realization and power-scaling in the 2 μm spectral regime. This wavelength ranges from approximately 1.94 to 2.1 μm is attractive for a variety of applications. First it is considered “eye-safe” as they are within the 1.7-2.1 µm wavelength range. To be considered eye safe, the emission spectra exceeds 1.4 µm, which get absorbed by portions of the eye, specifically the cornea, and do not reach retina. However, eye safe does not prevent the laser from causing thermal damage. Merely that the wavelength range is out of the interaction range of the retina [77, 45]. This wavelength regime also has applications such as medical, LIDAR and welding of plastics, as well as free space communications for satellites. [46 – 48]

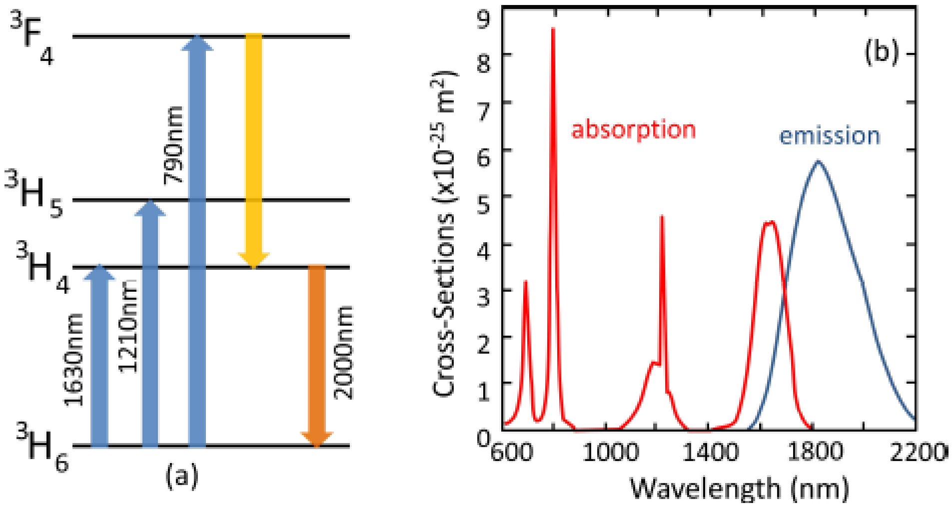

Figure 1.7: Energy level and absorption/emission diagram of Tm [49]

The energy level diagram for Tm^{3+} is shown in Figure 1.7. There are three potential wavelengths for pumping and one primary emission at 2 µm. The right-hand image of Fig. 1.7 provides the emission spectra, which is found to be spectrally broad, covering several hundred nanometers. There are two most common absorption bands for Tm at around 790nm and around 1600nm. The shorter wavelength overlaps common diodes that are commercially available, while the longer wavelength range can be effectively pumped with an Er fiber laser. [21] Both schemes will yield the 2 μm laser emission from the $^3H_4$ to $^3H_6$ energy transition.

The rare earth holmium (Ho) also exhibits emissions in the 2 μm regime, like that of Tm. Unlike Tm, however, there is no convenient pump wavelength available for diode sources. Due to the structure of the energy levels in Ho, there are fewer pumping schemes like those used in the other rare earths discussed here that will maximize power output and provide sufficient brightness. However, the mid IR emissions and pumping energy levels do coincide with the Tm emission.

In Figure 1.8, the energy level diagram for a co-doped Tm-Ho system and the emission spectra are shown. A Ho fiber laser can be configured using a pump source from the output light of a Tm fiber [51]. Further pumping and lasing can also be accomplished by co-doping the Tm and Ho, similar to the Er/Yb co-doping system (Figure 1,5) [52]. In this system, the Tm is doped into the silica host glass along with Ho in sufficient concentration to achieve sensitization. The Tm is pumped either with 790 or 1560nm light source, and it excites electrons up from the $^3H_6$ ground state. This transfers energy from the $^3H_4$ energy level in Tm to the $^5I_7$ level in Ho for the mid IR emission [53].

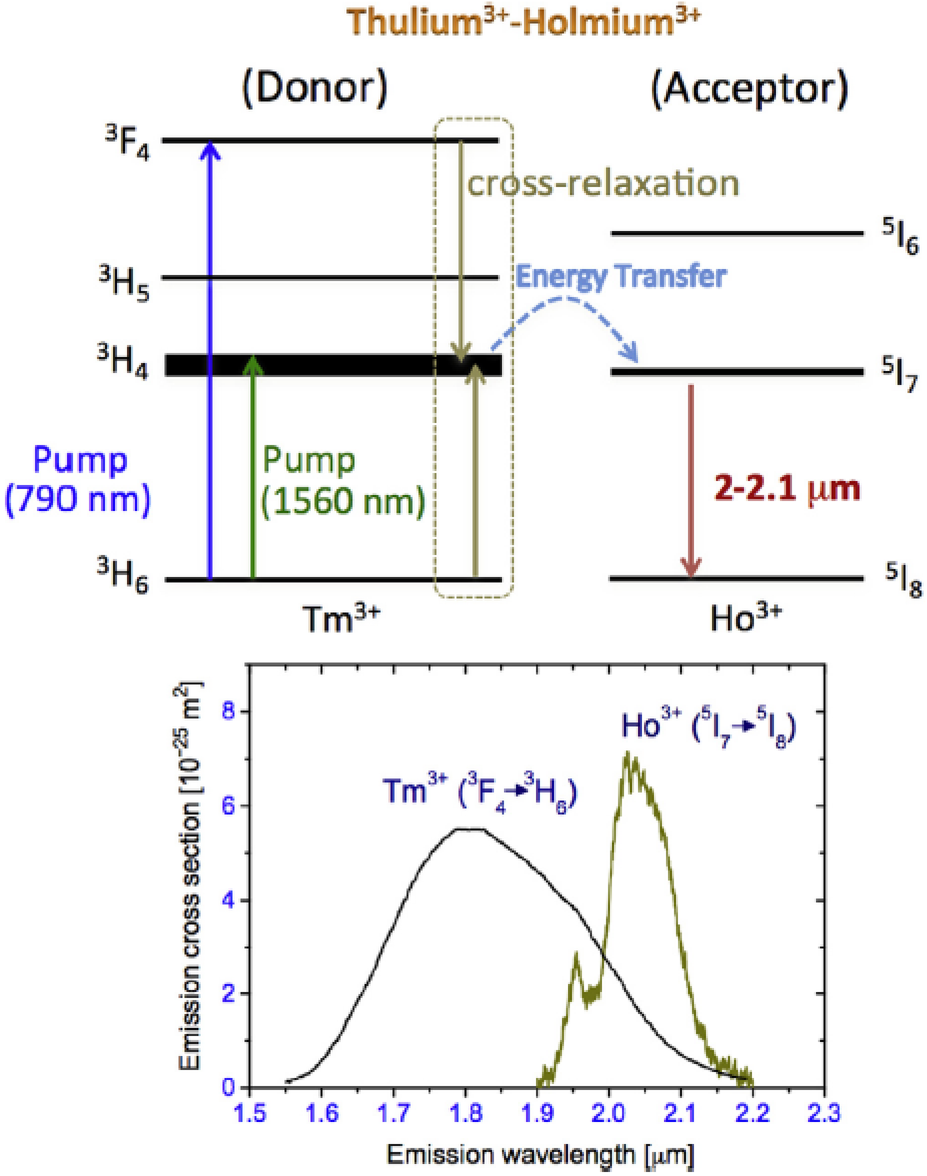

Figure 1.8: Tm and Ho energy level diagram in a co-doped system (upper) and emission spectra (lower) [50]

1.5 Optical Nonlinearities

1.5.1 Stimulated Brillouin Scattering (SBS)

Fiber lasers have enjoyed tremendous growth in applications such as manufacturing, defense, energy, and medical, including their use in particle accelerators and recent military deployment on the USS Ponce [54, 55]. However, the increased need to power-scale these systems has led to greater appreciation of nonlinearities as mechanisms which limit continued power-scaling. The two of most problematic optical nonlinearities given the power and linewidth of modern fiber lasers are Stimulated Brillouin Scattering (SBS) and Transverse Mode Instabilities (TMI) [56, 57, 58].

In its spontaneous form, Brillouin scattering is an interaction between the optical field (light) with thermally excited acoustic waves (phonons) of the glass. As optical power increases, the scattering reaches a threshold value whereby the acoustic wave is further enhanced by phase-matched transfer of power from the optical wave [23, 59]. In this now-stimulated case, interference between forward propagating and back scattering optical waves leads to periodic longitudinal density variations as power is further increased acting as an efficient reflector of the optical wave and limiting the output power achievable from the fiber laser. SBS has the lowest threshold of the parasitic nonlinearities in narrow linewidth system, such as fiber lasers [62].

Represented in Figure 1.9, in terms of physical and material properties, Brillouin gain coefficient (BGC) takes the form [60, 61].

$$\mathrm{BGC} = \frac{2\pi n^7 p_{12}^2}{c\lambda_0^2 \rho V_a \Delta\upsilon_B},$$

Figure 1.9: Equation for Brillouin Gain Coefficient [42]

where n is the refractive index (at free-space wavelength, λ_o), p_{12} is the transverse Pockels photoelastic coefficient, c is the speed of light (m/s), ρ is the density (kg/m^3), V_a

is the acoustic velocity (m/s), and $\Delta\nu_B$ is the Brillouin spectral linewidth (MHz), in Figure 1.9 [42].

A graphical illustration of SBS is shown in Figure 1.10. A backward-propagating optical wave is first generated by the forward-propagating optical wave reflecting off a thermally excited acoustic wave. The interference between the forward and backward propagating optical waves begins to enhance the acoustic wave, due to the photoelastic effect, traveling in the same direction as the propagation as power increases. In turn, the backward-propagating optical wave is further enhanced by more reflection off the acoustic wave. When these waves constructively interfere, i.e., they are phase matched, then the cycle yields stimulated Brillouin scattering in the fiber. This acousto-optic coupling can efficiently take energy away from the optical mode thus limiting power-scaling in the fiber laser.

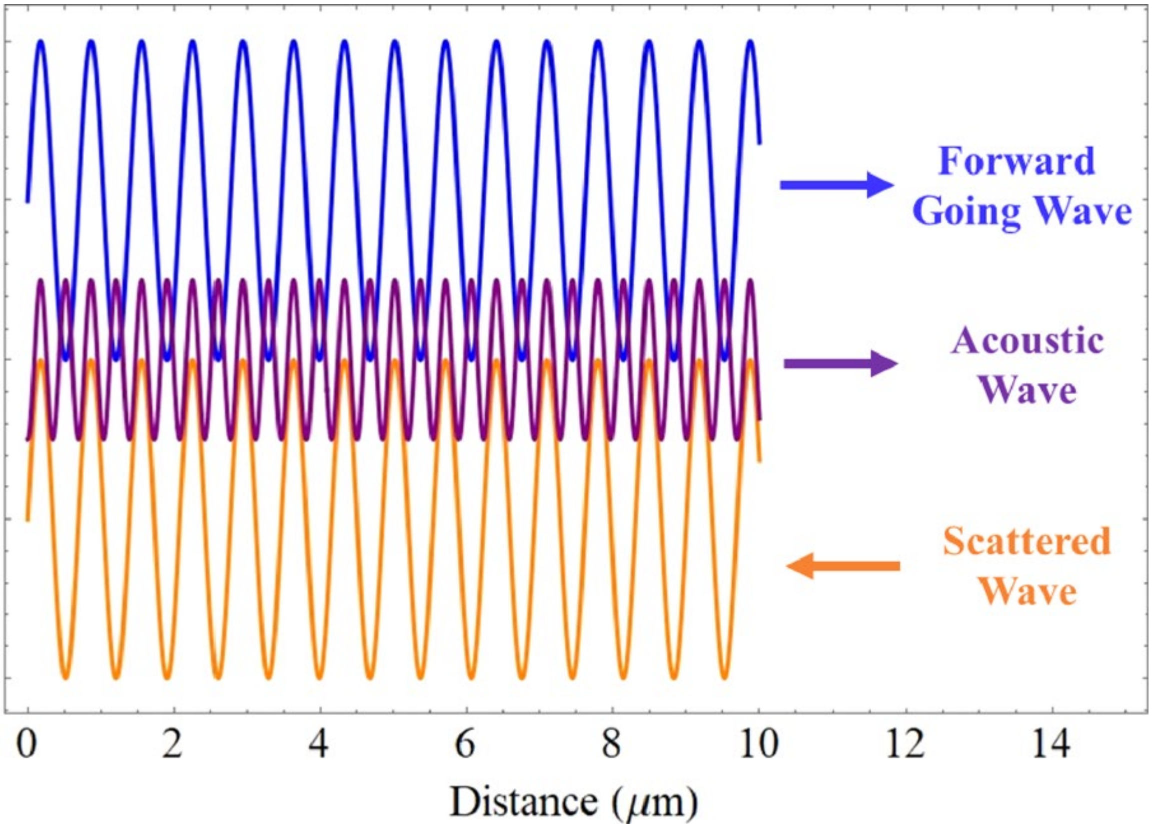

Figure 1.10: Schematic representation of stimulated Brillouin scattering (SBS) in a fiber; The optical wave (blue) travels down the fiber, creates and acoustic wave (purple) while then generates a scattered wave in the opposite direction (orange), limiting maximum power output. [42]

Materially, SBS, as well as TMI, is sufficiently complex that multiple constituents in the glass from which the fiber is made can either increase or decrease the thresholds of each. However, rarely does this work concurrently. When creating new materials for new fiber lasers, there must be trade-offs between the nonlinearities and how to compositionally address each. For example, it is possible to increase the Yb_2O_3 in a fiber laser glass by increasing doping concentration of the solution or Al_2O_3 content to improve the solubility [17]. This will have the effect of creating a new fiber laser that is shorter in length to achieve sufficient gain. A shorter fiber will have a higher SBS threshold because the overall gain depends on the gain coefficient and the interaction length, but a lower TMI threshold because the higher Yb content likely generates more heat per length of fiber. Accordingly, a tradeoff based on the material properties and desired characteristics of the fiber laser must be met [61 – 64].

The SBS threshold in which Brillouin Scattering occurs can be tailored materially in a variety of ways, and several of those are used in or related to this research. Both the refractive index and density of the material can be decreased and increased, respectively, reducing the BGC by compositionally tailoring the glass with changes to P_2O_5, Al_2O_3, or Yb2O3, for example. Each of these components influences acoustic velocity, Brillouin linewidth, and the transverse Pockels (photoelastic) coefficient in the material. It is, therefore, a matter of creating a new composition that achieves the lasing goal, while also sufficiently increasing the SBS threshold so that maximum power can be achieved in the fiber laser. Table I in Chapter 3 lists the property trends of these oxides and how they relate to various properties both physical and to the nonlinearities that affect fiber lasers.

1.5.2 Transverse Mode Instability (TMI)

TMI is another parasitic optical nonlinearity that limits power-scaling in high power fiber lasers. Both SBS and TMI arise from “mixed effects” in the material; i.e., coupling between optical, thermal, mechanical fields, etc. Whereas SBS is dependent upon the material’s photoelasticity (acousto-optics), modal instabilities in LMA fibers are, from a materials perspective, dominantly associated with the thermo-optic coefficient (dn/dT) [43]. TMI, along with SBS, have come to the forefront of power-limiting nonlinearities in high-power fiber laser systems. The phenomena were initially observed in a fiber laser in 2011 by Eidam, and has since become a key obstacle for power scaling in fiber laser systems [66 – 68].

TMI occurs in multimode waveguides, which all LMA fibers intrinsically are even when they are microstructured to be lossy to higher-order modes (HOMs). In these cases, light in the LP_{01} mode is coupled via the stimulated thermal Rayleigh scattering (STRS) into the other allowed modes, but this happens in a chaotic manner once some power threshold is met. Further increases in power in a fiber laser only increase this mode hopping instability, degrading beam quality, and preventing further high-power lasing. In Figure 1.11, the LP_{01} mode prior to TMI onset is shown on the left, where the area of greatest brightness is in (artificially colored) red. Once the TMI threshold is achieved, the modes hop between various HOMs, as in the right portion of the image. This illustrates the behavior of TMI once the mode propagation becomes dynamically changing during high-power beam guidance [60, 62]

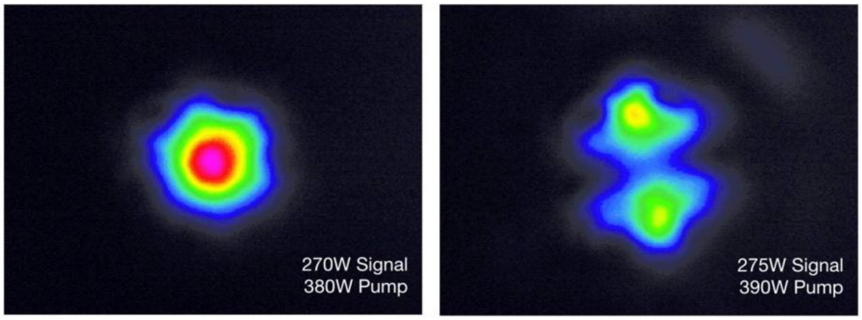

Figure 1.11: Image of modal guidance before (left) and after (right) the onset of TMI [66]

As noted, stimulated thermal Rayleigh scattering (STRS) is accepted as manifesting TMI in high power fiber lasers. TMI is a dynamic, thermally driven mode-hopping that arises when a grating is formed that phase-matches propagating modes of the incident and scattered light in large mode area (LMA) optical fibers (intrinsically multimode waveguides) that are lasing above a given threshold power [65].

Materially, the thermal nonlinearities associated with the accepted formalism is that the TMI threshold is proportional to $\rho \cdot c_p/(dn/dT)$ [61 – 64]. Additionally, the damping factor is proportional to the thermal conductivity and inversely so with heat capacity and density; though the dependencies of threshold and damping factor on heat capacity and density are different and so these factors do not cancel out. Of the factors that influence TMI, the thermo-optic coefficient, dn/dT, is most effectively tied to the properties of the materials itself. Thus, controlling the dn/dT will work to mitigate TMI and the threshold onset of the particular parasitic nonlinearity.

1.5.3 Photodarkening

Photodarkening is an effect where, in fiber, there is an increase in attenuation over time of operation. This increase in loss is thought to be the result of formation of color centers within the fiber over time [69]. This effect was especially prevalent in early Yb doped systems as powers increased in these fiber amplifiers and lasers. The linkage of the rate of effect was tied to the Yb concentration. As loss increased, so did the rate of photodarkening in a silica glass and output power decreased over time [70, 71]. While there is still debate on the intrinsic source of photodarkening, there are material improvements in fiber laser glass to reduce the overall effect.

Material mitigation of photodarkening in high-power fibers, particularly those doped with Yb, has shown significant success by the addition of P_2O_5 in the core during the vapor deposition process [72]. This is primarily thought to be associated with Yb doping in a P_2O_5 doped silica composition improves the solubility and ion to ion spacing between the RE ions. Further improvement in photodarkening is increased when Al_2O_3 is included, forming $AlPO_4$, and reducing Yb-Yb cooperative luminescence [42, 73]

Photodarkening has also been shown to be improved in fiber lasers with the addition of cerium (Ce^{3+}) in aluminosilicate systems [74]. In this process, the Ce acts to trap free electrons that might otherwise form color centers in Yb doped glass. These Ce^{+3} ions work to trap the otherwise hole-related color centers and mitigate the photodarkening in the fiber laser [75].

1.6 Purpose of this Dissertation

The primary goals of this Dissertation are to study and understand the fundamental composition / structure / property relationships in Yb-doped multicomponent silicate glasses used for high power fiber lasers. For these purposes, the host glass should exhibit low transmission loss and high lasing efficiency while also possessing low optical nonlinearities (specifically Brillouin scattering and mode instabilities). This research focuses on alumino-phospho-silicates (APS) and boro-alumino-phospho-silicates (BAPS) that are fabricated using conventional Modified Chemical Vapor Deposition (MCVD) methods. Of particular focus here is understanding the physical and chemical counter-play between component glass species and their impact on refractive index, glass stability, lasing performance, and optical nonlinearities.

This Dissertation takes two paths to the research presented within. First, we begin with creating a base glass composition to be used as the active medium in a high-power fiber laser. This ideal composition exhibits a variety of positive attributes that materially will make it an attractive option for a core in a fiber laser. This new material will contain SiO_2, P_2O_5, Al_2O_3, B_2O_3, $AlPO_4$, and Yb_2O_3 working together to create a highly doped, low photodarkening and compositionally stable glass with a refractive index difference, Δn, matched to that of silica. All these material constituents contribute to the robustness, ideal optical properties, and final lasing or amplification properties as a fiber laser core. This highly modified glass will exhibit low optical nonlinearities and efficient laser when used in a fiber laser design. Using rigorous characterization, both optically and compositionally, a series of preforms will be created with similar composition, dimension, and comparable refractive indices via MCVD. These preforms will then undergo stack and draw to combine the individual pieces into a single glass of which the minor differences in index or composition that would otherwise affect the pump light are mitigated.

The creation of this active core glass composition will become the foundation for new optical fibers that, materially, reduce the effect of optical nonlinearities in high-power fiber lasers, particularly that of SBS and TMI. In order to achieve this goal, a new preform will also be created via MCVD. This composition will be tailored to achieve a desired Δn, Yb_2O_3 doping concentration for sufficient lasing, and maximized amount of B_2O_3 within the glass to reduce the thermo-optic coefficient of the material (dn/dT) so that the TMI threshold is increased, as well as the SBS threshold. Using criteria for a commercial-off-the-shelf (COTS) fiber, this new glass will be tailored materially so that these effect from these parasitic nonlinearities will be mitigated. Further, the research will prove that this process is commercially scalable as standard MCVD and fiber draw processes will be used to create the preform and fiber. After the new preform is created, based on the optical and material properties, as well as modeling of the behavior of the dn/dT relative to the composition and B_2O_3 and Yb_2O_3 content, the glass will then be integrated into a commercial fiber design by a leading commercial manufacturer in of specialty fiber lasers. After the new fiber is created by the manufacturer, the new optical characteristics, such as SBS, refractive index, and power scaling, will be tested and measured to determine if this new fiber laser, and host core material, exhibits scalability up to 1 kW of power, and at the same time reduces the onset of these parasitic nonlinearities by creating a new material with tailored properties to mitigate them.

1.7 REFERENCES

1. A. G. Bell, “Selenium and the photophone”, *The Electrician*, 1880.
2. A. Schawlow, C. Townes, “Infrared and Optical Masers”, *Physical Review*, Vol. 112, No. 6, 1958.
3. T. H. Maiman, “Stimulated optical radiation in ruby”, *Nature* 187, 493-49 (1960).
4. E. Snitzer, “Optical Maser Action of Nd^{+3} in a Barium Crown Glass*”, Physical Review Letters*, Vol. 7, No. 12, 1961.
5. K. C. Kao and G. A. Hockham, “Dielectric-fibre surface waveguides for optical frequencies,” *Proc. Inst. Electr. Eng*., Vol. 113, no. 7, p. 1151, 1966.
6. J. Hecht, “The Remarkable Fiber Optic Vision of Charles Kao”, *Optics and Photonics News*, March 2019.
7. D. B. Keck, et al, U.S. Patent no. 3,737,292, 1974
8. J. B. MacChesney and P. B. O’Conner. “*Optical Fiber Fabrication and Resulting Products*”, US Patent #4,217,027, 1980
9. J. B. MacChesney “MCVD: Its origin and subsequent development,” *IEEE J. Sel. Topics Quant. Electron*ics, vol. 6, no. 6, pg 1305-1306 ,2000
10. J. B. MacChesney, P. B. O’Connor, F. V. DiMarcello, J. R. Simpson, and P. D. Lazay, “Preparation of low loss optical fibers using simultaneous vapor deposition and fusion”, *Proc. 10th Int’l Congress on glass*, pg 40 – 45, 1974.
11. A. Morrow, et al, Outside Vapor Deposition”, *Optical Fiber Communications*, Academic Press, 1985.

12. S. Nagel, J. B. MacChesney, K. Walker, "An Overview of the Modified Chemical Vapor Deposition (MCVD) Process and Performance", *IEEE Journal of Quantum Electronics*, Vol. QE-18, No. 4, pg 459 – 476, 1982.

13. K. Oh, U.-C. Paek, *Silica Optical Fiber Technology For Devices and Components*, John Wiley and Sons, 2012.

14. K. Schuster, S. Unger, C. Aichele, F. Lindner, S. Grimm, D. Litzkendorf, J. Kobelke, J. Bierlich, K. Wondraczek, and H. Bartelt, "Material and technology trends in fiber optics," *Advanced Optical Technology*, vol. 3, no. 4, pg. 447–468, 2014.

15. G. Vienne, J. Caplen, L. Dong, J. Minelly, J. Nilsson, and D. N. Payne, "Fabrication and Characterization of Yb^{3+} : Er^{3+} Phosphosilicate Fibers for Lasers", *Journal of Lightwave Technology*, Vol. 16, No. 11, pg 1990 - 2001 (1998)

16. J. E. Townsend, S. B. Poole, and D. N. Payne, "Solution-doping technique for fabrication of rare-earth-doped optical fibres", *Electronics Letters*, 23(7), pp.329-331 (1987).

17. J. Ballato and P. Dragic, "On the clustering of rare earth dopants in fiber lasers", *Journal of Directed Energy* 6, pg 175 – 181 (2017)

18. A. Mendez and T. F. Morse, *Specialty Optical Fibers Handbook*, Elsevier (2007

19. C. Koester and E. Snitzer, "Amplification in a Fiber Laser," *Applied Optics*, 3(10), 1182-1186 (1964).

20. L. Dong, B. Samson, *Fiber Lasers; Basics, Technology and Applications*, CRC Press, 2017.
21. D. J. Richardson, J. Nilsson, W. A. Clarkson, "High power fiber lasers: current status and future perspectives", J. Opt. Soc. Am. B, Vol. 27, No. 11, pg B63 – B92 (2010)
22. C. Jauregi, H.-J. Otto, S. Beietkoph, J. Limpert, and A. Tunnermann, "Optimizing high-power Yb-doped fiber amplifier system in the presence of transverse mode instabilities," *Optics Express*, Vol. 24, No. 8, pg 7879 – 7892 (2016)
23. R. G. Smith, "Optical Power Handling Capacity of Lowe Loss Optical Fibers at Sdetermined by Stimulated Raman and Brillouin Scattering," *Applied Optics*, Vol. 11, No. 11, pg 2489 - 2494 (1972)
24. C. Jauregi, H.-J. Otto, S. Beietkoph, J. Limpert, A. Tunnermann, "Optimizing the mode instability threshold of high-power fiber laser systems," *SPIE Proceedings,* Vol. 9728, pg 92780B1 – 92780B6 (2016)
25. L. Dong, F. Kong, G. Gu, T.W. Hawkins, M. Jones, J. Parsons, M.T. Kalichevsky-Dong, K. Saitoh, B. Pulford, and I. Dajani, "Large-Mode-Area All-Solid Photonic Bandgap Fibers for the Mitigation of Optical Nonlinearities," *Journal of Selected Topics Quantum Electronics*, Vol. 22, 4900207, pg 1 – 7 (2016)
26. F. Kong, C. Dunn, J. Parsons, M.T. Kalichevsky-Dong, T.W. Hawkins, M. Jones, and L. Dong, "Large-mode-area fibers operating near single-mode regime," *Optics Express* 24, 10295-10301 (2016).

27. F. Kong, G. Gu, T.W. Hawkins, J. Parsons, M. Jones, C. Dunn, M.T. Kalichevsky-Dong, K. Wei, B. Samson, and L. Dong, “Flat-top mode from a 50 μm-core Yb-doped leakage channel fiber,” *Optics Express*, Vol. 21, No. 26, pg 32371-32376 (2013).
28. G. Gu, F. Kong, T. Hawkins, J. Parsons, M. Jones, C. Dunn, M.T. Kalichevsky-Dong, K. Saitoh, and L. Dong, “Ytterbium-doped large-mode-area all-solid photonic bandgap fiber lasers,” *Optics Express*, Vol. 22, No. 11, pg 13962-13968 (2014).
29. S. Poole, D. Payne, M. Fermann, “Fabrication of low-loss optical fibres containing rare-earth ions”, *Electronics Letters*, Vol. 21, No. 17, 1985
30. M. Saha, A. Pal, M. Pal, C. Guha, R. Sen, “an Optimized Vapor Phase Doping Process to Fabricate Large Core Yb-Doped Fibers”, *Journal of Lightwave Technology*, Vol. 33, No. 17, 2015
31. E. Snitzer and R. Woodcock, “Yb^{3+}-Er^{3+} glass laser”, *Applied Physics Letters* 6, 45-46 (1966).
32. https://www.ipgphotonics.com/en/products/lasers/high-power-cw-fiber-lasers
33. Y. Jeong, J. K. Sahu, D. N. Payne, and J. Nilsson, “Ytterbium-doped large-core fiber laser with 1.36 kW continuous-wave output power,” *Optics Express* 12, 6088–6092 (2004).
34. J. Nilsson, S. Ramachandran, T. M. Shay, and A.Shirakawa, “High-power fiber lasers,” *IEEE Journal Select Topics Quantum Electron*ics. 15, 1–2 (2009).

35. Y. Jeong, A. J. Boyland, J. K. Sahu, S. Chung, J. Nilsson, and D. N. Payne, “Multi-kilowatt single-mode ytterbiumdoped large-core fiber laser,” *Journal Optical Society Korea* 13, 416–422 (2009)

36. G. Gu, Z. Liu, F. Kong, H. Tam, R. Shori, L. Dong, “High-Power efficient Yb-doped Fiber Laser with Low Quantum Defect”, *Workshop on Specialty Optical Fibers and Their Application*, WT2A.4 2015

37. R. Paschotta, J. Nilsson, A. Tropper, D. Hanna, “Ytterbium-doped fiber amplifiers”, *IEEE Journal of Quantum Electronics*, 33:1049-56

38. H. Pask, R. Carman, D. Hanna, C. Tropper “Ytterbium-doped silica fiber lasers: versatile sources for the 1 – 1.2 um region”, *IEEE Journal of Selected Topics in Quantum Electronics*, 1:2-13

39. S. Jetschke, S. Unger, A. Schwuchow, M. Leich, and J. Kirchhof, “Efficient Yb laser fibers with low photodarkening by optimization of the core composition,” *Optics Express*, vol. 16, no. 20, pg 15540-15545 (2008).

40. J. He, X. Liang, J. Li, H. Yu, “LD pumped Yb:LuAG Mode-Locked laser with 763 ps duration”, *Optics Express*, Vol. 17, No. 14, pg 11537 – 11542 (2009)

41. R. Mears, L. Reekie, I. Jauncey, D. Payne, “Low-Noise Erbium-doped Fibre Amplifier Operating at 1.54 μm”, *Electronic Letters*, 1987.

42. P. Dragic, M. Cavillon, J. Ballato, “Materials for optical fiber lasers: A review*”, Applied Physics Reviews*, 5, 041304, 2018.

43. J. Nilsson, W. A. Clarkson, R. Selvas, J. K. Sahu, P. W. Turner, S. U. Alam, and A. B. Grudinin, “High-power wavelength-tunable cladding-pumped rare-earth-

doped silica fiber lasers," *Opt. Fiber Technol*. **10**, 5–30 (2004).

44. J. D. Minelly, W. L. Barnes, R. I. Laming, P. R. Morkel, J. E. Townsend, S. G. Grubb, and D. N. Payne, "Diode-array pumping of Er3+/Yb3+ co-doped fibre lasers and amplifiers", *IEEE Photon. Technol. Lett.* **5**, 301–303 (1993).
45. N. Martinez, M. Velazquez, A. Umnikov, J. Sahu, "Highly efficient thulium-doped high-power laser fibers fabricated by MCVD", *Optics Express*, Vol. 27, No. 1, 2019.
46. P. Kadwani, R. Sims, J. Chia, F. Altat, L. Shah, and M. Richardson, "Atmospheric propagation testing using broadband thulium fiber systems*,"* *Advanced Optical Materials* (Optical Society of America, 2011)
47. V. Lemerg, D. D. Rozhetskin, and C. Jadczak, "Medium-power tissue ablation using 1940nm thulium fiber laser," *Journal of Biomedical Optics* (Optical Society of America, 2008)
48. Z. Xiaonong and J. Shibin,"2 micron fiber laser Enable versatile processing of plastics" *Application report in Industrial Laser Solutions*, (PennWell Corporation, 2016),
49. M. Zervas, C. Codemard, "High Power Fiber Lasers: A Review", *IEEE Journal of Selected Topics in Quantum Electronics*, Vol. 20, No. 5, 2014
50. D. Hudson, "Invited paper: Short pulse generation in mid-IR fiber lasers", *Optical Fiber Technology*, 20, 2014.
51. S. Jackson, "Mid IR Holmium Fiber Lasers", *IEEE Journal of Quantum Electronics*, Vol. 42, No. 2, 2006

52. Q. Wang, J. Geng, Z. Jiang, T. Luo, S. Jiang, “Mode locked Tm-Ho-codoped fiber”, *IEEE Photonics Technology Letters*, 23, 2011.
53. S. D. Jackson, A. Sabella, A. Hemming, S. Bennetts, and D. G. Lancaster, “High-power 83 W holmium-doped silicafiber laser operating with high beam quality,” *Optics Letters,* 32, 241–243 (2007).
54. V. Coffey, “High-energy lasers: New advances in defense applications”, *Optics and Photonics news*, pg 29 - 35 (2014)
55. T. Katsouleass, “Accelerator physics, Electrons hang ten on laser wake,” *Nature*, Vol. 431, pp 515-516 (2004)
56. A. Chraplyvy, “Limitation on Lighwave Communications Imposed by Optical-Fiber Nonlinearities”, *Journal Lighwave Technologies*, Vol. 8, No. 10, pg 1548 – 1557 (1990)
57. C. Robin, I. Dajani, B. Pulford, “Modal instability-supressing, single frequency photonic crystal fiber amplifier with 811 W output power”, *Optics Letters*, Vol. 39, no. 3, pg 666 – 669 (2014)
58. G. Agrawal, *Nonlinear Fiber Optics*, 3rd Edition, Academic Press, 2001
59. M. Cavillon, J. Furtick, C. Kucera, C. Ryan, M. Tuggle, M. Jones, T. Hawkins, P. Dragic, J. Ballato, “Brillouin Properties of a Novel Strontium Aluminosilicate Glass Optical Fiber”, *Journal of Lighwave Technology*, Vol. 34, No. 6, pg 1435 – 1441 (2016)
60. A. Smith and J. Smith “Mode instability in high power fiber amplifiers,” *Optics Express* 19, pg 10180 – 10192 (2011).

61. P. Dragic, M. Cavillon, A. Ballato, and J. Ballato, "A Unified Materials Approach to Mitigating Optical Nonlinearities in Optical Fiber. II. B. The Optical Fiber, Material Additivity and the Nonlinear Coefficients," *International Journal of Applied Glass Science* 9, pg 307 – 318 (2018).
62. J. Ballato, M. Cavillon, and P. D. Dragic, "A Unified Materials Approach to Mitigating Optical Nonlinearities in Optical Fiber. I. Thermodynamics of Optical Scattering" *International Journal of Applied Glass Science* 9, pg 263 – 277 (2018).
63. P. D. Dragic, M. Cavillon, A. Ballato, and J. Ballato, "A Unified Materials Approach to Mitigating Optical Nonlinearities in Optical Fiber. II. A. Material Additivity Models and Basic Glass Properties," *International Journal of Applied Glass Science* **9**, 278 – 287 (2018).
64. M. Cavillon, C. Kucera, T. Hawkins, J. Dawson, P. Dragic, J. Ballato, "A Unified Materials Approach to Mitigating Optical Nonlinearities in Optical Fiber. III. Canonical examples and materials road map," *International Journal of Applied Glass Science* **9**, 447 - 470 (2018).
65. L. Dong "Stimulated thermal Rayleigh scattering in optical fibers," *Optics Express* 21, pg 2642 – 2656 (2013).
66. T. Eidam, C. Wirth, C. Jauregui, F. Stutzki, F. Jansen, H. Otto, O. Schmidt, T. Schreiber, J. Limpert, A. Tunnerman, "Ecperimental obersvations of the threshold-like onset of mode instabilities in high power fiber amplifiers", *Optics Express*, 2011.

67. E. Snitzer, "Cylindrical Dielectric Waveguide Modes", *Journal of the Optical Society of America,* Vol. 51, No. 5, 1961

68. E. Snitzer, H. Osterberg, "Observed Dielectric Waveguide Modes in the Visible Spectrum", *Journal of the Optical Society of America*, Vol. 51, No. 5, 1961

69. R. Paschotta, J. Nilsson, P. Barber, J. Caplen, A. Tropper, D. Hanna, "Lifetime quenching in Yb-doped fibres", *Optics Communications*, 1997

70. J. Koponen, M. Söderlund, S. Tammela, and H. Po, "Photodarkening in ytterbium-doped silica fibers," *Proceedings of the SPIE*, vol. 5990, pg599008-1 – 599008-12 (2005).

71. S. Jetschke, S. Unger, U. Röpke, and J. Kirchhof, "Photodarkening in Yb doped fibers: experimental evidence of equilibrium states depending on the pump power," *Optics Express* 15, 14838-14843 (2007).

72. S. Suzuki, H. McKay, X. Peng, L. Fu, L. Dong, "Highly ytterbium-doped silica fibers with low photo-darkening", *Optics Express*, 2009

73. S. Jetschke, S. Unger, A. Schwuchow, M. Leich, and J. Kirchhof, "Efficient Yb laser fiber siwth low photodarkening by optimization of the core composition", *Optics Express* 16, 15540 (2008).

74. M. Engholm, P. Jelger, F. Laurell, L. Norin, "Improved photodarkening resistivity in ytterbium-doped fibe lasers by cerium codoping", *Optics Letters*, 2009.

75. M. Engholm, L. Norin, "Preventing photodarkening in ytterbium-doped high power fiber lasers; correlation to the Uv-transparency of the core glass", *Optics Express*, 2008

76. Y. Tamura, H. Sakuma, K. Moriata, M. Suzuki, Y. Yamamoto, K. Shimada, Y. Honma, K. Sohma, T. Fukii, T. Hasegawa, “The First 0.14-dB/km loss Optical Fiber and its Impact on Submarine Transmission”, *IEEE Journal of Lighwave* Technology, Vol. 36, No. 1, 2018.
77. J. Franks, "What is eye safe?," *Proceedings SPIE 1419, Eyesafe Lasers: Components, Systems, and Applications,* (1 April 1991)

CHAPTER TWO

EXPERIMENTAL

2.1 Introduction

This chapter details the processes involved in first formulating, then fabricating, and, finally, optimizing the active glasses, preforms, and fibers used for this Dissertation. As will be seen, this is a highly iterative and multi-dimensional set of considerations that need to be met in order to achieve the desired laser performance as described in Chapter 1. Since this Dissertation is focused on the enabling and underlying materials science and engineering of said advanced fibers, this Section will be limited to materials (glass, preform, and fiber) syntheses and characterization. Specific laser-related testing and materials development, while cited in the Results Chapters, are not detailed here as they have been thoroughly described elsewhere [1, 2].

2.2 MCVD preform fabrication

As a brief reminder, Chapter 1 described the state-of-the-art in high power fibers lasers. Also described was how the scaling of fiber lasers to higher output optical powers is limited by a series of nonlinearities. The fibers employed in this Dissertation, as tools to better understand the enabling materials science and engineering, are conceptualized to mitigate these parasitic nonlinearities through a combination of two complementary effects: (a) waveguide design and (b) material composition, hence structure and properties. Indeed the light propagating down an optical fiber is influenced by both of these effects since the waveguide design defines the modal aspects of the light (e.g., which modes propagate and their relative gain / loss characteristics) whereas the material composition defines the intrinsic gain coefficients and spectral widths for lasing and the nonlinearities. In both cases, the principal material requirements are (a) a specific average refractive index profile (despite being a highly multicomponent glass) and (b) optimized doping levels for both the active Yb species and for the glass components used to tailor the refractive index and reduce the nonlinear gain coefficients (e.g., Brillouin gain coefficient, BGC, or thermo-optic coefficient, TOC = dn/dT).

In order to achieve the requisite average refractive index and dopant levels with low levels of impurities in the glass, the Modified Chemical Vapor Deposition (MCVD) process was used to fabricate the active core glass [3]. Developed in the 1970's, this process utilizes high vapor pressure chemicals, heat, and oxygen to generate a high purity glass that is suitable for low light transmission losses. The process begins with a high-quality silica (SiO_2) glass substrate tube. Oxygen (O_2) and Helium (He) are used as a carrier gas for the precursors and to improve thermal distribution within the tube, respectively. Standard chemical precursors for generating the glass soot (a fine, porous silica powder) for the core are silicon tetrachloride ($SiCl_4$), germanium tetrachloride ($GeCl_4$), and phosphorous oxychloride ($POCl_3$). The oxidation reactions for $SiCl_4$, $GeCl_4$ and $POCl_3$ are: [4]

$$\mathrm{SiCl_4(g) + O_2 \rightarrow SiO_2(s) + 2Cl_2} \qquad \text{Eqn. 1}$$

$$\mathrm{GeCl_4(g) + O_2 \rightarrow GeO_2(s) + 2Cl_2} \qquad \text{Eqn. 2}$$

$$\mathrm{2POCl_3(g) + \tfrac{3}{2}O_2 \rightarrow P_2O_5(s) + 3Cl_2} \qquad \text{Eqn. 3}$$

Each of the oxides formed in the above reactions are chosen for specific reasons due to their contributions to the physical and optical properties of the resultant glass. SiO_2 is chosen as it is identical to the substrate tube material and provides compatibility, strength, and low loss. GeO_2 and P_2O_5 are both used to increase the refractive index of the glass relative to SiO_2. However, their influence on the host-glass optical and physical properties are not the same. The purpose of this research does not include study of GeO_2 behavior in the active glass development. Additionally, it is well researched and numerous sources can be found for further education on its behavior in SiO_2. In this research, the behavior of P_2O_5 in SiO_2 is further explored in this Chapter and in the subsequent materials and engineering Chapters.

The precursor liquids (e.g., $SiCl_4$ or $POCl_3$) are heated to 35°C as O_2 bubbles through. This combination of O_2 and precursor vapor flow through the interior of the substrate tube as a H_2 and O_2-fueled burner passes along the exterior of the tube. Figure 2.1 is a basic diagram of MCVD deposition process. Precursors are passed through the tube interior as the burner traverses while the substrate tube rotates. Each pass of the burner will yield a single layer of deposited glass. All layers of deposition except the core layer(s) are fully sintered into transparent glass. The core is not fully sintered and, therefore, remains porous (“soot”), as it is then to be doped with a rare earth salt solution in order to create the active core glass. Before doping, the entire substrate is removed from the MCVD lathe and mounted vertically for solution doping.

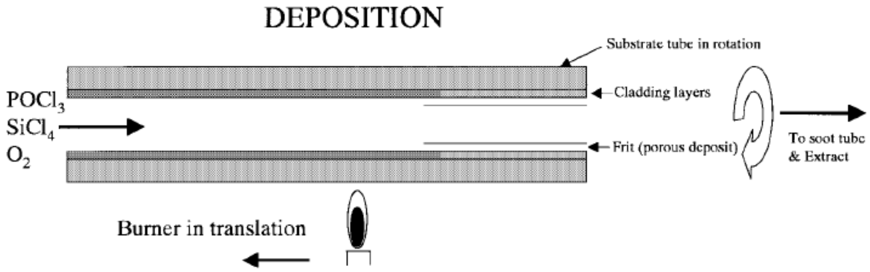

Figure 2.1: Diagram of core deposition in MCVD. [5]

The most common method for doping rare earths into the glass soot is called "solution doping" [6]. It typically involves combining aluminum chloride ($AlCl_3$) and a rare earth salt in deionized water and dissolving them fully into the solution. Many rare earth salts can be used for solution doping, but, for this work, ytterbium chloride ($YbCl_3$) is chosen as understanding and advancing the materials science and engineering of ytterbium (Yb) fiber lasers are goals of this Dissertation. The concentrations of $AlCl_3$ and $YbCl_3$ are initially determined by calculation of the target molar concentration in the glass. It is common practice to create a solution, dope the glass, evaluate the composition via SEM, and then change the amounts of $AlCl_3$ or $YbCl_3$ on subsequent preforms if the initial concentrations are not met. The fully mixed solution is pumped into the substrate tube gradually and allowed to soak for a minimum of one hour. For completeness, the purpose of the $AlCl_3$, which forms Al_2O_3 during further glass processing, is to facilitate "solubility" of the active Yb_2O_3 in the SiO_2. The silica glass network does not intrinsically accommodate much rare earth dopants without appropriate modifiers [7].

Once the soak time has expired after 60 minutes, the substrate tube is drained of the doping solution. It is dried under a 5 liter per minute (lpm) purge of nitrogen (N_2) overnight. After drying, the tube is reattached and remounted onto the MCVD lathe. The next steps of fabrication are to dry the doped soot layer, sinter it into a transparent glass, and consolidate the tube into a rod. The sintering process begins by preheating the glass through a series of drying steps that gradually increase the temperature and continue to eliminate moisture from the core soot layer. As the burner is traversing, He and O_2 are flowed through the tube, and the H_2 and O_2 of the burner fuel flows are ramped with each new series of passes along the outside of it.

Once the substrate tube is sufficiently warm and the interior moisture has been fully removed, the burner increases to the target sintering temperature of 1750ºC for one traverse pass along the length of the substrate tube at approximately 35 mm/min. This reduces the porosity of the core soot layer and fuses it to the substrate tube. After the sintering pass, the burner temperature is increased to approximately 2400ºC and the traverse speed is reduced to approximately 20 mm/min. This collapse pass is the first of three that begin to reduce the structure of the substrate tube to a rod. The final consolidation pass is at approximately 12 mm/min and closes the interior of the tube fully to a rod. After the final consolidation pass, the tube is separated manually using a handheld H_2/O_2 torch and allowed to cool fully before further testing and fabrication.

2.3 MCVD preform fabrication at Clemson

The MCVD lathe system at Clemson University was used for all preform fabrication discussed in this Dissertation [8]. Bespoke glass working is used to attach the substrate tube for preform fabrication. All process gases (e.g., $SiCl_4$, $POCl_3$, O_2) are introduced through a custom rotary union that is sealed and purged. Heat is applied externally via a jacket-cooled hydrogen-oxygen flame source. The Clemson lathe is computer controlled via discrete process steps that are programmed into a “recipe” that is interpreted by the machine programmable logic controls (PLC) as discrete motor and gas flow steps. When the recipe is initialized, system safety checks are performed, and the process is then started. All run steps, including burner temperature, gas flows, and speeds are pre-programmed and automatically controlled once the recipe has been initialized. Figure 2.2 shows the primary lathe bed system, and the headstock and tailstock positions are labeled for locational reference.

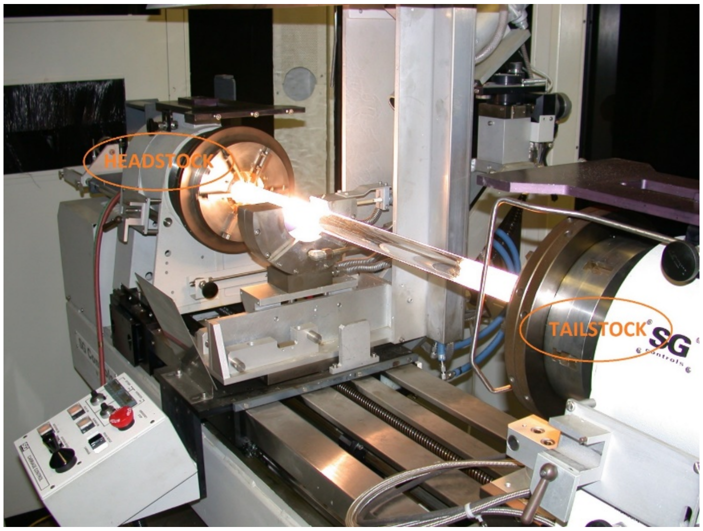

Figure 2.2 Principal lathe bed with headstock and tailstock direction labels [8]

The initial step for preform fabrication is tube preparation. The substrate tube is heated externally to 2100°C while O_2 and He flow within the tube at approximately 1000 standard cubic centimeters per minute (sccm) each. After preheat, the interior surface of the tube is etched. This reduces imperfections within the tube interior and provides a pristine surface to deposit the cladding and core layers. A mixture of freon (C_4F_8) and sulfur hexafluoride (SF_6) are introduced along with O_2 and He as etchants. At the temp of 2100°C these fluorinated gases etch and remove silica from the tube interior [9]. After etching, the C_4F_8 and SF_6 are purged from the tube. Finally, a clear and polish pass is completed after etching. This removes any unwanted etching gases, as well as any surface imperfections inside the tube by reheating it and. The clearing pass is completed at 2200°C. Once completed, the tube is ready for cladding and core deposition. Equation 4 provides the chemical reaction for etching using carbon tetrachloride and silica are noted here as an example. This mechanism is almost identical to the freon etching used in this Dissertation.

$$\mathrm{CF_4(g)} + \frac{3}{2}\mathrm{SiO_2(s)} \rightarrow \frac{3}{2}\mathrm{SiF_4(g)} + \mathrm{CO_2(g)} + \frac{1}{2}\mathrm{O_2(g)} \qquad \text{Eqn. 4}$$

[4]

In each case treated in this Dissertation, there are a total of five layers of cladding glass deposited prior to core deposition. These cladding layers are created by flowing silicon tetrachloride ($SiCl_4$) and phosphorous oxychloride ($POCl_3$), which react and deposit a phosphosilicate (SiO_2:P_2O_5) glass. These layers are deposited while the burner is traversing left to right from headstock to tailstock (Figure 2.2). This is considered the forward direction. The elevated burner temperature of 2100°C fully sinters the soot as it reacts and deposits. Once the five layers are deposited, the burner temperature is reduced to 1750°C. The $POCl_3$ flows are increased to maximum at 1500 sccm and $SiCl_4$ to approximately 1000 sccm. These conditions are optimal for core deposition.

Unlike the cladding passes, the core deposition pass is generated in the reverse direction. The burner starts at the tailstock side of the lathe and moves right to left in the opposite direction of the precursor gas flows [5]. This reverse pass allows for a thicker soot that is more uniform, which will ultimately lead to a larger and more uniform core region. Prior to core deposition, the process is delayed while the tube is cooled from the clad deposition process and the appropriate precursor flows for the core to begin. This promotes an optimal environment inside the tube for soot generation with a high concentration of P_2O_5. This delay and tube filling process is assumed to be beneficial based on past MCVD fabrication experience, although no testing has been completed to evaluate the difference. The burner, when it reaches the end of its traverse distance at the tailstock, heats to a 1750°C and moves at 12mm/minute in the reverse (R to L) direction. The core is deposited as the burner moves. This process continues until the burner reaches the start position at the headstock.

After the core is deposited, the soot layer is too soft to be removed from the lathe and solution doped. It will not adhere to the substrate tube wall and fall off when exposed to a doping solution without an optimized presinter step, which increases the density and promotes adhesion to the tube wall [5]. This single pass of the burner at approximately 1200°C sufficiently reduces the density of the core soot so the rare earth solution can be introduced without the entire soot layer releasing from the tube interior. The preform is then readied for solution doping by removal from the lathe after it has cooled.

A solution of the desired concentration $AlCl_3$, $YbCl_3$, and H_2O are mixed and pumped into the substrate tube with the newly deposited core. The $AlCl_3$ and $YbCl_3$ used in the solutions are approximately 18 and 33 grams per 250 grams of water, respectively. Both the $AlCl_3$ and $YbCl_3$ are of at least 99.999% purity. Deionized water is measured out and added to a flask with a stir bar. The $AlCl_3$ is added and allowed to dissolve, followed by the $YbCl_3$. A solution is used up to 10 times before discarding. As with the halide sources for SiO_2, B_2O_3, and P_2O_5, the $AlCl_3$ and $YbCl_3$ precursors will ultimately oxidize during preform fabrication yielding Al_2O_3 and Yb_2O_3. The target concentrations of Al and Yb varied for each development phase, and they are discussed in further detail during the Materials Engineering Chapter of this Dissertation.

The substrate tube is mounted vertically in a stand after removal from the lathe. Using a peristaltic pump, custom cap, and tygon tubing, the tube is filled with solution gradually, so it does not disturb the soot layer. Once filled, the pump is stopped, and the solution is allowed to fully saturate the soot for at least 60 minutes. After this length of time, the pump is reversed, and the tube is drained and allowed to dry overnight under a nitrogen purge of 5 lpm. The solution is saved for additional usage as needed.

After doping and drying overnight, the second phase of MCVD preform fabrication can begin. A series of gas flows, burner passes, and temperatures are used to reduce the ID and OD of the tube to a solid rod. Additional precursor gases are used to change the index, as well as maintain the P_2O_5 content within the core glass. In Figure 2.3, the MCVD fabrication process as a function of temperature versus time is plotted. The principal stages of fabrication are indicated, including cladding and core deposition, sintering, and consolidation and collapse.

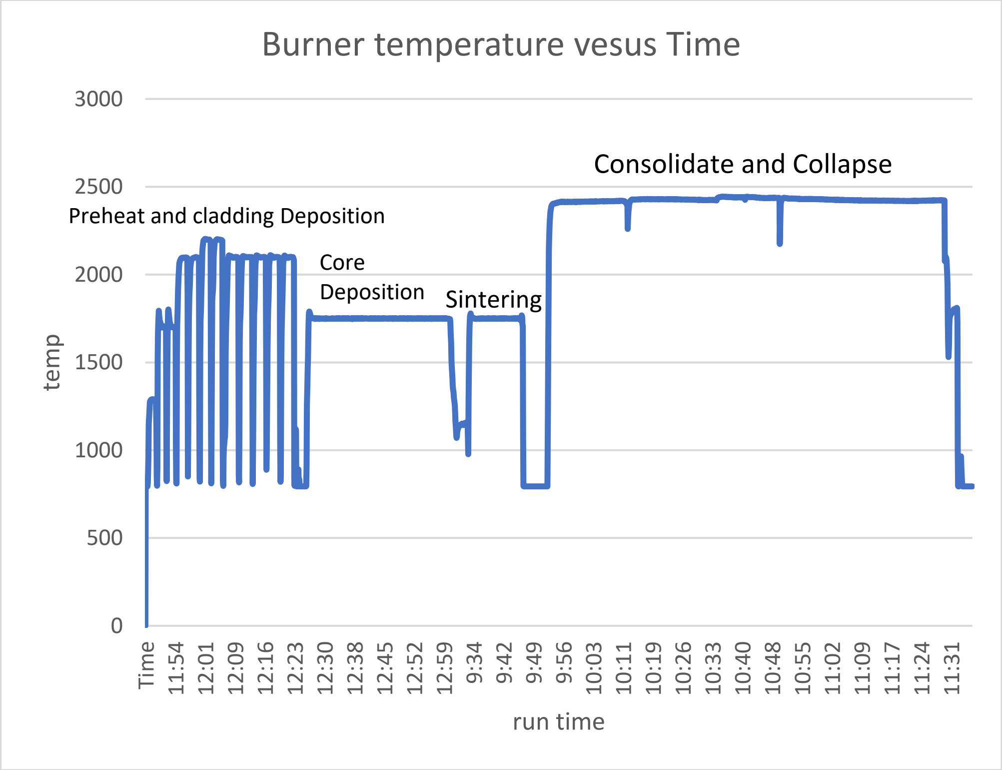

Figure 2.3: MCVD temperature (in °C) versus time

Using bespoke glass-working, the substrate tube with dried and doped core is reattached to the tailstock and exhaust tube on the MCVD lathe. A slow drying and gradual heating process is used to ensure any residual moisture in the soot is removed before consolidation and collapse, but any water is driven out of the soot slowly so as not to disturb it. This drying process is performed with the pilot portion of the burner on, which is the lowest possible combination of H_2 and O_2 flows. A total of 40 drying passes are completed before the sintering pass. After drying, the soot layer is sintered fully to remove remaining porosity. During the sintering pass, BCl_3 is introduced, which ultimately oxidizes at the high processing temperatures to form B_2O_3. It is used to reduce the final refractive index of the core to the desired target, to achieve a flat differential refractive index (Δn) profile relative to silica, and reduces the Brillouin gain coefficient of the glass. The B_2O_3 in the glass also reduces the index as is shown in Figure 2.4 the oxidation reaction for BCl_3 to B_2O_3 is in Equation 5 [10].

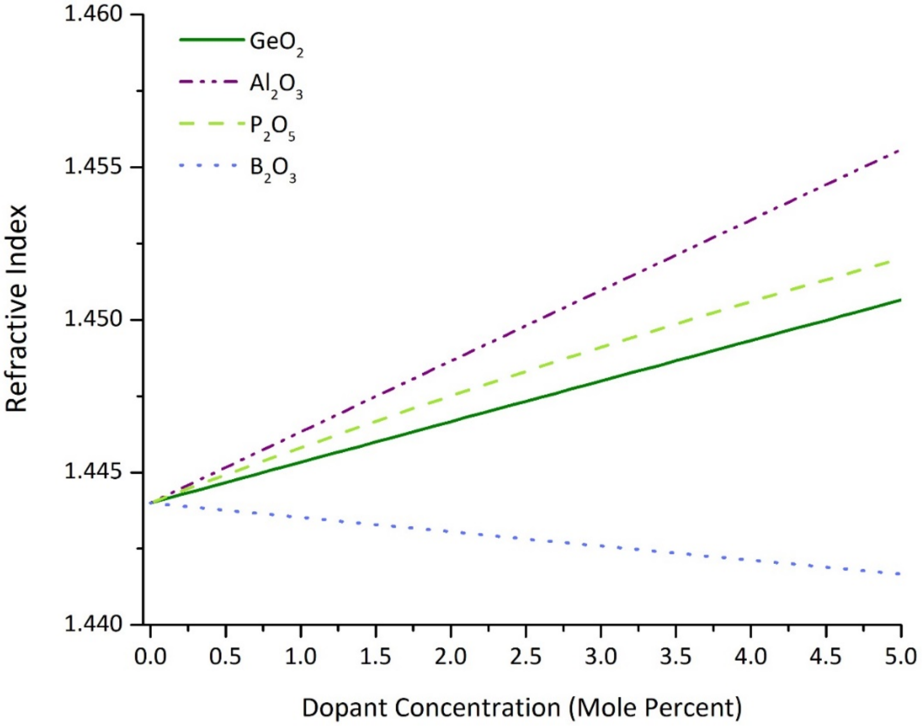

Figure 2.4: Common MCVD dopants vs effect on refractive index (n) [21]

$$2BCl_3(g) + \frac{3}{2}O_2(g) \rightarrow B_2O_3(s) + 3Cl_2(g) \qquad \text{Eqn. 5}$$

The sintering pass fully reduces the porosity and the glass is now transparent. However, the substrate is still a tube and not yet fully consolidated into a rod. Additional consolidation and collapse passes are required to transition the tube to a rod. The lathe burner gases are increased to achieve maximum temperature of approximately 2400°C, and the traverse speed is reduced while it travels from the headstock to tailstock direction. This increased temperature softens the glass and promotes the reduction of the inner diameter (ID) and outer diameter (OD). A total of 3 consolidation passes are required before the ID is sufficiently small enough to close it in a single pass. During the consolidation, a large quantity of P_2O_5 is volatilized at the elevated lathe temperatures. In order to counteract this volatilization, a constant flow of $POCl_3$ is maintained during all three passes. This flow is gradually reduced as the ID decreases with each consolidation pass to maintain the diameter reduction of the preform to a rod.

The final collapse pass is carried out from the tailstock to headstock direction (R to L in Figure 2.2). The burner is stopped while the glass is heated sufficiently that the surface tension of the glass fully facilitates a complete closing of the tube into a rod. Once that begins, the burner continues to move slowly so that the closed region continues along substrate back to the start position, leaving a fully collapsed preform. The transition area from open to closed is maintained in the middle of the burner during this pass by adjusting the burner speeds manually.

The reverse closing process serves two purposes. First, it is easier to begin the close process in this direction as the doped core layer is thicker on the tailstock side due to the reverse core deposition process used. This reduces the length of time to begin the close process, as the softer and thicker core region collapses more readily. Second, by collapsing beginning on the tailstock side, the $POCl_3$ rich atmosphere is trapped and burn-off of the core region is reduced. This is because all precursors and process gases are introduced in the headstock region. Gases flow from headstock (L) to tailstock (R) and out the exhaust tube. Closing the tailstock side first traps the atmosphere that contains an excess amount of $POCl_3$ precursor, reducing the amount of burn-off. An over-pressurization and failure of tube wall integrity is prevented by monitoring pressure of the tube at the headstock via the rotary union. Once the preform is fully consolidated the entire 500mm length, a manual hand torch is used to soften the glass and detach it from the tailstock.

2.4 Preform characterization

Each preform that is produced must go through a series of characterization steps to ensure it will meet the intended design parameters. After fabrication on the lathe, as just described, a sample from the finished tailstock end of the preform is removed. This sample is polished to expose the core region so that compositional analysis can be performed. The samples are scanned using a scanning electron microscope (SEM). The samples are scanned on a Hitachi SEM 6600 unit. A copper calibration and 20kV scan is completed before each new sample. The scan is completed using a low pressure of 30Pa with variable pressure setting and not full vacuum to mitigate the charging effects on these low conductivity samples. Samples were analyzed using a weight-by-weight percent (w/w%) list of elements known to be in the sample of Si, P, Al, Yb, and oxygen was obtained by stoichiometry. Boron is present but not detectable by the energy dispersive (x-ray) spectroscopy (EDX) analysis feature of the SEM. The integration and use of boron is addressed further in both Materials Science and Materials Engineering

Chapter of this Dissertation. This characterization step is necessary to ensure the desired core composition is maintained after preform fabrication. If there is compositional difference or drift, the glass is remade and re-characterized. The lathe fabrication step that caused the deviation is corrected, but the glass is not used in further development. Figure 2.5 is a flow chart representation of the development cycle steps involved to create a single active core rod.

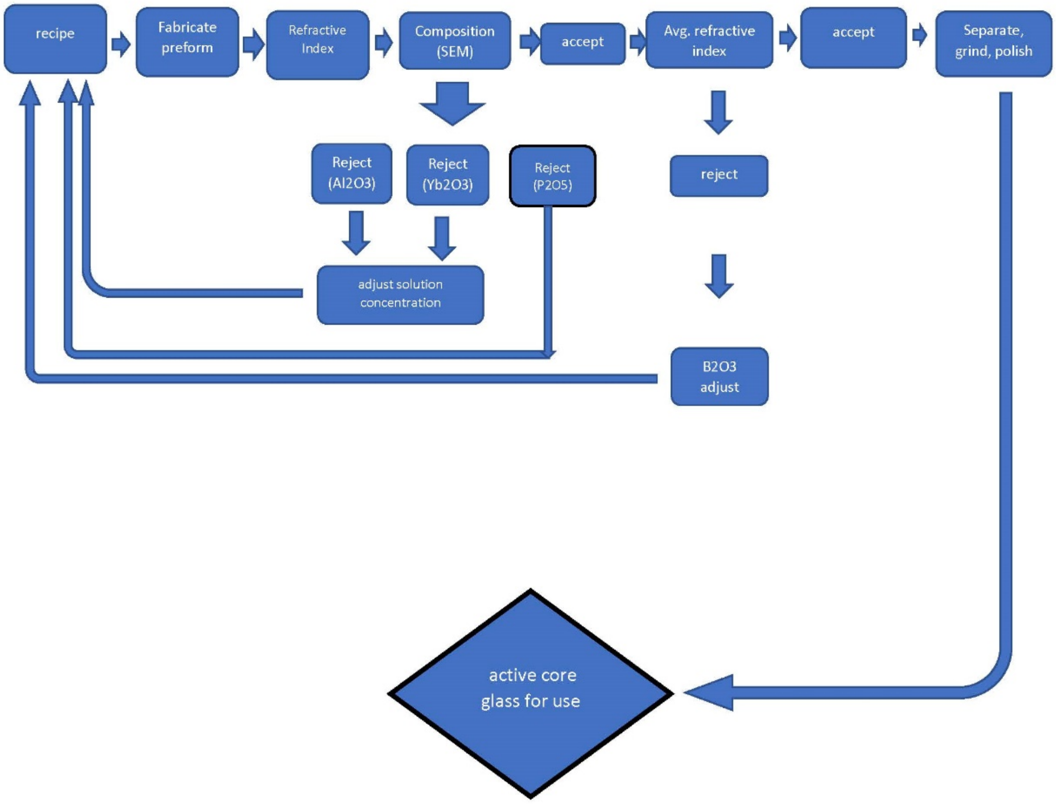

Figure 2.5: active glass development flow chart

After SEM analysis, the preform refractive index profile is characterized. A model 2600 preform analyzer by Photon Kinetics (PK) scans the preform at 10mm intervals over the entire length of the preform. The PK measures a refractive index difference (Δn) relative to that of silica at a wavelength of 632.8nm, which is 1.4570. The accuracy in index value is +/- 0.00020. [12] The preform is immersed vertically in an index matching oil and allowed to soak for 15 minutes to achieve thermal equilibrium with the oil. The preform is scanned across the diameter at each 10mm position starting at the tip. The scan interval can be tailored to smaller or larger increments, but for this research, every 10mm was sufficient to achieve a representative index along the preform length. An example of index data after plotting for a preform is in figure 2.6, where the X axis is in mm and the Y axis is Δn. The zero position is the center of the preform, as calculated by the PK2600 instrument.

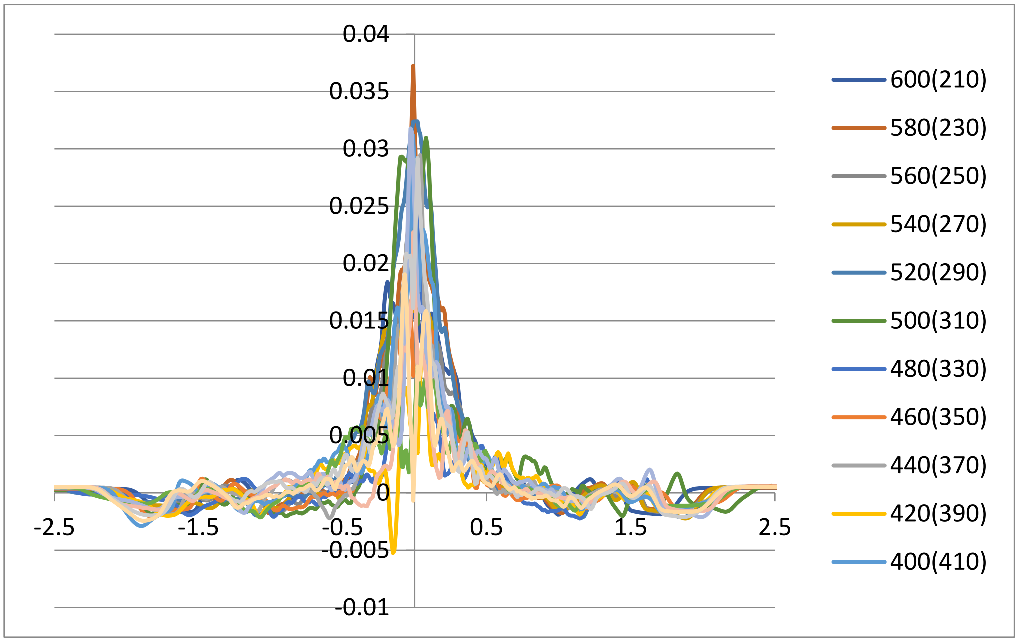

Figure 2.6: Sample refractive index profile of a preform (LA34413)

Once the index scan is complete, the data is plotted, as represented in Figure 2.6. The vertical axis is Δn and horizontal axis is position, in mm, across the cross section of the preform, where zero is the center of the preform. Using the initial refractive index data, the average refractive index is calculated to evaluate the index along the length of the preform as it relates to the target upper and lower limits. This representation allows for a linear 2D approximation of the index along the preform relative to the headstock and tailstock positions. The average index plot is used to identify sections that are within the target Δn range to be segregated from out of range regions of the preform for grinding and polishing. This prevents the incorporation of less desirable areas of the preform to be used in the final active core glass. As an example, Figure 2.7 shows that preform positions from 240 to 410mm are below the desired lower index boundary and would not be acceptable for use. However, there are more desirable sections within the upper and lower index boundaries between preform positions 520 to 670 mm that could be used. Further discussion of average index boundaries is addressed within the Materials Engineering discussion Chapter. The review of the boundaries and choice for the range for each phase of development is better suited with a further discussion of the nature of $AlPO_4$ and its role in the glass.

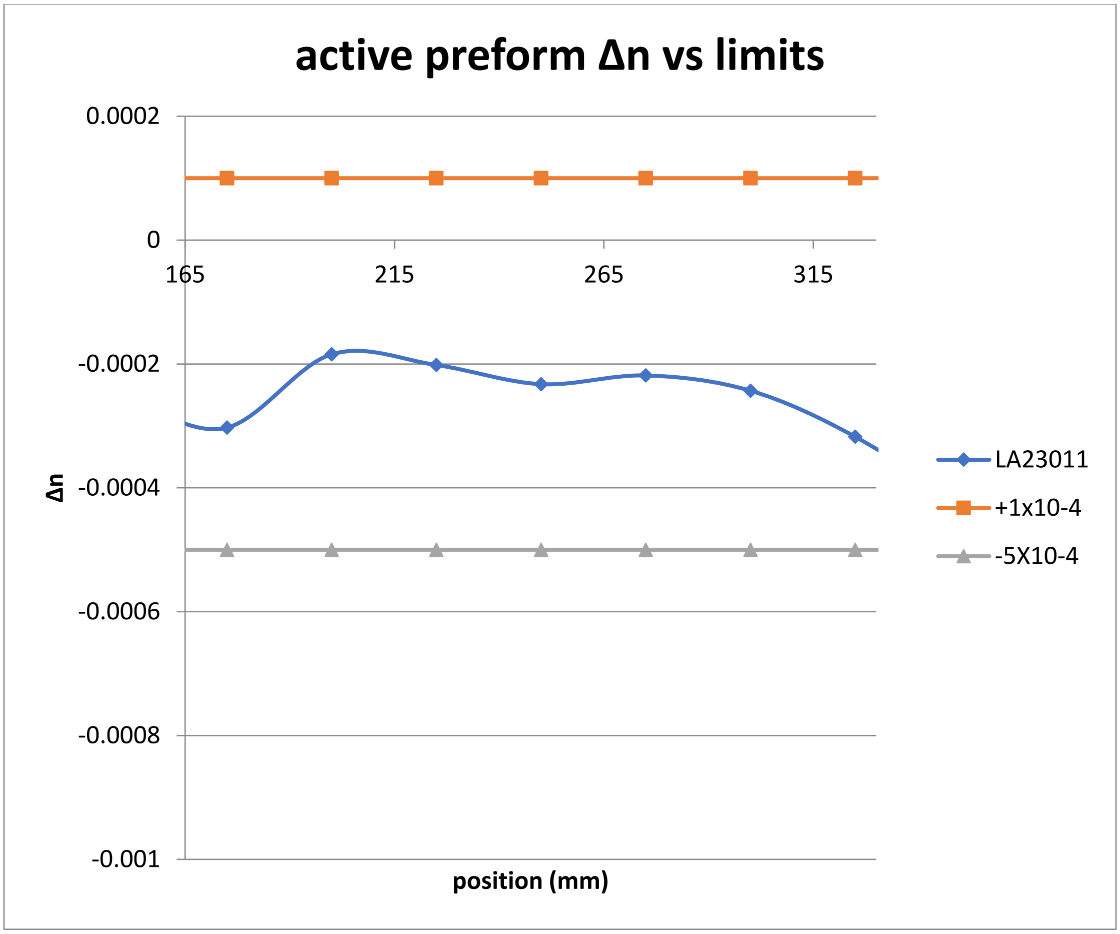

Figure 2.7 Average refractive index of preform

2.5 Preform preparation – grinding and polishing

Once a preform is fabricated and characterized, most of the outer cladding material needs removal for reasons later discussed in this Chapter, as it will dilute the core concentration when stacked. This is performed by an outside vendor [13, 14]. Average outside diameters of the preforms are reduced from approximately 16mm to 3.2mm +/- 0.1mm. An optical finish of the surface is added after the diameter is reduced. Lengths of the preforms that are ground ranged from a minimum of 150mm to a maximum of 200mm in length. Variation of the length is acceptable due to the difficulty in creating a preform within the desired index range, as well as use of a restacking and redrawing process, which is detailed later. The diameter of 3.2mm is chosen because this final size greatly reduces the volume of unwanted cladding glass (SiO_2) from the substrate tube, but also leaves a sufficient amount of silica in place for robustness and handling during the later stack and draw phases of the cores. Removing all the outer silica cladding is not possible as the doped core region cannot be stacked or drawn without it.

Before the actual development and fabrication steps for creating the active glass, the intent was to remove a significant portion of the outer silica clad while leaving a minimal amount necessary to ensure safe handling, stacking and drawing. Without this removal, the active core component would be too dilute and not capable of successful lasing as a novel phosphosilicate core. Typical preform dimensions using a substrate tube with a 19mm ID by 25mm outer diameter, OD (Hereaeus Tenevo F300), will yield a final preform with OD of approximately 16mm and core diameter of approximately 2mm. This gives a core to OD ratio of approximately 16% active region by dividing the core diameter by final OD. After grinding and removal of the outer cladding to 3.2mm, an all silica cladding approximately 500 microns in thickness remain. This new ratio of approximately 68% active core is more optimal for a core glass as most of the material will contain Yb (in the form of Yb_2O_3). At this ratio, dilution of the active glass is greatly reduced compared to that of a preform with a fully intact clad region. In Figure 2.8, A full length preform, separated section, and then ground and polished core rods are displayed as an example of both length and diameter reduction.

Fig 2.8. Starting preforms prior to grinding (top), shortened section (mid) and preform after clad removal and surface polish(bottom)

2.6 Active glass stack orientation

While adherence to the upper and lower limits of the target glass is observed, there is still some slight variation of finished pieces to be slightly higher or lower in Δn. None of the preforms fabricated were identical in that regard, as it is not possible to repeatedly control the index to the third and fourth decimal place for all preforms throughout the entire 500mm length of the finished length. Some pieces were slightly higher or lower within the desired index boundaries within a single preform. The final glass needs to have index uniformity so the stack is created by pairing higher index pieces with lower ones. Using this method, the final glass should have a flat Δn profile with less variation from one region of the glass to the other. Figure 2.9 is the resultant stack configuration for a series of Yb doped preforms after comparing and matching ground pieces with varying refractive indices within the upper and lower limits.

A brief explanation should be given regarding the unique identification numbers for all preforms and fibers fabricated at Clemson. This will further explain the numbers associated with each preform piece in Figure 2.9. All processes should have a method for sample identification that allow for clear explanation and tracking the history of a product from inception to end of life. That is the goal of each sample identification used by the fiber fabrication group. Each code is made of 2 letters and 5 numbers. The first letter is either L or D, where L = a preform from the lathe and D = a draw on the optical fiber draw tower, and all preform identifications (ID) begin with L and all fiber ID's begin with D. The second letter indicates the order of fabrication for that day. The letter A would be first, followed by B for the second, and so on. The first 3 and last 2 digits represent the Julian day and year, respectively. A fiber or preform fabricated on March 15, 2019 will be designated by the number 07419, where the 15th of March is the 74th day of 2019. To expand on this further, the first preform fabricated March 15, 2019 will be LA07419. The second fiber drawn on March 15, 2019 will be DB07419. These unique codes follow each fiber or preform from creation to disposal. They allow for historical data to be pulled regardless of timeframe, if number is available.

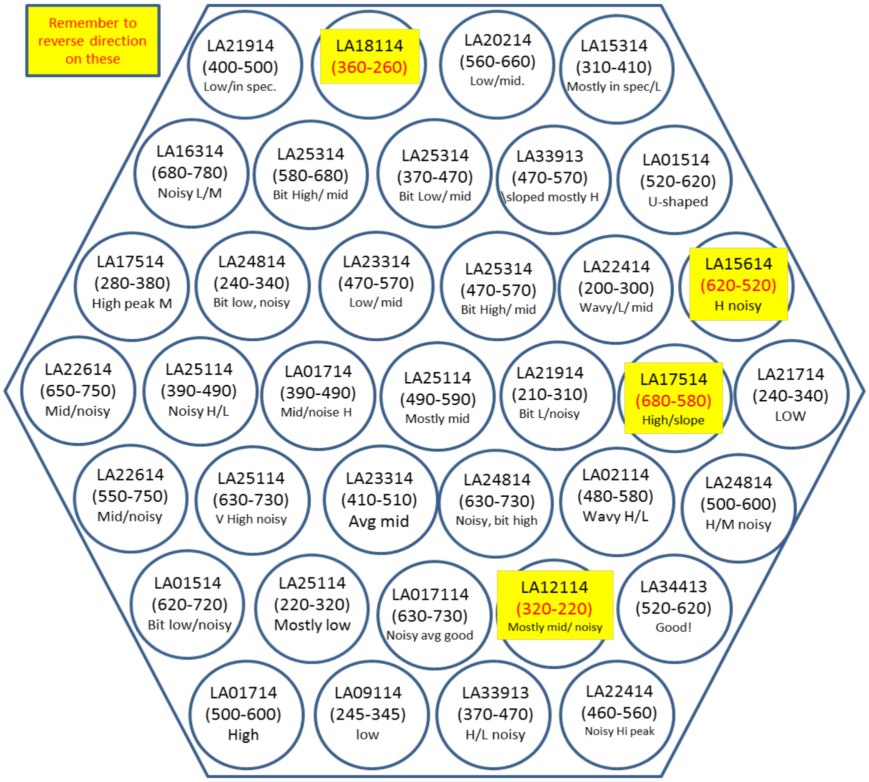

Figure 2.9: Yb doped preform layout after matching high and low trending core rods

2.7 Stacking and glass-working

After pairing the core rods based upon the average refractive indices, the individual pieces must be combined to form a uniform hexagonal stack. A graphite clamp was designed and fabricated to hold the glass pieces as well as be thermally resistant to the required glass-working of the core rods. The inner surface of the clamp is lined with foil to reduce transfer of graphite to the core pieces during glass-working, as the stack cannot be cleaned safely once it is joined to a handle. The clamp and stack are shown in Figure 2.10.

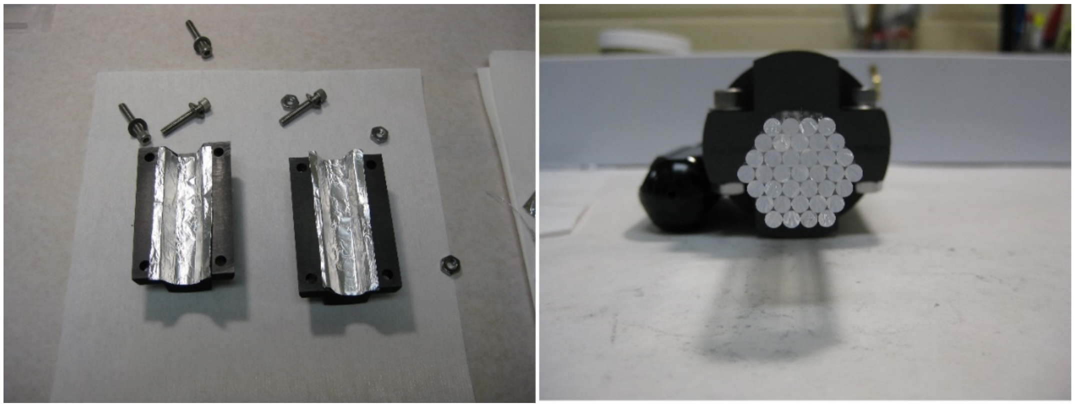

Figure 2.10: graphite hex clamp with foil (L) and core rods stacked (R)

After clamping, the core rods must be attached to a handle and sleeved inside another over-clad tube. The handle, as it is attached to a stack in Figure 2.11, is necessary for feeding the pieces vertically into the furnace and draw them due to their short length. The outer clad tube is necessary to consolidate all cores under vacuum into a single 1.5mm rod. The furnace configuration and draw tower layout does not allow for the stack of core rods to be drawn without the handle and over-clad tube due to their length. An H_2/O_2 burner is used to attach the handle tube to the stack, and then it is cooled to room temperature.

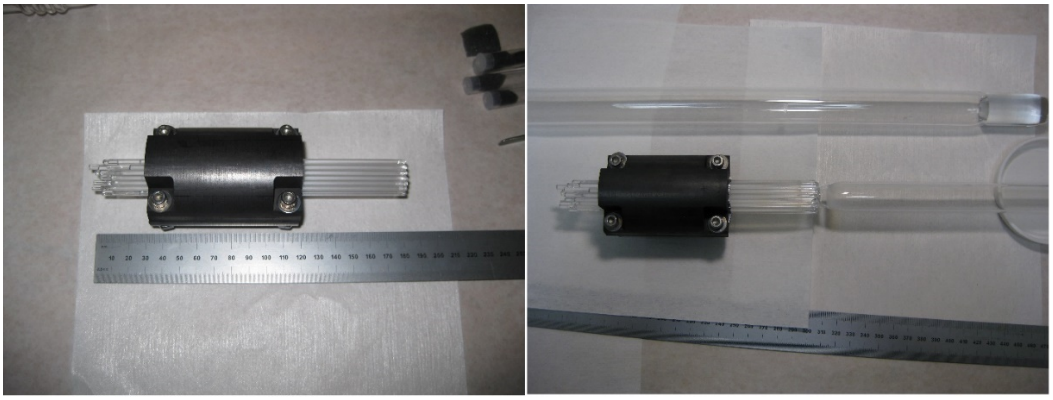

Figure 2.11: active stack before and after handle tube

As can been seen in Figures 2.9 and 2.10, the maximum width of the stack is 7 core rods of 3.2mm OD. This gives a maximum corner to corner distance of 22.4mm. The over-clad tube must be of sufficient thickness to maintain the stack integrity, but also thin enough so as not to dilute the active region by increasing the volume of undoped silica to the doped glass. An over-clad tube of F300 glass (Heraeus Tenevo) with and ID of 23 and OD of 28mm was chosen for this work. The stack and handle were inserted into the over-clad tube and attached to vacuum controls to evacuate the interior and consolidate the structure once the draw temperature was achieved. A fully over-clad stack is in Figure 2.12.

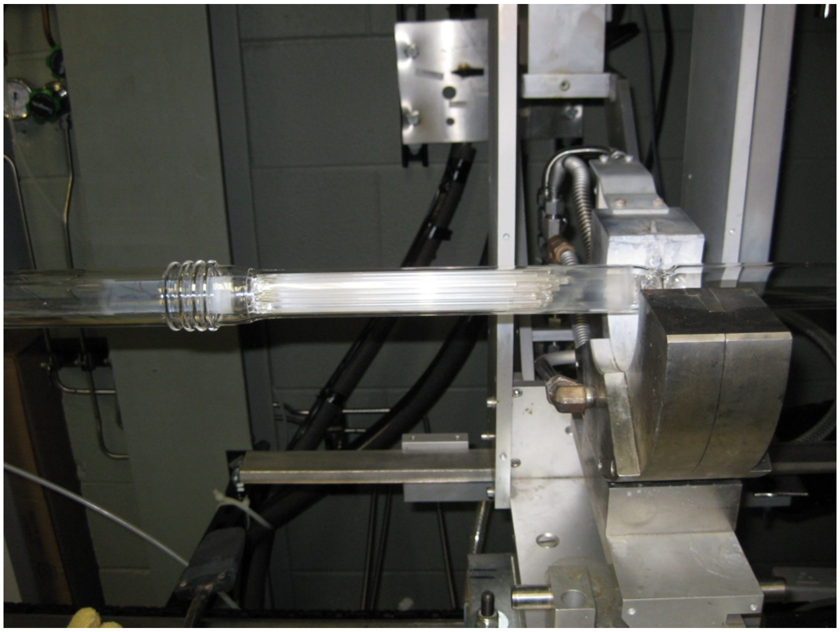

Figure 2.12: Stack in over-clad tube after glass-working

2.8 Active cane draw

All draws are completed using the facilities at Clemson University. A 6.5m standard draw tower is used that is capable of drawing glass preforms from approximately 3mm OD to 50mm OD. The OD of the fibers that can be drawn can range from 40 microns to 18mm OD. Several variables can influence these sizes, such as glass type, OD, and desired final fiber dimensions. The tower is capable of drawing glasses with various softening temperatures from slightly above room temperature up to 2200°C. For the purposes of this Dissertation, a high temperature furnace, manufactured by Centorr Industries, was employed that contains a graphite element and is purged with ultra-high purity argon for use on all silica glass draws. This furnace has a working temperature range from 900°C to 2200°C. A typical draw tower configuration along with the draw tower at Clemson is shown in Figure 2.13.

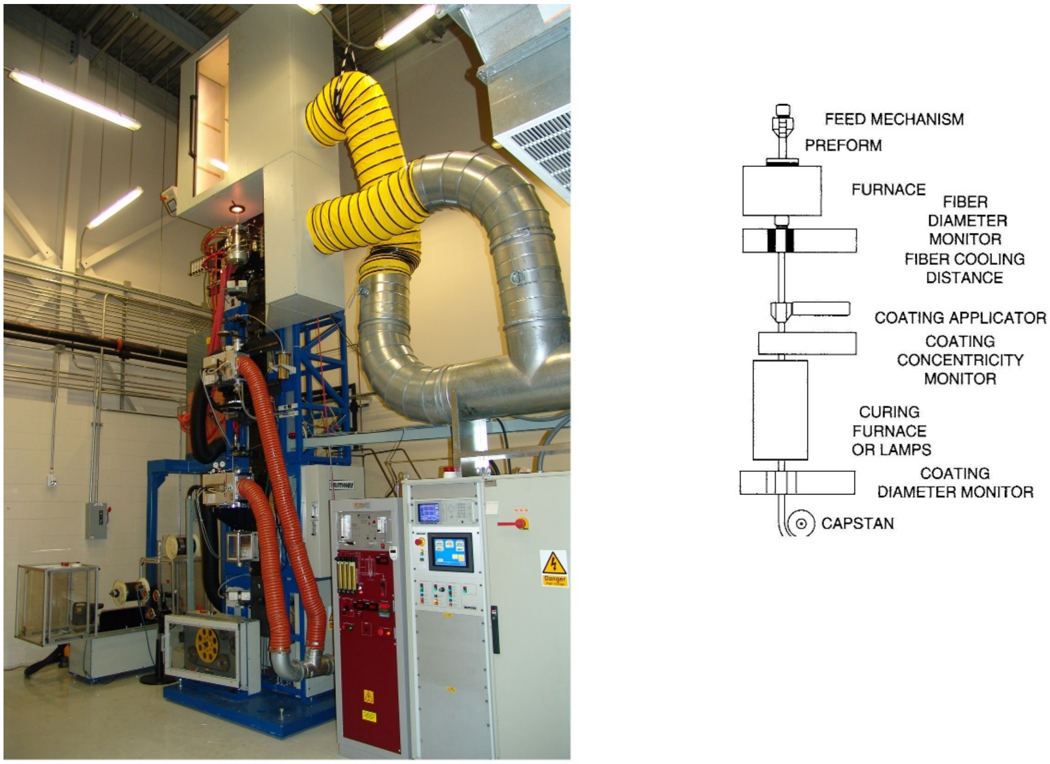

Figure 2.13: Clemson draw tower and typical tower layout [15]

Once the stack workup is loaded into the furnace and attached to the vacuum and pressure control system, the tube interior and stack surfaces are purged while being heated to remove any moisture on the glass surface. The furnace is heated to 1200°C. Dry N_2, taken from a liquid nitrogen source, is flowed through the tube at a rate of about 20 lpm while the entire preform assembly containing the active pieces passed through the heat zone at a rate of about 50mm/minute. This process is repeated three times.

After drying, the furnace temperature is increased to 1950°C to begin the draw process. A vacuum of -4” Hg is applied once the glass is sufficiently hot and begins to soften. The preform is fed into the furnace at a rate of 3mm/minute and drawn out using a belt tractor assembly at a rate to achieve a final target OD of 1.5mm. The temperature is reduced to approximately 1850°C to achieve an optimal draw tension as the preform begins to reduce in diameter to the desired range. This lower temperature also serves to optimize the outside diameter and ensure uniformity, as higher temperatures will allow the glass to soften and deform the glass due to the higher P_2O_5 content of the core.

2.9 Active Glass Redraw

Once the core material is fully drawn, All the pieces are then collected, cut to approximately 100mm lengths, then restacked inside a 17x21mm silica tube and drawn. The initial draw consolidates the core pieces, but there are still noticeable diameter fluctuations and index differences. The redraw of the core pieces a second time eliminates these differences, and the final active glass will be of uniform index, composition and OD. In Figure 2.14 below, the variations in sizes can be seen in the left image, while the new fully stacked over-clad tube from the initial draw is on the right.

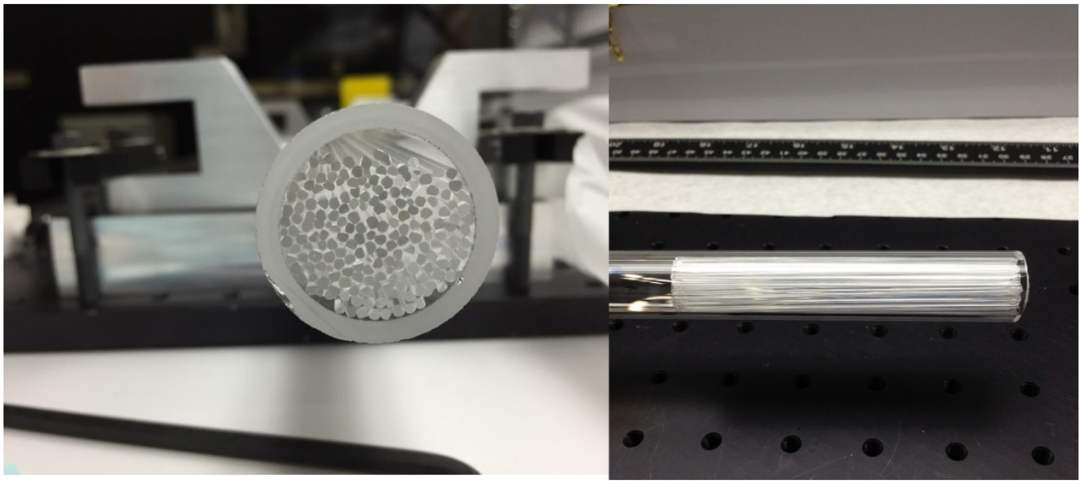

Figure 2.14: redraw stack of active core pieces.

Using a similar process as the initial draw described in Section 2.6, the drawn pieces are cut to the same lengths, then sleeved inside a 17mm×21mm over-clad tube. Additional glass-working is completed to ensure the active core pieces do not slip out of the tube once it is turned vertical. A total of ten drying passes were used on the redraw at 1200°C versus three on the initial draw. Once the drying passes are completed, the furnace temperature is increased to 1925°C until the glass softens. The vacuum is increased to -4” H_2O, and the final cane is drawn to a target OD of 1.5mm. This final draw yields a series of 1.5mm OD canes of uniform OD and length. These canes can then be cut into smaller lengths and stacked together in various fiber designs. A cross section of one of the finished canes from active phase 2 is in Figure 2.15 below. Detailed dimensions of the resultant glass pieces are discussed in greater detail in Chapter 3.

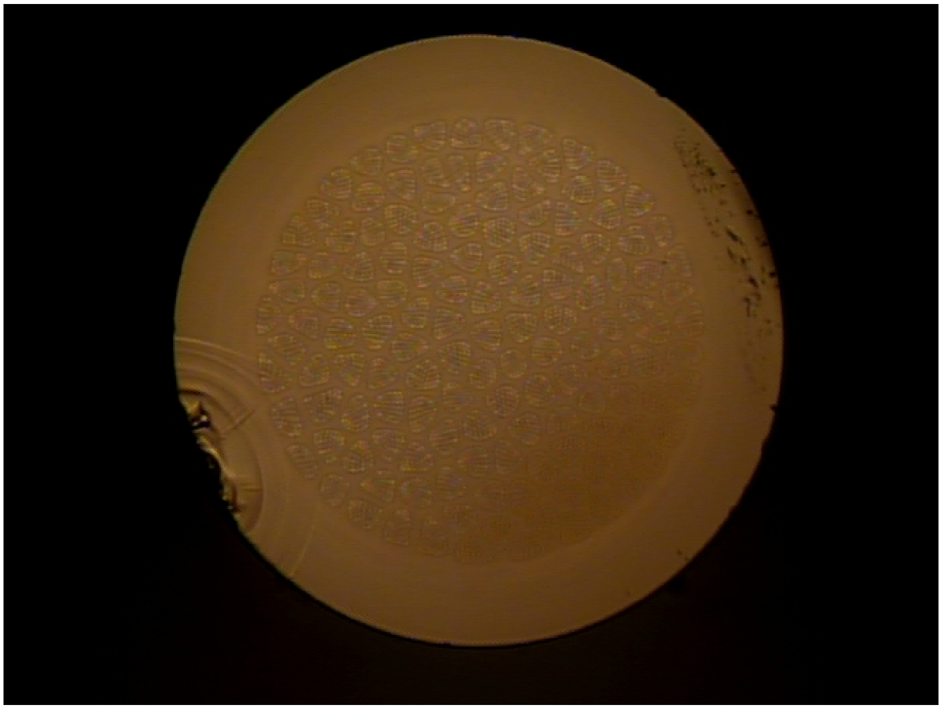

Figure 2.15: Active cane after redraw

2.10 Integration and fiber fabrication

Using a multiple step draw and redraw process for active glass development, the new core pieces are ready to be incorporated into custom fiber stack designs. Since the active glass has been stacked and redrawn, the core pieces are identical to each other and there is no need to compensate for variations within them. All the canes are the same OD, composition, index profile, and they can be cut to identical lengths depending upon the requirements of the COMSOL modeling and fiber design. The quantity and length of the new active core glass varies and is dictated by the modeling, simulation, fiber design, and availability of other glass components that are necessary for the design. Below are examples two different designs in Figure 2.16, each having very different quantities of active glass in them. The design on the left only requires a single active core (red region) while the design on the right (purple region) requires a total of 7 active cores.

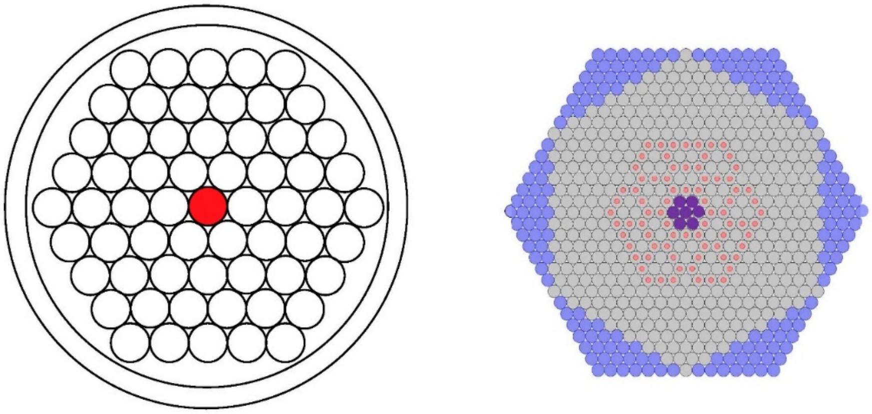

Figure 2.16: Active core comparison

2.11 Stacking, tacking, and over-clad

Using a cross sectional template of the desired final fiber as a guide, a new work-up is created by stacking a combination of silica or active glass in a hexagonal arrangement. The position of each piece is determined in the cross section of the fiber design. Each glass rod (or cane) is selected, cut to the desired length, and positioned between a series of angled guide blocks that are sized according to the final stack dimension. This is defined by the fiber design cross section. The canes are stacked from the bottom of the design to the top in the order and type according to the cross section, as in Figure 2.16.

After stacking, the individual canes are secured using metal clamps around the outside. These clamps prevent the individual canes from shifting during movement. The clamps are secured using bolts at positions along the length of the stack. One set of clamps is much wider and is used to secure the stack on the draw tower for glass-working and tacking. When the clamps are secured, tungsten wire is wrapped around the stack within the first 40mm only. This wire will not melt at 1800°C, which is the temperature used to adhere the glass pieces together and ensure the stack is robust. The tungsten does not oxidize as the furnace interior is purged with ultra-high purity argon that has gone through additional purification and filtration after leaving the bottle. Without the wires in place, the individual canes will expand and pull away from each other during the tacking process, causing the overall stack dimensions to change.

Once tacked, the stack is allowed to cool and the wires are removed. The now rigid section of the stack does not need wires or clamps to inhibit movement of the individual canes. The end of the stack that was previously wired is now loaded back into the furnace and reheated to 2175°C. The first approximately 40mm of the stack soften and pull away from the rest of the stack, leaving behind tapered neck-down region of fused glass. This new region will have a handle, or hangar tube, attached to it for the remainder of the fabrication process. Figure 2.17 shows a section of the stack with wires and clamps as well as the tapered neck-down region after tacking and drop. Figure 2.18 shows the stack with handle attached.

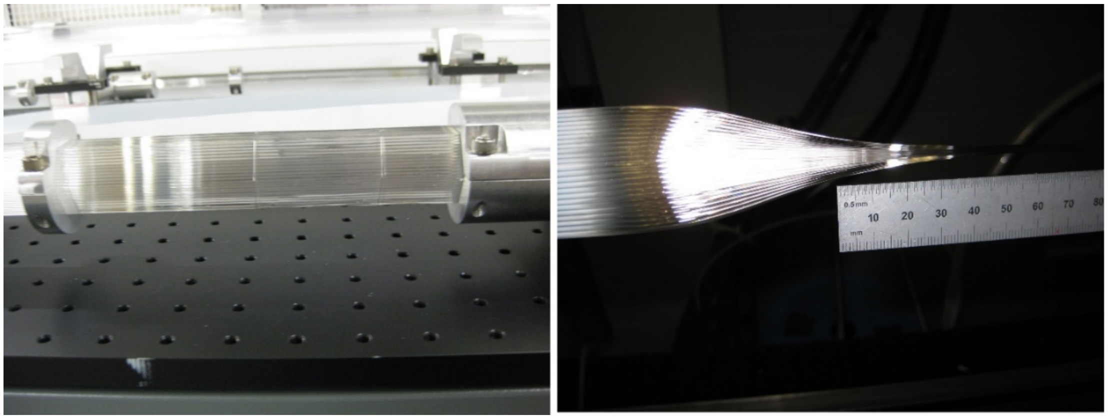

Figure 2.17: Clamp and wires on stack (left) and neck-down after tack and drop (right)

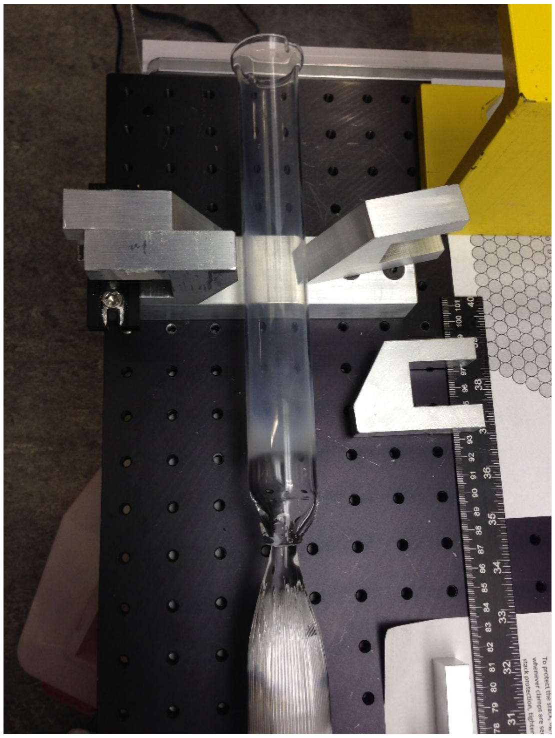

Figure 2.18: Top of stack with handle

The new neck-down and tapered end of the stack with the attached hangar tube is now the top, and it is used to orient the rest of the glass-working and fiber draw. The middle of the stack is secured with the widest clamp and the bottom is wired with the tungsten as before with the top of the stack. The entire stack is moved to the glass-working lathe and a handle is attached to the tapered top of the stack using an H_2/O_2 burner. The handle is flared at the top, which will secure it to the cladding tube for the entire stack.

The bottom of the stack is loaded in the furnace and tacked at 1800°C. The stack is cooled, wires are removed, and loaded into the furnace. This bottom end is also heated to 2175°C and a drop taken off the stack, fusing all the pieces together. Once the bottom of the stack is fused and tapered, clamps or wires are no longer necessary to maintain the structure and prevent shifting. The stack with handle is inserted into an over-clad tube which has been fabricated separately. The size of the over-clad tube is determined by the fiber design. It is necessary to use an outer tube for the stack as it would not be possible to consolidate the entire structure under vacuum without it into a solid structure.

2.12 Stack to Cane Draw

Many stack sizes that are fabricated are not suitable to be directly drawn to their desired fiber size. This is due to the size of the stack versus reduced fiber diameter, the need for future fibers from the same batch of material, as well as new sizes that are not currently anticipated for the design. In order to illustrate this further, some additional dimensions of one of the larger stack and fiber designs are provided that will support the need for a stack to cane draw step. A typical final stack length is approximately 500mm before it is placed inside the clad tube and drawn to cane. An example of the larger stacks that are fabricated at Clemson has a corner to corner dimension of 37.5mm on the hexagonal cross section. This stack is inserted into an over-clad tube of 40mm ID x 44mm OD. Within the 500mm length of the stack, only 200mm of active core material is used, as illustrated in Figure 2.19. The remaining section is filled will silica rods to maintain the structure and shape of the stack, but they are not optically active. These sections of the stack are used to eventually draw passive fibers to determine the bandgap for the desired active fiber. [16] A typical stack with these dimension yield 10 to 15 meters of canes without active core, and with a corner to corner dimension of 5.5 mm.

The active section of the stack will yield 5 to 8 meters of canes. Drawing these passive pieces prevent waste of the limited amount of active core material and allows for flexibility for future testing and fiber requirements that are not currently anticipated. Each cane can be drawn to over a kilometer of 125 micron (μm) diameter fiber, so having a large number of pieces is not necessary. Many fiber draws for the desired laser fiber are only a few tens of meters.

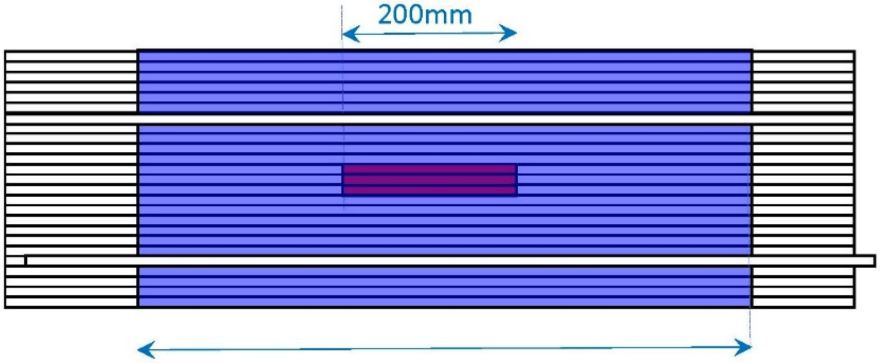

Figure 2.19: Stack layout from the side

The entire workup of stack and over-clad tube are loaded into the draw tower. The stack is lowered into the furnace past the center of the heat zone in the furnace while the entire interior of the stack and over-clad tube is purged with nitrogen. The furnace is heated to 1000°C and the stack and over-clad are raised through the heat zone at a rate of 20mm/min while being purged with nitrogen at 20 lpm to dry the interior and remove any surface debris before cane draw. After the drying process is completed, the nitrogen flow is stopped, and the furnace temperature is raised to approximately 2175ºC to soften the glass for cane draw. Once at temperature and the glass is soft, the interior of the clad tube and stack is evacuated at -50” H_2O for the duration of the draw. This removes any air and fully consolidates the structure into a solid cane. The temperature is then reduced to optimize draw tension and remove all air spaces within the stack. The resulting cane cross section is fully solid. Figure 2.20 shows a fully stacked series of individual canes and the finished cane cross section after draw.

In Section 2.6 a brief explanation was given regarding the nomenclature used for identification of different preforms and draws. Some explanation should also be given at this point for the nomenclature used in fiber designs for the purpose of internally grouping the characteristics, materials, and various testing procedures for each fiber design. Unlike the method used for fibers and preforms, the one used for designs is less straightforward. Using Figure 2.20 for reference, the fiber design shown is labeled HEL3B. This design was part of a high energy laser research project, which is indicated by HEL. It was the third design of this project, and it was the third re-creation of this design. The first stack was designated HEL3, and the first remake due to fabrication issues was HEL3A. This third fabrication of the same design for the same project was HEL3B. Currently as of this writing for the high energy laser research projects, the latest generation fiber design is HEL12. [15]

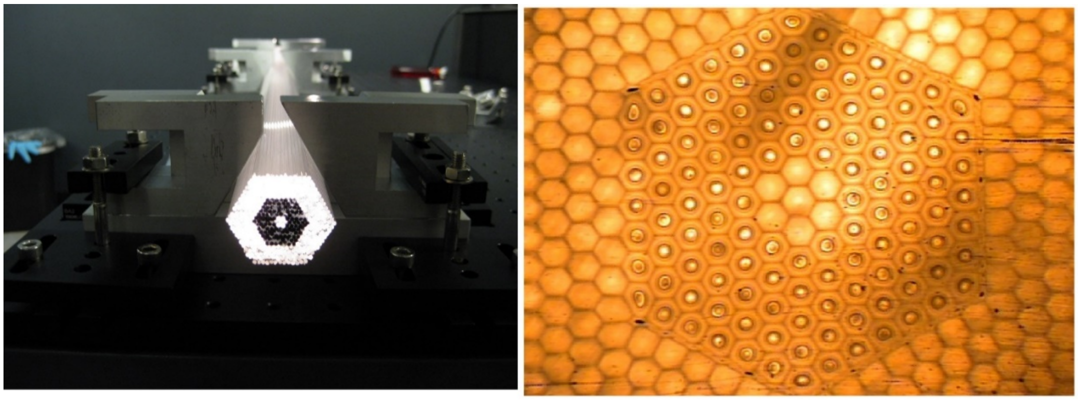

Figure 2.20: Fully stacked design HEL3B and final drawn cane

2.13 Cane to Fiber draw

After a cane is fabricated from the stack, the new fiber must be drawn. The initial cane to fiber draw is typically done using the passive cane for bandgap measurements. The fiber design modeling provides the target bandgap and estimated core size of the final fiber design, but an actual fiber must still be drawn to verify the model. A passive cane that does not contain active core glass is drawn to the calculated fiber dimensions based on the COMSOL modeling. The first photonic bandgap for the respective core size of the passive fiber is evaluated. Once verified, the target core and fiber dimensions are adjusted for the active fiber draw [16]. The flat-to-flat dimensions (Figure 2.21) of the passive cane are recorded, the corner to corner and the cross-sectional areas are then calculated. Using these values, the desired fiber flat to flat dimension can be calculated. This value is used in conjunction with the canes starting dimensions to determine the desired cane feed rates and drawing line speeds to achieve the desired fiber dimensions.

The passive cane is loaded into the furnace to the target position within the heat zone. The furnace is heated to 2175°C to soften the glass and begin the drawing process. Once a portion of the cane in the heat zone softens and begins to drop away from the remainder, the bottom iris of the furnace is opened. The drop is cut into a bucket and the remaining smaller OD fiber is pulled manually down to the bottom of the tower and inserted into the capstan. The temperature is reduced to achieve optimal fiber tension, and the feed and capstan draw speeds are adjusted to achieve the target fiber flat-to-flat dimensions that were previously calculated. Figure 2.21 shows a typical cross section of an active core fiber. In this example, the flat-to-flat dimension is 373 microns while the corner to corner dimensions are 411 microns.

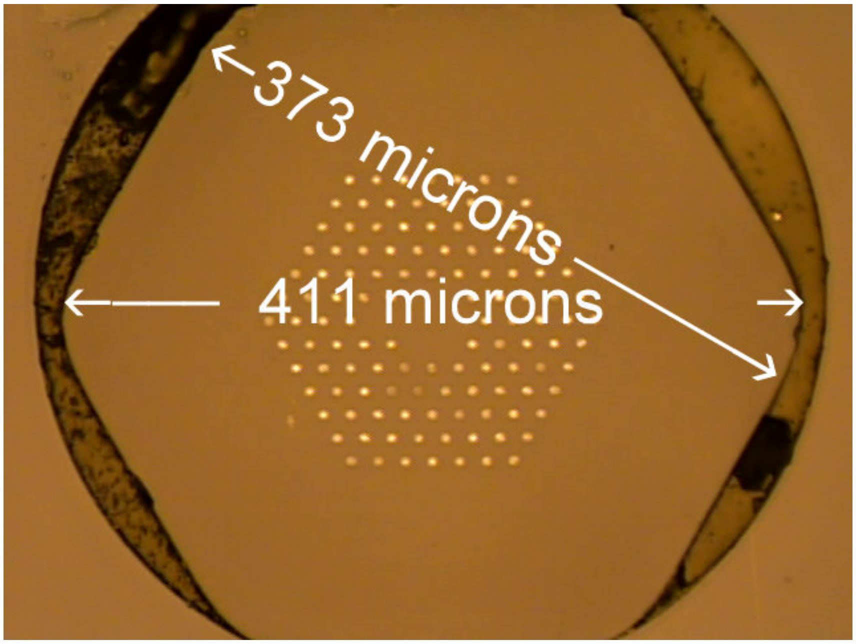

Figure 2.21: Fiber flat and corner dimensions

After the size and tension is optimized for the desired draw parameters, a UV curable polymer coating is applied to the fiber. This coating can either be higher index [18] or lower index than the clad glass to achieve a double clad configuration [17, 19]. A double-clad configuration is important for some fiber designs, such as the one is Figure 2.21, as it increases numerical aperture (NA) of the clad and improves pump efficiency by allowing for more pump light to couple into the core. The coating is a liquid until exposed to high intensity UV light, which cross links the polymer and a solid cured coating remains to protect the glass surface. This coating is applied via solid die configuration, which is commercially available [20]. The configuration consists of an upper die, middle reservoir, and lower die. These parts are assembled in the coating head before the fiber draw, and the fiber is threaded through it during the process. The top and bottom dies ID are chosen based upon the calculated fiber diameter and desired coated diameter. These are determined prior to the start of the draw process, and they can vary depending on the required fiber fabrication parameters.

After the coating is applied and cured, the fiber is wound onto a spool. This spool size is determined by the coated fiber diameter. A larger diameter fiber requires a larger spool due to the reduced bend radius. Smaller diameter fibers can be wound on to smaller diameter spools due to their increased bend radius compared to their larger diameter counterparts. The fiber spool is rotating and traversing a specific distance left to right. This traverse distance is known as the pitch, and the value used is determined by the final coated fiber diameter. The objective is to lay the fiber side by side with each revolution of the spool without overlap in a single layer. Once the fiber is wound, the fiber is ready for testing and further analysis.

2.14 References

1. F. Kong, G. Gu, T.W. Hawkins, J. Parsons, M. Jones, C. Dunn, M.T. Kalichevsky-Dong, K. Wei, B. Samson, and L. Dong, “Flat-top mode from a 50 μm-core Yb-doped leakage channel fiber,” *Optics Express* 21, 32371-32376 (2013).
2. F. Kong, C. Dunn, J. Parsons, M.T. Kalichevsky-Dong, T.W. Hawkins, M. Jones, and L. Dong, “Large-mode-area fibers operating near single-mode regime,” *Optics Express* 24, 10295-10301 (2016).
3. J. B. MacChesney, P. B. O’Connor, F. V. DiMarcello, J. R. Simpson, and P. D. Lazay, “Preparation of low loss optical fibers using simultaneous vapor deposition and fusion”, *Proc. 10th Int’l Congress on glass*, Kyoto Japan 1974.
4. K. Oh, U. Paek, *Silica Optical Fiber Technology For Devices and Component,* 2012 John Wiley and Sons.
5. G.Vienne, J. Caplen, L. Dong, J. Minelly, J.Nilsson, D. Payne, “Fabrication and Characterization of Yb3+ : Er3+ Phosphosilicate Fibers for Lasers”, *Journal of Lightwave Technology*, Vol. 16, No. 11, Nov. 1998.
6. J. Townsend, S. Poole, D. Payne, “Solution-doping technique for fabrication of rare-earth-doped optical fibres” *Electronics Letters*, 23(7), pp.329-331 (1987).
7. J. Ballato, P. Dragic, “On the clustering of rare earth dopants in fiber lasers”, *Journal Directed Energy.* 2017;6:175-81.
8. https://www.sgcontrols.co.uk/index.php/products/84-preform-products/8-preform-mcvd

9. United States Patent # US 6,821,449 B2, "*Two step etching process for an optical fiber preform"*.
10. L. G. Van Uitert, D. A. Pinnow, J. C. Williams, T. C. Rich, R. E. Jaeger, W. H. Grodkiewicz, "Borosilicate glasses for fiber optical waveguides", *Materials Research Bulletin*, Vol. 8, pg 469-476, 1973.
11. H. Murata, *Handbook of Optical Fibers and Cables*, Second ed., Marcel Dekker, New York 1996.
12. http://www.pkinetics.com/products/productdetail.aspx?model=2600.
13. http://www.cidraprecisionservices.com/.
14. https://www.wilmad-labglass.com/.
15. A. Mendez, T. F. Morse, *Specialty Optical Fibers Handbook*, 2007 Elsevier.
16. F. Kong, K. Saitoh, D. Mcclane, T. Hawkins, P. Foy, G. Gu, L. Dong "Mode area scaling with all-solid photonic bandgap fibers", *Optics Express,* vol. 20, No. 24, 19 Nov. 2012.
17. T. Matniyaz, W. Li, M.T. Kalichevsky-Dong, T.W. Hawkins, J. Parsons, G. Gu, and L. Dong, "Highly efficient cladding-pumped single-mode three-level Yb all-solid photonic bandgap fiber lasers," *Optics Letters,* 44, 807-810 (2019).
18. https://focenter.com/wp-content/uploads/documents/AngstromBond---Fiber-Optic-Center-AngstromBond-DSM-3471-3-14-UV-Cure-Fiber-Re-Coating-(1Lt)-Fiber-Optic-Center.pdf
19. G. Gu, Z. Liu, F. Kong, H. Tam, R. Shori, L. Dong, "Efficient ytterbium-doped phosphosilicate double-clad leakage-channel fiber laser at 1008-1020 nm", *SPIE*

Proceedings vol, 9728 97282Q-1, fiber lasers XIII, Technology, systems and applications.

20. https://www.sancliff.com/fiber-optic-fiber-coating-worcester-ma
21. T. Hawkins, J. Ballato, P. Dragic, "A Unified Materials Approach to Mitigating Optical Nonlinearities in Optical Fiber. IV. Opportunities for Vapor Phase Processing" (publication in process)

CHAPTER 3

STUDY AND DEVELOPMENT OF ACTIVE LASER GLASS

3.1 Introduction and Research Motivation

There is a significant discussion in Chapter 1 regarding the role of the light emissive dopant ytterbium (Yb) in host glasses for fiber lasers due to its simple energy level structure, which facilitates high power lasing. Further, Chapter 1 detailed several glasses that were excellent hosts for Yb, namely aluminosilicates (AS), phosphosilicates (PS), and aluminophosphosilicates (APS). Chapter 2 details the thought processes and understanding that went into creating these glasses via MCVD with desirous properties for high power fiber lasers. Based on this, the properties of the resultant glass rod to be incorporated into advanced fiber designs as an active core material for lasing in optical fibers are discussed [1, 2, 3].

The main objectives of this Chapter therefore are to detail the creation of active host glasses for fiber lasers. This process involves understanding the role of the various material components that will be added to or combined to create a new host glass composition and the fundamental role of those components in achieving the properties required for power scaling the resultant fiber to > kW power levels; much to ask of any glass. Further, these compositions will need to be sufficiently stable to use in a variety of fiber laser configurations (as described in Chapter 4, for example).

Materially, there are multiple components that comprise these glasses that must be studied and their impact understood. These include phosphorous pentoxide oxide (P_2O_5), aluminum oxide (Al_2O_3), boron oxide (B_2O_3), aluminum phosphate ($AlPO_4$), and ytterbium oxide (Yb_2O_3). All these constituents will be used in conjunction with each other to create a new glass composition. Conversely, many of these components play different roles or influence the glass optically, thermally, and physically on both the bulk (preform) and fiber scale. Lastly, all are used via conventional MCVD fabrication methods that are commercially accepted in the high-power fiber laser industry around the world.

This Chapter also will understand the materials science and engineering as it affects the creation of new laser glass hosts, achieving practical functionality to build new fiber designs, and perform in a high-power lasing application. The goal of this research is to illustrate the importance of understanding the materials from the atomic scale (i.e. lasing of the Yb ion) up and through the macro scale (i.e. creating a stable, functional series of preforms to be drawn to a fiber laser). To show this, first to be discussed will be the role these glass materials serve in the host material from both scales, and their function in fiber lasers. Then discussed are the various stages of creating the glass, the importance of materials characterization, and then how it performs when it is used in a new fiber laser. Within this process will also include the engineering difficulties and further material understanding during this research. Lastly, this new active glass research in this Chapter creates a starting point for Chapter 4, which focuses on the creation of a new low thermo-optic coefficient fiber laser. In that Chapter, research on this active laser glass created here is the base material composition and beginning for the creation of this new fiber material that works to reduce Transverse Mode Instability (TMI) via understanding and changing material properties of the glass [4].

As noted, this dissertation research seeks to study and understand the inter-play between active core glass composition, structure, and properties in order to advance high power fiber lasers. This Chapter will primarily focus on the creation of a new active host glass, as well as the subsequent research into the material properties that will support that use. From a practical perspective, this work will constrain itself to MCVD preform fabrication (with solution doping) and fiber draw since they are readily available at Clemson but also standard within the specialty fiber and fiber laser industry. Unlike lightly doped silica fibers, such as those employed in telecommunications, the core compositions inevitably developed herein will push glass-forming limits and issues such as phase separation, high stresses, and much lower draw temperatures will have to be solved. A new understanding how to process these materials using conventional stack and draw processes must also be developed.

After initial core glass compositional development largely focused on Yb spectroscopy and refractive index control, the knowledge gained will be used to create more tailored glass compositions that provide further reductions in SBS and TMI through compositional tailoring of photoelastic and thermo-optic effects [5]. This new low thermo-optic coefficient is discussed in Chapter 4.

3.2 Creation of a Phosphosilicate Glass

The MCVD process allows for the creation of glasses that are of high purity and can be tailored both structurally and compositionally, and it is straightforward to implement [6]. While MCVD-derived glasses are mostly SiO_2, other oxides such as P_2O_5

and GeO_2 can be introduced via vapor phase oxidation during the fabrication process due to the availability of precursors with sufficiently high vapor pressures. The resultant bulk glass rods, called preforms, can also be doped with RE via vapor phase or solution doping [7, 8].

Modern high-power fiber lasers use a series of geometries and compositional techniques to achieve the maximum possible output laser powers, efficiencies, and beam qualities [9]. Of interest in this research is the emphasis on the material component of these glasses, and the contribution of the individual components, in part or in whole to these properties in the final fiber. To do this, a phosphosilicate glass will be further modified by incorporating additional amounts of Al_2O_3, Yb_2O_3 and B_2O_3 to create a new active core glass for fiber lasers [10].

In this research we are starting with glass core that contains both SiO_2 and P_2O_5 to create the PS preform via MCVD. The inclusion of P_2O_5 into the SiO_2 host matrix yields several benefits to the optical performance of the fiber, but also significantly changes the material properties compared to a pure SiO_2 glass. Phosphorous forms tetrahedral units like that of silica. However, one of the oxygen atoms is double bonded to phosphorous and is, therefore, non-bridging. When additional dopants such as Al_2O_3 or Yb_2O_3 are added to the glass matrix, the P_2O_5 network increases the number of non-bridging oxygens even further [11]. This reduces the glass viscosity of the core composition, which can be a detriment to MCVD and fiber draw. Further, it lowers the immiscibility barrier of the silica which promotes the increased incorporation of the RE into the host glass [10]. This new phosphosilicate further improve the Yb concentration in the glass when Al_2O_3 is included with the rare earth.

Along with reduced viscosity, P_2O_5 is volatile during the final stages of MCVD fabrication, which occurs at temperatures in excess of 2300°C. During this process, the core can undergo sublimation, which will also remove the RE dopant and Al_2O_3, thus reducing the overall performance of the final fiber laser [12].

The PS core also is highly stressed due to the compositional difference between the core and clad. As the initial amount of phosphorus pentoxide in the core was targeted at 6 weight %, this led to a significant coefficient of thermal expansion (CTE) mismatch between that region and the all silica clad outside of the core, noted in Table I. While sufficiently stable during fabrication, any mechanical perturbations such grinding or sawing of the preform would result in shattering of the core. There were attempts to increase the P_2O_5 concentrations in the glass during MCVD to achieve a higher weight % in the glass. Higher concentrations of P_2O_5 are difficult to achieve via MCVD. The P_2O_5 vapor pressure is higher than that of the SiO_2. At the elevated temperatures of vapor deposition, particularly in the later stages of the process, P_2O_5 readily volatilizes out of the glass, which results in “burnout” region of the core and can be seen as a refractive index difference and concentration of RE difference where the P_2O_5 is lower [10].

While there are some material challenges dealing with PS glass, such as the reduced viscosity, the benefits of the optical characteristics far outweigh the drawbacks. As mentioned, these glasses allow for higher doping concentrations of RE into the host glass, which reduces the overall fiber length required for a high-power laser [13]. A shorter length is beneficial to create a smaller fiber laser device and can mitigate certain parasitic nonlinearities. Further this PS composition exhibits low photodarkening, which leads to higher usage lifetimes of fiber lasers at higher powers [14].

Table 3.1 is a list of common compounds and dopants added to silica. In this table the qualitative effect they have on various physical and optical properties within the host glass are listed. This work will reference back to Table 3.1 as further discussion is given to the additional dopants used in creating this new host glass. All but GeO_2 and fluorine (F) are used in this research for the new host laser glass.

Compound	**Physical****			**Brillouin****			**STRS****	**Raman****	**Wave-Mixing****
	n	ρ	CTE	V_a	$\Delta\nu_B$	p_{12}	dn/dT	V_m	n_2
SiO_2***	1.444	2200	0.55×10^{-6}	5970	17	0.226	10.4×10^{-6}	27.31	2.5×10^{-20}
GeO_2	↑	↑	↑	↓	↑	↑	↑	↑	↑
F	↓	↓	↑	↓			↓		↓
P_2O_5	↑	↑	↑	↓	↑	↑	↓	↑	
B_2O_3	↓	↓	↑	↓	↑	↑	↓	↑	
Al_2O_3	↑	↑	↑	↑	↑	↓	≈	↑	↑
Yb_2O_3	↑	↑		↓		↓		↑	

Table 3.1: General Property Trends on Addition of Noted Compounds into Silica [15]

* Trend strictly valid over homogeneous glass forming range and for the binary composition with silica. Ternary and n-ary glasses may show equivalent trends but will depend on the relative concentrations of each component. Additionally, trends presume that no new phase or structure is formed such as with the mixed alkali effect [16,17] or in the $Al_2O_3 - P_2O_5$ system where both Al_2O_3 and P_2O_5 increase the refractive index, for example, when individually added to silica but decrease it when both Al_2O_3 and P_2O_5 are added in equal proportions to silica due to the formation of $AlPO_4$ [18].

** Property abbreviations and units: n is the linear refractive index [dimensionless], ρ is the density [kg·m^{-3}], CTE is the coefficient of thermal expansion [K^{-1}], V_A is the acoustic velocity [m·s^{-1}], $\Delta\nu_B$ is the Brillouin linewidth [MHz], p_{12} is the transverse photoelastic coefficient [dimensionless], dn/dT is the thermo-optic coefficient [K^{-1}], V_m is the molar volume (cm^3·mol^{-1}), and n_2 is the nonlinear refractive index (m^2·W^{-1}).

*** Values for silica: refractive index, n, measured at a wavelength of 1550 nm. Brillouin linewidth, $\Delta\nu_B$, measured in MHz at a Brillouin frequency of 11 GHz.

3.3 Al_2O_3 doping for enhanced RE solubility in SiO_2

Creating doped preforms via MCVD that are then drawn into laser fibers involves a variety of steps and materials to create a glass with the most desirous properties [6]. Arguably the most critical aspect of this process is including RE ions into the host matrix to form a gain medium for lasing. There are primarily 2 methods by which this is done: vapor phase doping of RE chelates and solution doping [6, 8, 19]. The sole RE incorporation method used in this research is solution doping.

As discussed in Chapter 2, solution doping entails dissolving the RE, usually as $RECl_3$ along with Al_2O_3 in water and soaking this solution into the porous soot of the preform. Rare earth oxides do not readily incorporate on their own into the SiO_2 network without the presence of network modifiers such as Al_2O_3. This is due to the limited solid solubility of in the $RE_2O_3 – SiO_2$ system, which leads to phase separation at fairly low RE oxide concentrations [10, 49]. Solubility of the RE is greatly increased by Al_2O_3, which incorporates readily into silica [20, 22]. The Al_2O_3 also lowers the immiscibility barrier between the materials. Reference [21] contains a thorough treatment on the behavior and importance of Al_2O_3 in creating modern optical fibers, amplifiers, and fiber lasers. For this research, the role of the Al_2O_3 doping is to control the refractive index, facilitate greater rare earth solubility, hence shorter fiber laser lengths and lower nonlinearities, and possibly react with P_2O_5 as a means of further index control, as is discussed later. These aluminophosphosilicate (APS) glasses will also be discussed for their suitable for high-power fiber laser applications.

3.4 Tailoring refractive index materially

Thus far base glass compositions have been discussed in terms of creating a PS glass by including P_2O_5, and then an APS glass by incorporating Al_2O_3 via solution doping. Both materials have their own unique and cooperative properties that contribute to the formation of an optimal bulk laser glass, which is the purpose of this research.

When discussing MCVD, the constituents added to the host glass work to raise the refractive index, save a few exceptions such as Fluorine (F) and B_2O_3 [23]. Referenced in Chapter 2, Figure 2.4 are dopants concentrations versus refractive index used in MCVD to create preforms. Along with the information in Table I, the components discussed thus far to create the APS glass used for this research all increase n when added to the glass, along with the RE component. One of the characteristic criteria for this host glass is to have a flat change in refractive index (Δn) relative to that of silica glass such that one knows the necessary dopant concentration for a desired index. This will be discussed further in this chapter.

If all materials discussed thus far work to increase Δn, there must be a way to reduce it materially. The first method used in this research to reduce the index is the formation of aluminum phosphate, or $AlPO_4$ [24]. It is well established that both Al_2O_3 and P_2O_5 raise the index of silica when incorporated into it. A unique benefit to the material properties is when they react together forming the ≡Al-O-P≡ structure ($AlPO_4$). This preserves the tetrahedral network of the silica glass but reduces the refractive index, n, by creating less polarizable bonds [18, 25 - 28].

Although $AlPO_4$ is beneficial for this research by decreasing the index thus affording higher doping without the negative impact on increasing the numerical aperture, further steps must be taken to tailor the material properties in order to reduce Δn to near zero. In this research, the incorporation of B_2O_3 into the new host APS glass achieves that goal. Recall in Chapter 2, Figure 2.4 that the refractive index is increased by all dopants in that chart except B_2O_3 [29]. During the creation of this RE doped APS glass, B_2O_3 is added during the sintering phase (see Chapter 2) of MCVD by reacting BCl_3 with O_2 to form the boria (B_2O_3) in the core glass. Materially, the B_2O_3 reduces the density of the glass and along with P_2O_5, softens the glass and reduces the viscosity. This enables consolidation of the glass at lower temperatures during MCVD, which reduce the volatilization of the P_2O_5 within the core, as well as any RE species that were doped into the glass. This consolidation at lower temperatures can also reduce the amount of refractive index dip due to core burnout [10].

3.5 Active Aluminophosphosilicate glass with Ytterbium

The discussion in the Chapter thus far has focused on the materials used to create the base glass composition. These compositions are comprised of SiO_2, P_2O_5, Al_2O_3, $AlPO_4$, and B_2O_3. In total, it is a passive boron doped Aluminophosphosilicate glass (BAPS), a suitable laser glass host given the proper understanding of the individual parts and how they interact in the bulk. Also, this composition created and fabricated in straightforward fashion via MCVD, a standard industrial fabrication method for optical preforms.

However, to achieve efficient lasing, a rare earth must be incorporated into the glass in sufficiently high quantity that a fiber can be drawn from the resultant glass, pumped optically, and output laser light at a desired wavelength (λ). [30, 31]. The RE compound that is the focus of this research is ytterbium oxide or Yb_2O_3. This will be abbreviated further in the Chapter as Yb during the materials discussion. Yb doped high power fiber lasers are one of the most common for a variety of applications. Current commercial continuous wave (CW) laser systems can achieve output powers in excess of 100kW [32].

A primary feature of Yb is the simplicity of its electronic energy level structure. The principal Yb^{3+} energy levels are shown in Chapter 1, Figure 1.4. Yb^{3+} possesses two main 4*f* electronic states that are of greatest interest to the high-power fiber laser community: the $^2F_{7/2}$ ground state and the $^2F_{5/2}$ excited state. Absorption and emission between these levels occurs at a wavelength of about 1000 nm.

Other features that have led to the popularity of Yb^{3+} in high energy fiber laser systems also includes the lack of additional excited states that otherwise could lead to excited state absorption or upconversion and the fairly large energy gap between the excited state and ground state, which leads to high efficiency and also a relative ease of population inversion. While a basic two-level system should never lase, the additional stark energy levels within the $^2F_{5/2}$ and $^2F_{7/2}$ enable absorption and lasing at multiple wavelengths; thus Yb behaves as a "pseudo three-level" laser system.

Further, the spectroscopic properties of the Yb^{3+} can be enhanced through careful compositional tailoring of the host glass. Typically, fractional molar percentages of Yb can be doped into typical silica glass. However, an APS glass, such as one employed in this research, can significantly increase the doping level. When P_2O_5 is incorporated into the SiO_2 glass matrix, the phonon energy of the host glass is increased, the amount of non-bridging oxygens increases, and this facilitates greater doping of Yb^{3+} into the glass matrix [34, 58]. As noted by Plotnichenko, the incorporation of P_2O_5 into a SiO_2 glass matrix leads to a series of double phosphorous centers in addition to the silicon-oxygen and phosphorous- oxygen tetrahedra. These various bonds lead to additional non bridging oxygens capable of additional rare earth inclusion to the matrix. Increasing this doping is also facilitated with the incorporation of the Yb with Al_2O_3 to improve solubility as also noted by Ballato and Dragic in [21].

To summarize the individual material constituents in the research dedicated to the creation of a new glass composition for high-power fiber lasers; P_2O_5 is added to a SiO_2 host to create a phosphosilicate glass, which has good solubility for rare earth dopants and low photodarkening. Al_2O_3 is incorporated to create a new aluminophosphosilicate host glass with enhanced Yb solubility. This new Yb doped APS glass is further enhanced and the refractive index is changed by incorporating B_2O_3 and forming $AlPO_4$ to achieve an active glass with a Δn to that of pure silica glass.

3.6 Active Core Glass Creation

A critical challenge in the creation of this core glass is to develop a material via MCVD with a RE doped core that also maintains sufficient uniformity in refractive index. Ideally, this glass also should also be suitable to create fiber lasers with core diameters up to 100 μm (LMA design). Any increase in core sizes over 35 μm will need to exhibit compositional uniformity and uniform refractive index control within the host material. At larger core sizes, any dissimilarities in index or dopant and shape will promote localized guidance in that region of the glass, i.e. not in the core. Any material used in this research must maintain the uniformity if it is to be a successful core glass and avoid this localized guidance outside of the core.

The required uniformity of the index will be influenced by the its dimensions and relative to the index fluctuations. These fluctuations in index can occur if the its size is sufficiently small relative to the wavelength of the light. As core sizes increase, the accuracy of the refractive index becomes more critical. While the original glass created via MCVD will have some variations, the final active core material will be stacked and drawn. The final material will still maintain some similarities to the original structure, but the variations will be small than the optical wavelength that this glass is intended for, which is approximately 1 μm. These smaller scaled dimensions in conjunction with any species diffusion that may occur during MCVD, stack, draw or fiber draw will alleviate these difficult to control parameters, such as index variations.

To begin the process of creating a new glass for high-power fiber lasers, a series of starting compositional variables had to be selected. This was the most logical point for the research, as optical performance could not be completed until stable glass creation via MCVD was completed. The compositional criteria for the glass is in Table 3.2. Boria is not listed as it the capability is not available at the Electron Microscopy facility. Further, there was not material target as one of its principal function was to further reduce Δn, which is measured via refractive index profilometry (RIP)

Material	Target (wt%)	Avg.
Al	1.0	1.1
P	6.0	6.1
Yb	1.0	1.2

Table 3.2: Compositional targets vs. final average of preforms.

In Table 3.2, the averages of the 23 preforms created used in this research is listed in the right column (more detail is provided below). They align with the compositional targets and, as will be revealed, individual preform composition was less critical than an overall composition. The research of the active glass in this chapter is not to create a single preform that will then be drawn into fiber. Rather a series of preforms meeting compositional and optical criteria (Δn) are made and then combined into a single piece of glass. This glass is then used as an active core glass for numerous fiber laser types.

Each APS preform must go through a series of characterization steps to ensure it will meet the intended optical and compositional criteria, which are used as practical bounds on fabrication. After fabrication on the lathe, a sample from the finished tailstock end of the preform is removed, polished to expose the core region, and compositional analysis is performed using a scanning electron microscope (SEM). Samples were analyzed using a weight percent of the compounds present: SiO_2, P_2O_5, Al_2O_3, and Yb_2O_3 by stoichiometry. When needed, especially in the latter parts of this research, boron (i.e., B_2O_3) is added as an index-lowering compound although it is not detectable by the energy dispersive (x-ray) spectroscopy (EDX). If there is compositional difference or drift, the glass is remade and re-characterized.

After SEM / EDX analysis, the preform refractive index profile (RIP) is characterized at 10mm intervals over the entire length of the preform. The profile is given as refractive index difference (Δn), relative to that of silica (1.4570), at a wavelength of 632.8nm. The accuracy in index value is +/- 0.0020. Each step and the acceptance/rejection criteria are followed for each preform until a preform with acceptable index and composition are created as shown in Chapter 2, Figure 2.5.

A total of 23 preforms that fit the material and optical criteria were used in this research. Table 3.3 lists the individual pieces and their corresponding compositional properties. Several preforms, which when created via MCVD, contain more than one useful section to make the final active piece. The first column is an internal identification used for tracking and composition w/w%

Preform:	Al	P	Yb	Yb max	SEM Al:Yb ratio
LA13611	0.75	5.76	1.20	1.80	0.63
LA18811	0.89	5.6	1	1.61	0.89
LA19311	0.98	5.8	1.2	1.5	0.82
LA22311	0.93	5.02	1.20	1.46	0.78
LA23011	0.77	5.69	1.10	1.32	0.70
LA24111	1.32	5.75	1.3	1.64	1.02
LA24511	0.79	5.5	1.3	1.82	0.61
LA24911	1.7	5.74	1	1.35	1.70
LA25111	0.49	4.75	1.00	1.20	0.49
LA25711	0.43	1.7	0.4	0.42	1.08
LA27911	0.91	4.80	0.90	0.96	1.01
LA28511	0.96	5.40	1.00	1.32	0.96
LA29011	1.12	7.60	1.20	1.64	0.93
LA29411	1.45	8.35	1.40	1.83	1.04
LA29911	0.64	6.10	1.30	1.50	0.49
LA31211	0.99	6.40	1.10	1.30	0.90
LA31811	1.66	7.70	1.50	1.68	1.11
LA33311	1.54	6.63	1.40	1.60	1.10
LA33611	1.53	6.51	1.60	1.70	0.96
LA34011	1.49	7.23	1.20	1.70	1.24
LA34211	1.02	8.02	1.30	1.64	0.78
LA34711	0.97	6.43	1.00	1.13	0.97
LA34911	1.50	6.82	1.30	1.52	1.15
Averages Phase 1	**1.08**	**6.06**	**1.17**	**1.46**	**0.93**

Table 3.3: Active preforms created via MCVD and composition.

There were optical properties and goals set for each preform, along with the compositional properties. After a compositional sample was selected from the end of a finished preform, refractive index profiles were measured down the length of the glass rod every 10mm. This data is measured as a change in refractive index Δn versus SiO_2 at 632.8 nm (HeNe wavelength). This difference is plotted and interpreted against the target limits set forth for this research. For the group of preforms listed in Table 3.3, the upper limit Δn value was set at $+1\text{x}10^{-4}$ and a lower value of $-5\text{x}10^{-4}$ against the SiO_2 n of 1.4570. Graphical representation of preform versus these upper and lower limits is in Chapter 2, Figure 2.7.

As represented above, the section between 165 and 325mm (horizontal axis) are within the acceptable Δn range selected for this new glass. This section of preform is then combined with others of comparable composition and index difference to create the final glass. What is of note in this optical characterization of the RIP is that limits set most of the acceptable range below 0. Further, this specific example is completely below 0 Δn. According to the principal of Total Internal Reflection, if this preform was to be drawn to fiber, it should not guide light in the core, as the core is a lower index than the surrounding clad glass. Rather it would antiguide and not fully propagate core light or lase [36].

The selection of these optical constraints being more towards the negative are due mainly to the additional constraints of fabricating via stack and draw (see Chapter 2, also Section 3.6 this chapter). Each preform will be heated to approximately 2000°C and drawn down via standard draw practices to reduce the outside diameter (OD). This will happen twice to achieve the final desired active glass. During this process, there is enough thermal energy to encourage diffusion between the core and clad which could increase the refractive index as diffusion can change the concentration of species such as Al, P and B in the glass. These are some of the principal constituents in use to reduce Δn [23, 37]. Further as there is already a sufficient CTE mismatch between the core and clad materials due the core being a multicomponent glass (Table 3.1), there is expected to be stress induced index changes to increase the refractive index [38, 39]. To compensate for these effects, a more negative Δn limit range has been selected.

Overall the most critical aspect of creating a new glass using different preforms, each with a slight difference in refractive index and composition throughout the length of the glass is that these perturbations must be mitigated to make the final active glass useful for building a fiber laser. Good refractive index control is critical for core sizes in fibers that need to be scaled above standard telecom dimensions for single-mode (SM) performance. The refractive index fluctuations between pieces must be sufficiently smaller than the λ of the light being transmitted so as not to interact. Compositional variations can also be reduced by scaling the pieces down, as the difference between each preform reduces as they are drawn down.

To achieve this goal, stack and draw is employed to decrease the difference index and compositional differences between the preforms. Figure 3.1 represents the evolution of preform from starting dimension after MCVD to the final dimension used in stack and draw. The doped core is extracted from a preform by grinding down the OD. This decreases the amount of undoped glass (SiO_2) that will go into the stack and increase the concentration of active material in the stack.

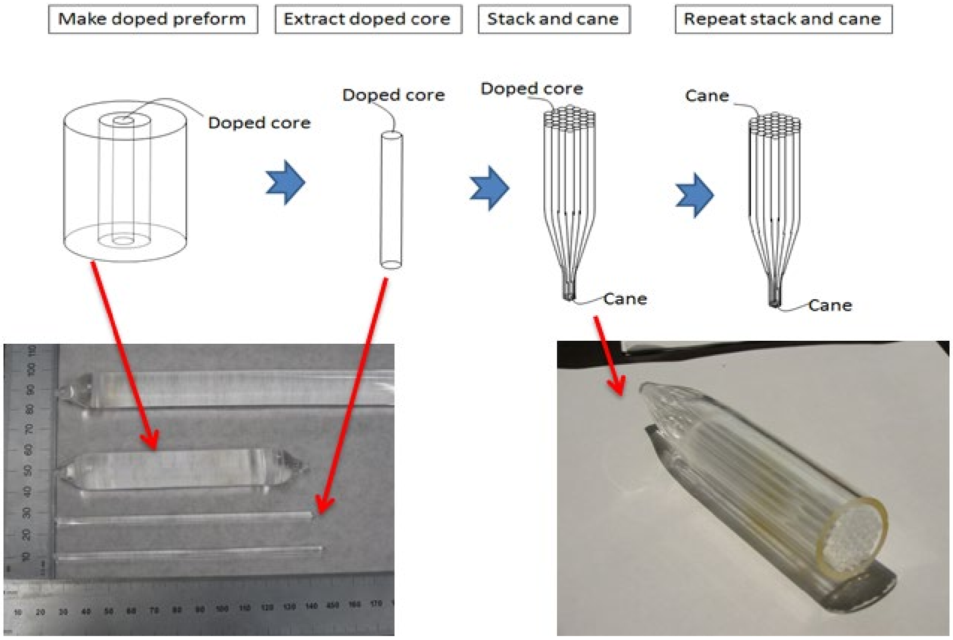

Figure 3.1: Active Glass stack and draw

Once the core of all the pieces created in Table 3.3 are ground, they are stacked together and drawn to a target of 1.5mm. This decreases the variation between each core component in the stack, however it is still insufficient for the final glass. Due to the high amount of non SiO_2 constituents, the glass viscosity is lower than more common glasses drawn at Clemson. Further the amount of starting material is very small, so only a few temperature changes to compensate for the low viscosity could be made before there was no more material. This led to a significant variation in the OD of the pieces. However, as they were to be redrawn a second time, the variation was not recorded.

The second stack and drawn insured the pieces would be more uniform in both composition and index difference across the glass cane, which was 1.5mm after the second draw. The image in Figure 3.2 is the resultant cane after the second draw. On the left is the overall cross section of the cane, which is approximately 1.5mm. The interior region, which contains all the active pieces that were created from the first stack and draw are approximately 1.0mm.

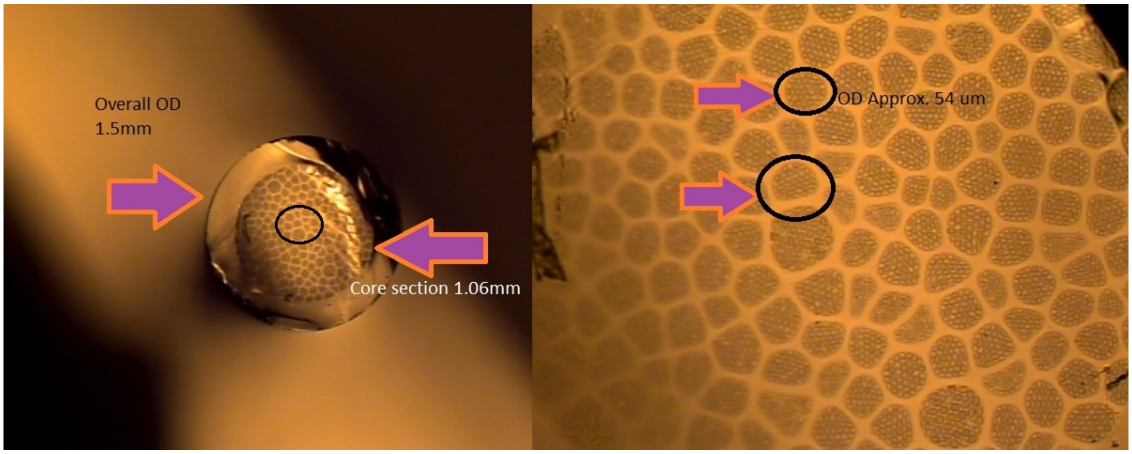

Figure 3.2: Active cane after second consolidation stack and draw. Left is cane cross section. Right is magnified region of active pieces.

The right-hand image of Figure 3.3 is the magnified region of the overall cane. This is to illustrate the scaled down nature of this process. Initially each of those circled regions in black were the original stack. Within each of those circles is all the active cores created in this process and redrawn.

A further increase in magnification of the cane highlights the diameter of each new active piece individually in Figure 3.3. In the white circles within the inset image, the active portions after these consecutive stacks and draws are approximately 9 microns. This is a 3 order of magnitude reduction from starting at 3.2mm (3200 microns) to now 9 microns.

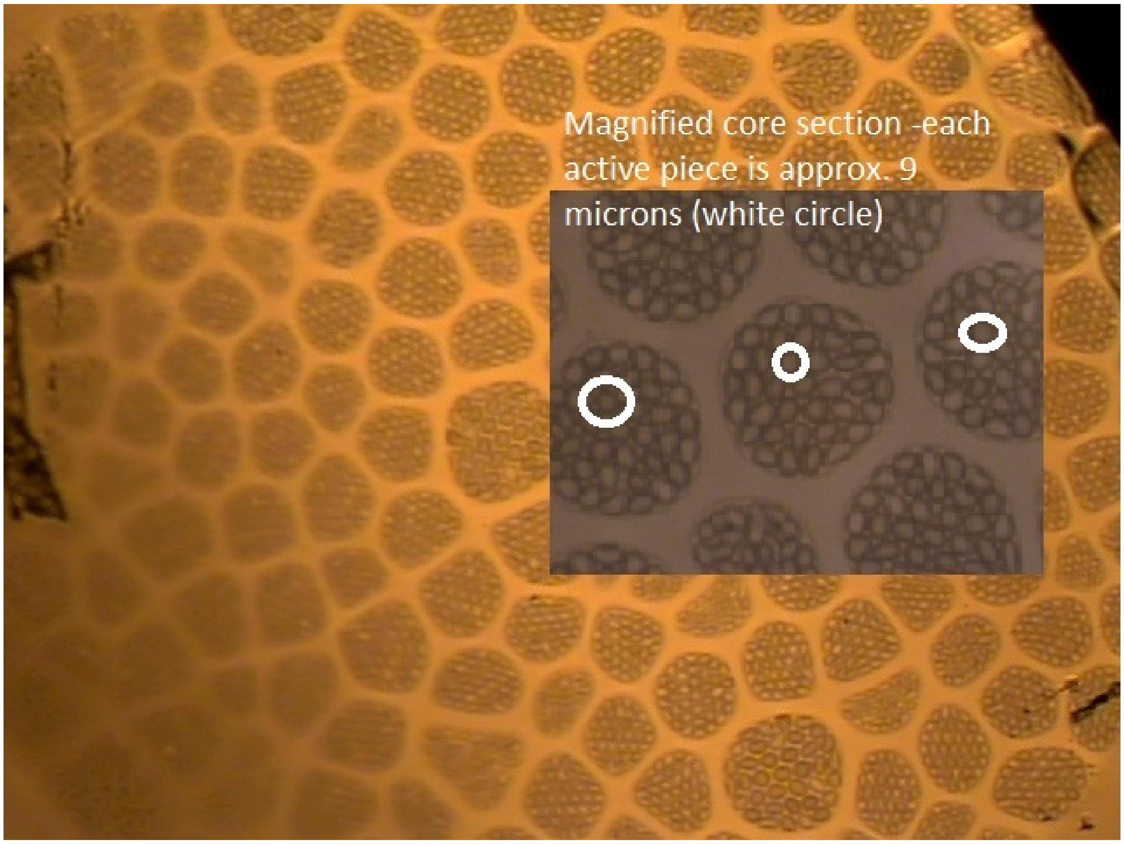

Figure 3.3: Active cane interior with magnification (50x) of preforms.

3.7 Active core integration into fiber

While much of the discussion has been on the active glass creation via MCVD, and the material properties that were targeted, nothing has been mentioned regarding the use of this glass as a fiber laser. The intent of the research at this point was to create a glass that could be used as core in a larger scaled stack and draw process. The main purpose of the significant level of research is to create a single uniform glass type that is sufficiently versatile for creating many new fiber lasers based on design criteria separate from the materials research. The new active core glass (referred to as AC1 now) is homogenous throughout the 10's of meters that were drawn from the multiple stack and draw steps. Further, materially and through the draw process and additional steps that are used to create the fiber laser, it behaves much like a comparable glass made of pure SiO_2 of the same dimensions.

Due to the overall low Δn of this glass, a fiber design was created to enable offset of it by surrounding the core with F doped glass of even lower Δn than the core. This new configuration is a Leaky Channel Fiber design, or LCF [40, 41]. In a LCF design, the fiber is created so that the structure within has certain discontinuity by using materials of different refractive indices and periodicity between the core and cladding structures [42]. These discontinuities build in strong guidance of the Fundamental Mode (FM) within the fiber but are lossy to higher order modes thus creating an effectively single mode fiber.

Briefly, FM guidance in optical fiber, particularly fiber lasers is of great importance to the output power and stability of the laser light. Light through the fiber is a transverse electromagnetic wave, and the various modes are guided in the core of the fiber when it is surrounded by a cladding of lower refractive index [43, 44]. Maxwell's equations yield a generic wave equation, which with dimensions and index of the waveguide (fiber) serve as boundary conditions for this differential wave equation. The solutions to those equations are called the modes. They represent an intensity profile of the light that is being bound by and guided in the fiber. The mode with the most intense spatial distribution of light guided through the waveguide with the least loss or breakup of intensity is the FM [45]. As a fiber is considered a cylindrical waveguide and also a dielectric, it is considered a cylindrical dielectric waveguide. Within this waveguide, the modes have either a magnetic (H), electric (E) or linear combination of these (linear polarized or LP) through the core.

For this LCF design, a series of low Δn glass rods were stacked around a single piece of the active core glass created in this research. Those rods, doped with F, had a Δn of -15.5×10^{-4} lower than that of silica. This was approximately -14×10^{-4} lower than that of the lower limit of the Δn criteria set forth by the research constraints when creating these preforms via MCVD. In Figure 3.4, the proposed fiber cross section and final fiber cross section are shown. The F doped rods are in red (darker in actual fiber), silica in outer regions, and active core (blue in inset) in the center of the fiber.

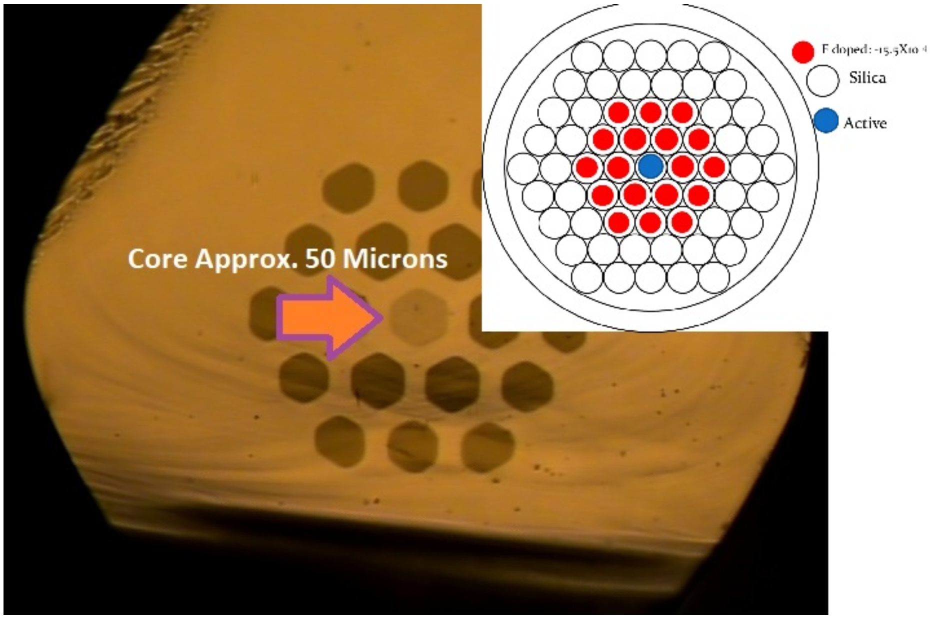

Figure 3.4: LCF fiber cross section and proposed design (inset).

Using a stack and draw process like the one used to create the active core glass, the individual pieces of glass were stacked according to the design in the rig inset of

Figure 3.4 and drawn into fiber. A total of approximately 100 meters were drawn, with an overall fiber dimension of approximately 400 microns, and a core diameter of approximately 50 microns. The hexagonal design is an artifact of the stack-and-draw process. It also serves to strip out higher order modes (HOM) when the fiber is sufficiently bent during testing. These HOM reduce the beam quality of the fiber laser and are, therefore, detrimental to laser performance [46].

The magnified core region of the first LCF fiber made with the active glass is in Figure 3.5. In this image, the highlighted region on the left is the entire cane on the right once the fiberization is complete. This is critical to the performance of the fiber in that the variations in the core region seen in the larger 1.5mm OD active cane are nonexistent optically. Once drawn, the cane has been reduced a further factor of 2 orders of magnitude from 1.5mm to 50 microns. In the core, the active regions that were 50 microns (Figure 3.6) approximately are now only around 1.7 microns. What once was a 3.2mm rod of glass is now scaled down to approximately 300 nm.

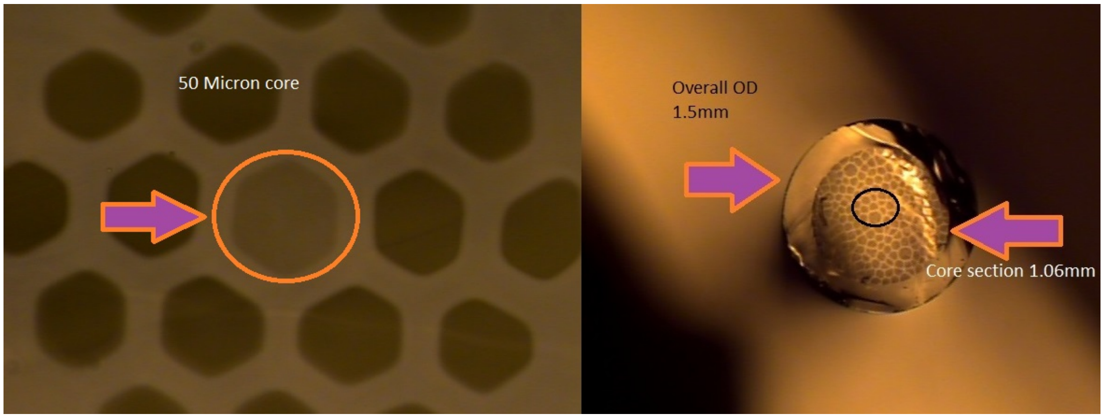

Figure 3.5: LCF fiber with active core (Left); original active core glass (Right)

The first series of confirmation tests ran on this fiber to evaluate the newly created core glass was to evaluate the composition of the core by SEM at Clemson. The compositional values associated with the final core glass did not corroborate with the values measured on the bulk preforms, which was very concerning. A sample was sent for WDS, which would provide a more accurate measurement of the composition, as well as offer a valuable comparison against the measurements at Clemson. Both measurements were consistent with each other and the total Yb content (or Yb_2O_3 content) was around 0.3 weight % across the core, which was almost 1/3 of what was expected to be in the final glass. Further, the Al content was also less than measured in the bulk by roughly half. In the bulk preforms (Table 3.3), the Yb concentration was approximately 1 weight % for all pieces, along with the Al. However, the overall composition in the final fiber (Figure 3.6), was closer to 0.3 weight percent. Boria was in the glass and was not accounted for in either the preform or final fiber measurements as it was not directly measurable using the facilities at Clemson. This can account for some variation, as it is known to be in the glass. However, the expectation was that the final fiber composition would more closely resemble the bulk preform averages in Table 3.3.

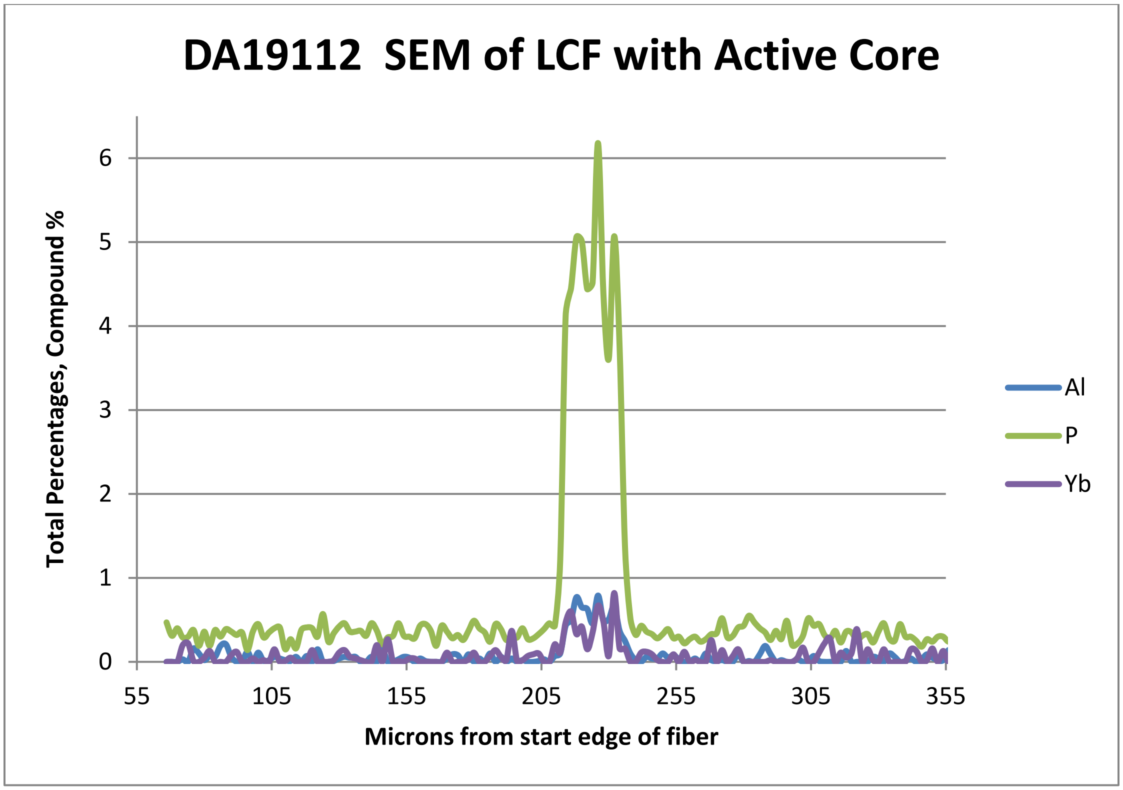

Figure 3.6: SEM of LCF fiber with active core glass.

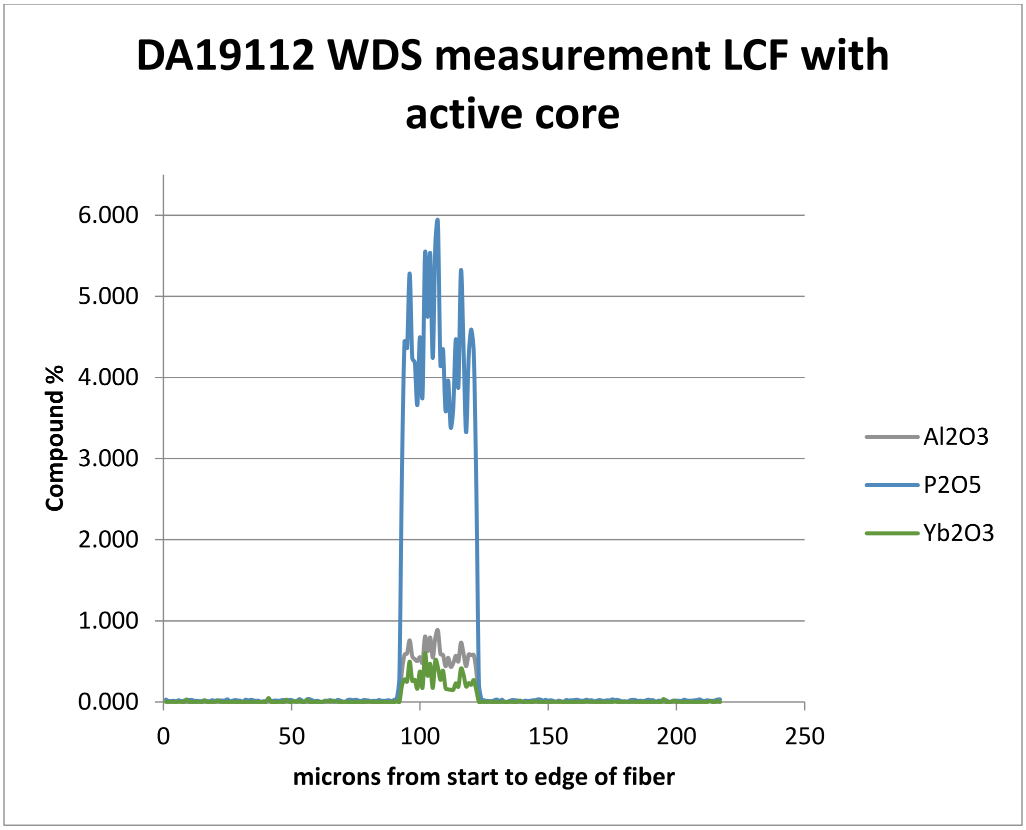

Figure 3.7: WDS of LCF fiber with active core glass.

The main theory regarding composition changes are excessive dilution of the RE ions over the course of the stack and draw processes. This could be from additional cladding around the core pieces, then further addition of silica cladding glass at each subsequent stack and draw step may have reduced the overall concentration. This was not confirmed by directly measuring the change in silica content in the core of the final fiber then comparing it to the preforms themselves, nor was it evaluated during the stack-and-draw processes to measure any dilution of Yb during these intermediate steps. Further, when measuring the index across the entire surface of the core, the composition measurement is combining all constituents, including the SiO_2, which would appear to effectively reduce the RE concentration in the composite core.

After composition, the refractive index profile (RIP) of the fiber was measured along a sample of the fiber cross section using an interferometry method employed by an outside vendor [47]. This sample was taken around 90 meters into the sample of drawn fiber. In Figure 3.8, a cross sectional RIP of the fiber is shown. The region labeled CORE is depressed relative to the 0.0000 Δn axis. Using the raw data, the depressed region is -1.7×10-4 Δn less than that of SiO_2. The expectation was that the Δn would increase due to the various constituents and diffusion of the glass through the various stack and draw steps, moving up closer to the upper limit of $+1\times10^{-4}$. What is surprising is that it continued to stay below the Δn of 0.00 of silica.

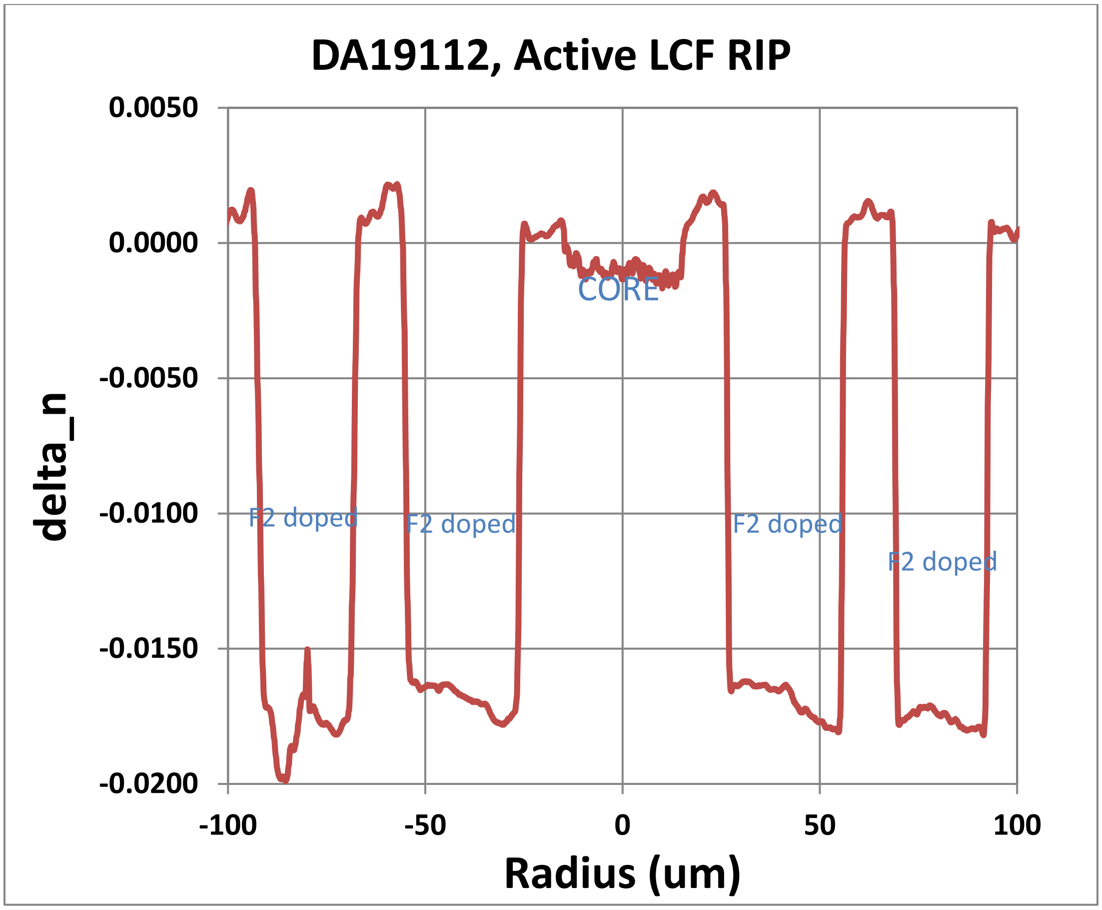

Figure 3.8: LCF fiber with active core RIP

To confirm that this was not something anomalous with the fiber drawing or stack and draw process, and to confirm that it is an issue with the active core glass, a new fiber was made using the same active glass and redrawn to fiber. The Δn was also measured and is plotted against the first fiber drawn in Figure 3.9

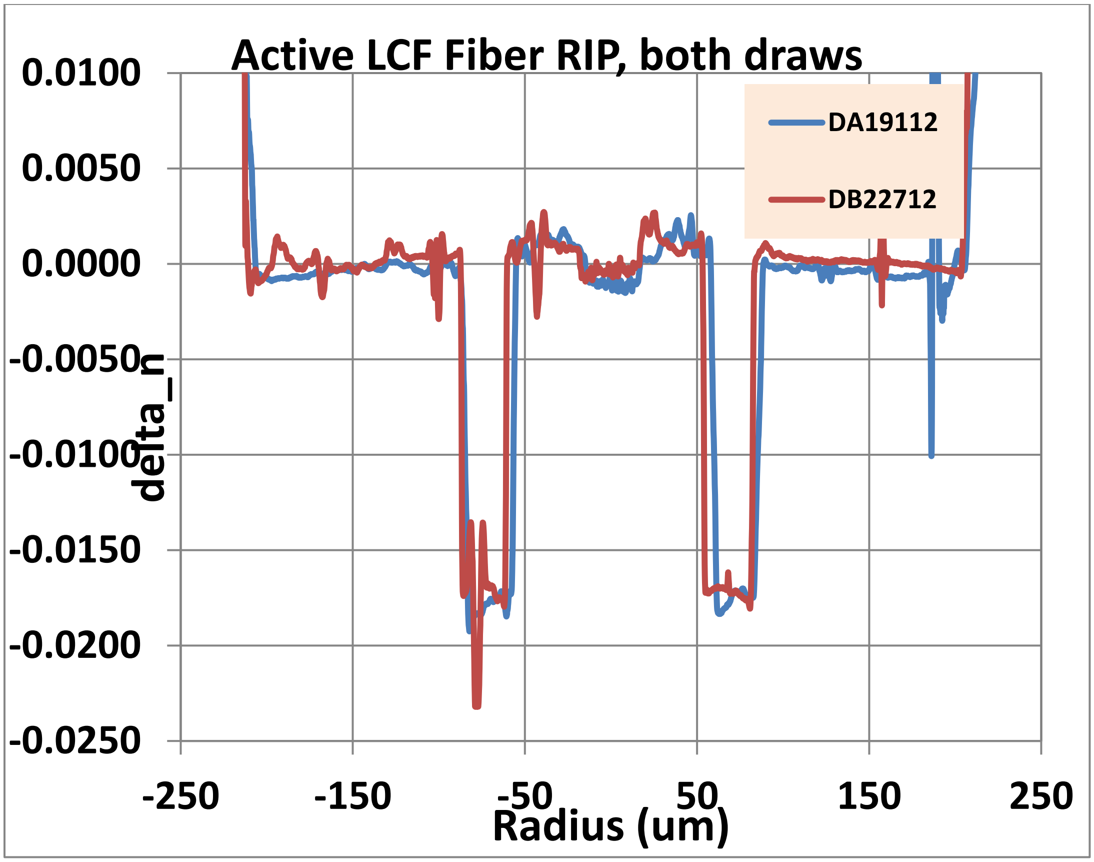

Figure 3.9: LCF fibers, both draws, RIP.

This data confirmed that it was indeed due to the core glass. Both fibers exhibit consistent dips along the same region of active core. From a compositional perspective, the Yb content was too low to be a viable glass for a fiber laser as the desired concentration was at least 1 wt%. There appeared to be decreases in both the Al and Yb content from the start of the process with creating preforms via MCVD, to the final step of creating and using the glass a core for a fiber laser. Further the Δn was below that of silica. The core would not effectively guide the FM through the core. This was further supported by the LCF fiber configuration used to evaluate the core glass. The much lower index F doped glass should have mitigated any anti-guiding by the core, provided the index was sufficiently positive [48].

Lastly, the final confirmation of the performance of the active core glass was completed during evaluation of mode guidance of light. Light with wavelength of approximately 1 micron was coupled to the fiber and an image of the output mode was captured with an infrared camera. If the core and resultant structure were of positive index and leaking the HOM, respectively, most of the light would be guided in the core, and not leaking between the F doped regions. In Figure 3.10, The cross section is shown with the pump light coupled and guided. The bright areas are regions outside of the core, which remains dark. In this figure, the modes are guided in the clad region and outside of the core itself, which is the bright portion of the image. Due to the lower index in the core region, the light is not guiding in the core. It was at this stage of the research that a new approach and revision to composition and index is needed to create the desired active core glass for high-power lasers.

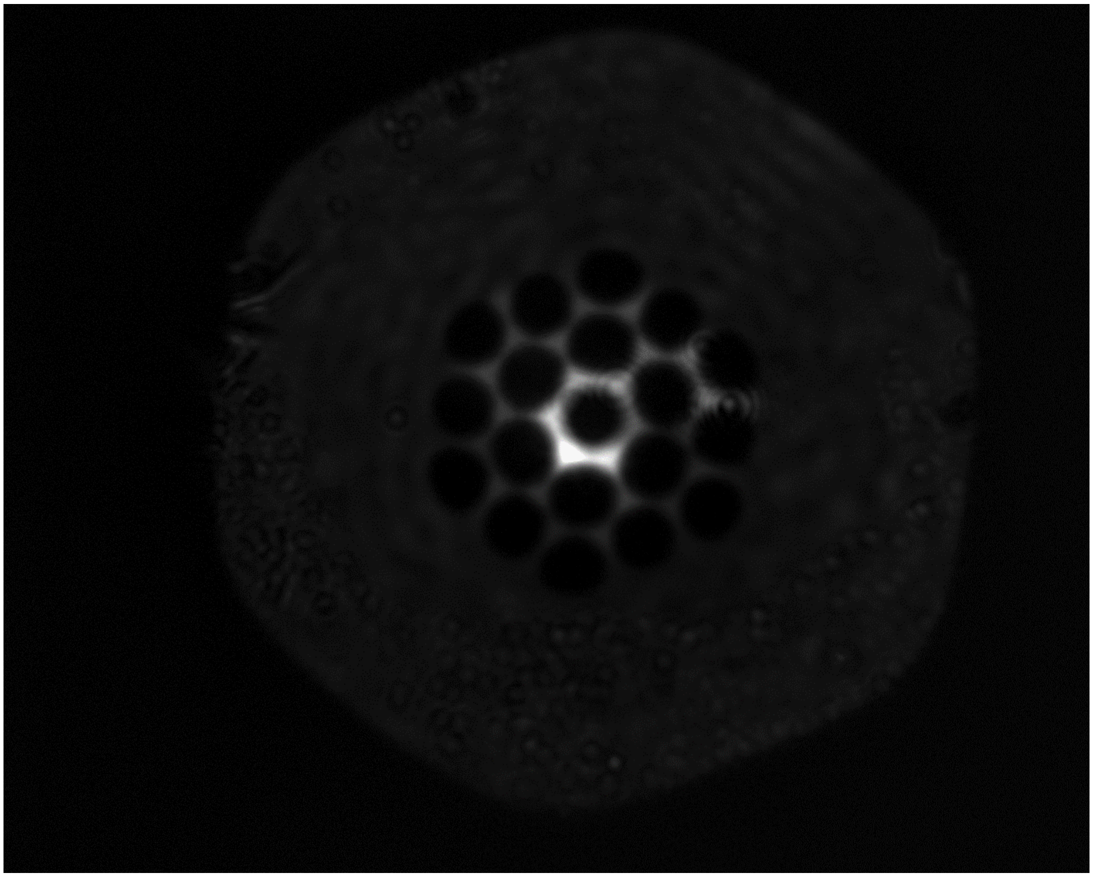
Figure 3.10: Mode pattern of LCF.

3.8 Active Core Glass Reevaluation and Revision

Following the creation of the active glass (AC1) and evaluation of its performance, material and optical properties as a core for a fiber laser, it was clear that the criteria are not sufficient to make a functional host for high power fiber lasers without significant changes. A new set of criteria and changes to the targets for AC1 were chosen based on the knowledge gained from this first glass. When the choices for index criteria and Yb concentration were selected, one of the key components was that they be conservative values. This was due to the process of creating many preforms with such an index and composition, grinding, then stacking and drawing multiple times was a new undertaking. The AC1 version of the glass was also a trial run of sorts. Once the results of the initial glass were evaluated in a fiber laser design and results such as Δn were deemed too low, more aggressive compositional and Δn research levels were set.

The two key compositional changes between AC1 and the revised active glass (AC2) were the level of Yb_2O_3 concentration in the glass, as well as the levels of Al_2O_3. For AC1, the assumed conservative levels were closer to 1 wt%. The Yb concentration target was increased to 3 wt%, compared to 1 wt% in AC1. For the Al content, that amount was more than doubled in AC2, compared to the initial glass composition in AC1. Table 3.4 compares the Al, P, and Yb weight % between both AC1 and AC2.

Regarding the increase in Yb concentrations from AC1 to AC2, the higher Yb content would promote higher lasing threshold as the concentrations of RE for a given length of fiber would be higher. This in turn would enable a greater amount of laser output for the same length of fiber over the AC1 concentration. However, as Yb does not readily incorporate into a silica glass, the Al concentration was also increased to improve the solubility of the higher amount of Yb to be doped into the glass. Further, the Al/P ratio changing will increase the amount of $AlPO_4$ in the glass, which will offset the index increase by the increased Yb concentration, as $AlPO_4$ decreases the index.

The levels of P_2O_5 were not changed in AC2 as the composition of the glass proved sufficiently low viscosity compared to pure silica for the further stack and draw steps. Also due to the high vapor pressure of P_2O_5, it is more prone to volatilization out of the core during the high consolidation temperatures of MCVD, leading to a dip in the index of the core due to burn-off [10]. Since the glass in AC1 was sufficiently stable from an MCVD fabrication standpoint, it was determined that increasing the P_2O_5 would deviate the material criteria further and increase the time needed to create a new composition, as the higher levels in the silica glass would change the characteristics too greatly.

wt%	Al	P	Yb	Yb max
AC1 glass	1.1	6.1	1.2	1.5
AC2 glass	2.5	5.9	3.2	4.0

Table 3.4: Compositional comparison between AC1 and AC2 active glass

To achieve the increase in Yb and Al concentrations, the doping solution used for introducing these constituents was modified. Discussed in Chapter 2 is greater detail regarding the introduction of RE via solution doping for MCVD. Table 3.5 lists the approximates solution changes to achieve the increase in Yb and Al in the new active glass. Both the $YbCl_3$ and $AlCl_3$ were in hexahydrate form ($6H_2O$) and the $AlCl_3$ neared full saturation due to the amount in the solution. The Yb and Al ratios in the solution were increased to achieve higher doping of the Yb in the glass, and to improve the solubility of it by increasing the Al. Further, this increases the amount of $AlPO_4$ created in the glass to reduce the index. The higher Yb content compared to AC1 will increase the index, so must be mitigated to achieve a Δn of 0 relative to silica.

	YbCl3 (g)	AlCl3 (g)	H2O (ml)
AC1	25	75	500
AC2	41	300	250

Table 3.5: Concentrations of doping solutions from AC1 to AC2

An increase in Yb concentration of the active glass will proved the benefit of a shorter fiber length for lasing. This is due to the increased Yb levels will enable higher gain over a shorter distance of the glass fiber. This will in turn reduce the overall device side, once the fiber has been created and proven to be an effective fiber laser host. The increase of Yb and Al also increase the density of the glass and, in the case of Al, increases the acoustic velocity and Brillouin spectral linewidth. These material properties along with an increase in density, increase the overall Brillouin Gain Coefficient, and work to increase the SBS threshold in a fiber laser, the lowest threshold parasitic nonlinearity in high-power fiber lasers (See section 1.5.1 on SBS).

With the increase in Yb, comes the need to improve the solubility of the RE into the glass. This is one of the reasons for the increase in level of Al_2O_3in the glass for AC2. Aluminum oxide doping improves solubility of the RE in the glass matrix, and it is discussed in detail in Ref. [21]. Further, it lowers the immiscibility range between the RE oxide and SiO_2, allowing for a homogenization of the RE and less opportunity for clustering in the host glass, and improving the homogenization of the RE in the glass [49]. Further it decreases the thermodynamic opportunity of the glass core composition to phase separate [50]. Lastly, it also increases the refractive index and density.

The resultant Δn in AC1 when the glass was used in a LCF fiber design proved to be too low to effectively guide light in the core. For AC2, the optimal ranges were increased closer to $\Delta n = 0$. Further, the limits of acceptable index variation was greatly decreased, which would decrease the number of acceptable preforms that could be created in the same timeframe. However, we were confident that the limits of creating this host glass via MCVD had not been reached.

The data in Table 3.6 lists a summary and comparison of the various Δn targets between AC1 and AC2. The key value is the change from AC1 to AC2. This new reduction in Δn represents a 75% reduction in acceptable range of index fluctuation that can be used to create this new final active core glass AC2 for a given preform created via MCVD.

	Upper limit	Lower limit	Range
AC1	1.0E-04	-5.0E-04	6.0E-04
AC2	5.0E-05	-1.0E-04	1.5E-04
		Change from AC1 to AC2	4.5E-04

Table 3.6: Compositional comparison between AC1 and AC2 active glass

Materially this reduction creates significant challenge from the standpoint if creating this glass via MCVD. Most preforms fabricated will not fit the criteria of both composition and a more stringent Δn range. However, the new upper and lower limits that are now shifted further positive will eliminate the previous issue of anti-guiding as seen with AC2.

A graph in Figure 3.11 gives a more visual representation of the changes to the Δn between the groups of glasses created in AC1 and AC2. Not only is the new range for AC2 smaller, but the both the upper and lower limits are much closer to a Δn of 0, with an average target of -2.5×10^{-5} for a preform. The range of indices for AC2 is decreased by more than half.

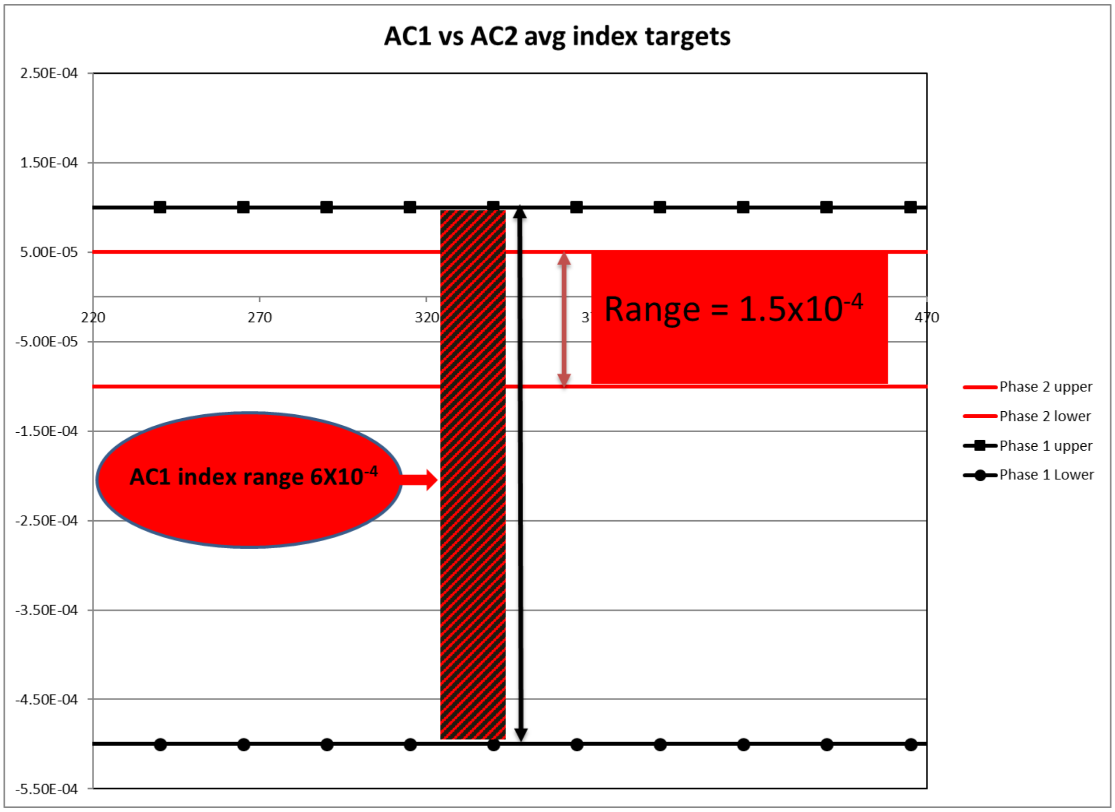

Figure 3.11: AC1 and AC2 index range comparison.

As with AC1, new preforms were created, characterized for composition, as well as refractive index. Once a sufficient number of preforms were created, the OD was reduced to 3.2mm, then stacked and drawn down twice to achieve a uniform cane of active glass AC2 with an OD of 1.5mm that can be incorporated into a new fiber laser design. Compositionally, the new preforms did have an increased Al and Yb concentration over AC1, while maintaining the previous levels of P in the glass. Table 3.7 lists the preforms and average compositions for AC2, along with a comparison of the averages against AC1 at the bottom.

Preform:	Al	P	Yb	Yb max
LA34912	2.98	6.16	4.02	5.51
LA01013	2.71	6.21	3.26	4.75
LA01513	2.39	6.22	3.23	4.11
LA02113	2.24	5.89	2.60	3.06
LA02213	2.92	5.77	3.60	4.27
LA02313	2.07	5.56	3.11	3.54
LA03213	1.61	5.49	2.24	2.75
LA03713	2.50	6.30	2.98	3.70
LA03913	2.61	5.12	3.57	5.08
LA04913	2.49	6.10	3.19	4.31
LA05113	2.26	5.85	2.74	3.43
LA06413	2.99	6.29	4.05	5.12
LA06513	2.74	6.05	3.45	4.36
LA06713	2.11	5.84	2.69	3.27
LA07113	2.43	5.94	3.11	3.55
LA07313	2.50	5.61	3.42	4.32
LA07913	2.38	6.05	2.97	3.39
LA08413	2.41	5.92	3.06	3.73
Averages AC2	**2.46**	**5.91**	**3.18**	**4.01**
Averages AC1	1.08	6.06	1.17	1.46

Table 3.7: AC2 SEM and compositional information.

Creating the new active glass followed the same steps as in AC1. First the canes were stacked and drawn, then restacked and redrawn to increase uniformity. The final cane cross section and scale of the active regions is shown in Figure 3.12

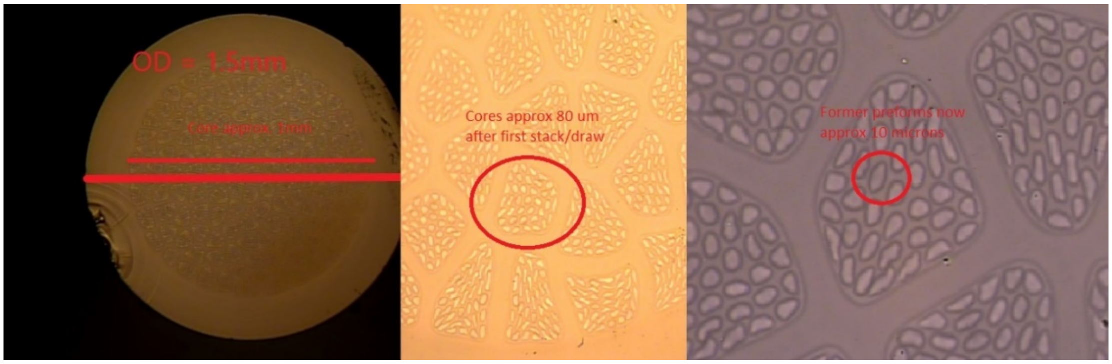

Figure 3.12: AC2 active cane after stack and draws.

In Figure 3.12, the resultant preforms that were originally 16mm, then reduced in OD to 3.2mm, are now approximately 10 microns. They will be further reduced when integrated into a fiber as the active core material as AC2. The reduction and restacking process takes over 100 pieces of canes generated in the first stack and draw step, then reduces again. The result is around 5000 original ground and stacked preforms in the final cane. Once this cane is drawn to fiber, the original active preform will be below 1 μm and appear uniform to the light, as the active RE is Yb and will operate in the approximately 1 μm regime.

The creation of AC2 group of active core glass prompted a repeat use in the LCF design for AC1. Structurally and materially it was identical to the LCF discussed in section 3.7 of this Chapter and performed well with optimal guidance. However, as that fiber was for an outside research collaborator, the final performance information was not fully shared. Only that the fiber did guide successfully. Visually, the core in AC2 more closely matches the silica cladding, which is indicative of a closer Δn match than the core glass created as AC1. Figure 3.13 shows the AC1 glass on the left, and the same fiber configuration on the right with AC2. The AC2 core glass more closely resembles the all silica clad region outside of the F doped pieces. In the image on the right, the AC1 glass core is darker than the surrounding silica clad, indicating a depressed index relative to it.

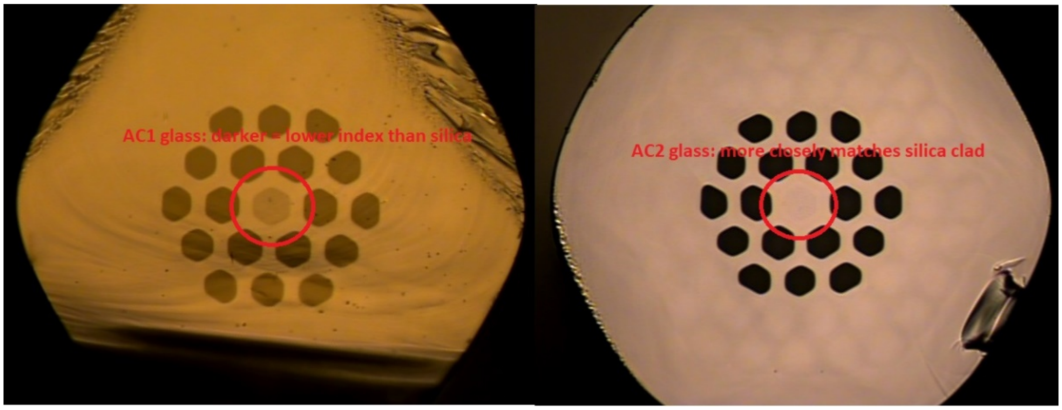

Figure 3.13: Comparison of AC1 and AC2 cores in identical LCF configuration

After the LCF work with AC2, a new photonic bandgap fiber (PBGF) design was created to evaluate the ability of AC2 to operate as a large core fiber laser host. In a PBGF, there is a significant amount of periodicity build into the design of the fiber. This is done using a standard stack and draw process, where materials of differing indices are combined and stacked in such a way as to promote or prevent certain frequencies, or wavelengths of light, from guiding, while allowing others to be guided in the core of the glass [54, 56, 57]. This periodicity can come from air holes or solid rods of higher or lower refractive indices. A common choice is germanium doped rods, where the index is higher than the surrounding silica pieces. The photonic bandgap (PBG) will stop light at certain wavelengths and angles of incident into the fiber from propagating through the material while allowing others to propagate. The bandgap originates due to arranging dielectrics, i.e. glass, periodically so that some frequencies are allowed while others are forbidden.

The PBGF configuration is shown in Figure 3.14. In this fiber design, there are 3 constituent glasses in use. First, the circles in grey are all silica. The red dots indicate GeO_2 doped rods to promote the periodicity. The size of this GeO_2 nodes and spacing determine the bandgap of allowed frequencies and will determine what is effectively guided in the core region. The seven purple core pieces are the AC2 glass stacked as the core. This core in the final fiber (right side Figure 3.14) is approximately 50 μm across.

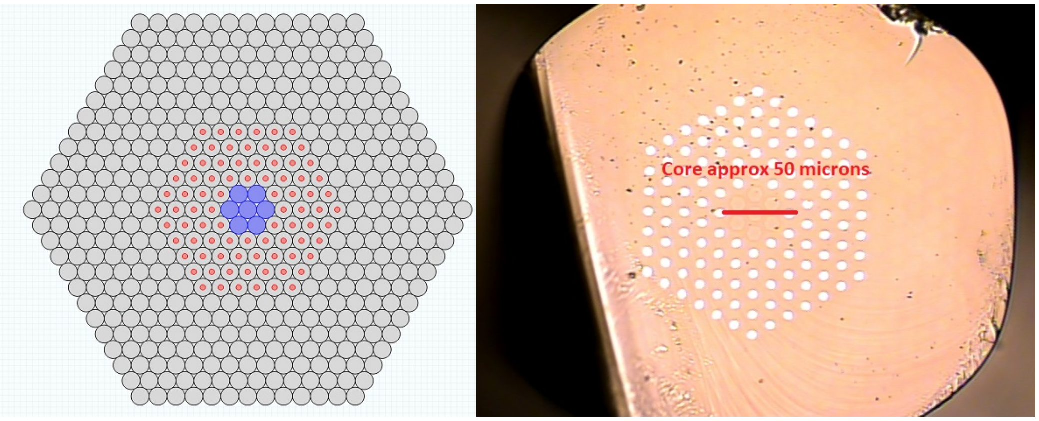

Figure 3.17: PBGF fiber design and final cross section

In this final fiber, as mentioned previously, the light guided will see a uniform core region due to the multiple stack and draw processes. For example, the AC2 cane, which is 1.5mm across, has measured nodes within the core of approximately 10 microns. After stacking and drawing to create this PBGF in Figure 3.14, these differences are on the scale of 300 nm. The incoming pump light at approximately 1 μm would not discern any differences across this core region. This active glass and its performance as a fiber laser, is treated to vigorous analysis and optical characterization and modeling in references [42, 46, 52 – 57].

3.9 Summary, Conclusions and Future Work

The purpose of the research in this Chapter was to create and study the compositional and fabrication influences of new active glass hosts for use as core phases in advanced high-power fiber laser designs. The glass should be a phosphosilicate composition and be doped with Yb_2O_3 as the active component. Aluminum oxide was added to improve solubility of the RE ion and tailor the refractive index and reduce nonlinearities (this will be further discussed in the next Chapter). This new glass should also have a Δn of nearly zero relative to pure silica. Initial conditions were determined for the composition, as well as Δn boundaries and a series of preforms were created that met the criteria and boundaries. This glass was stacked and drawn multiple times to create a new core material AC1. This glass was used in an LCF fiber design, but the Δn was not sufficiently high to guide. Further the Yb content was lower than anticipated.

Based on this new glass and the processing steps created to make it, new compositional targets were created that increased Yb as well as Al content in the glass. The Δn was also increased as well as the acceptable range was decreased by 75% for a much stricter set of boundary conditions. New preforms were created via MCVD and followed identical stack and draw conditions to create AC2, the newest active core glass. This glass was incorporated into the same LCF design and performed successfully.

There was significant time spent on optimization, but the changes associated with these steps all tie back to the Materials Science of the research. First, the Yb concentration was kept low due to the poor solubility of it into a silica-based glass. This is improved by using Al to lower the immiscibility barrier and further promote solubility, along with adding P_2O_5 to create a phosphosilicate glass host, which further increase the solubility of the Yb. This doping concentration was increased from AC1 to AC2 to improve the lasing properties of a host glass by raising the concentration of Yb. However, to raise it in the host phosphosilicate glass, further addition of Al was added to improve the solubility of the higher concentration rare earth, as well as form $AlPO_4$.

An optimization property of this research was to create a host glass that was the same Δn as that of silica at 632.8nm. Most materials that are incorporated into the host glass via MCVD raise the refractive index. The exceptions are F, B_2O_3, and $AlPO_4$. In this research, the increase in Yb, known to raise the refractive index, was offset by addition of higher concentrations of Al to help solubility. It also has the added benefit of creating higher amounts of $AlPO_4$ in the glass as well. Further adjustments in the index are lowered by increasing the concentration of B_2O_3 in the glass. However, due to limitations of the measurements available, this was not measured directly. Only through an Edisonian process of creating a preform, characterizing, then adjusting gas flows was this done with a regular amount of repeatability.

Optically, this material exhibited preferred characteristics suitable for high-power laser applications. Phosphosilicate glasses, due to their glass structure, are low photodarkening hosts for Yb as a laser glass. This is important as it increases the lifetime of the laser created using the material. Higher concentrations of B_2O_3 and P_2O_5 reduce the thermo-optic coefficient in a material (dn/dT), a known material property that is shown to increase the threshold onset of TMI (see Chapter 4), a parasitic nonlinearity in high-power fiber lasers. Further, changes in concentration of P_2O_5, Al_2O_3, and Yb_2O_3 increase the density of the glass. This density increase reduces the Brillouin Gain Coefficient (BGC), which reduces the onset of Stimulated Brillouin Scattering (SBS) another parasitic nonlinearity that inhibits high-power in fiber lasers by increasing the threshold with which it occurs. SBS has the lowest threshold of propagation of the most common parasitic nonlinearities. All these oxide additives to the host silica glass increase the onset of SBS, not just through the increased density, but their contribution to the other acousto-optic properties in the BGC term, such as acoustic velocity and Brillouin Linewidth (Chapter 1, Section 1.5.1)

Following the completion of the LCF fiber, the AC2 material was included in a new series of PBGF for high-power laser applications. These fibers also performed well with the new AC2 material, including achieving high lasing powers with high efficiency. The research to create a new phosphosilicate glass doped with Al and Yb as a host material for high power lasers has been successful. This AC2 glass performance as a fiber laser is treated more fully in references [42] and [52 – 57].

Based on the research into this new active glass, the material is the foundation for creating a new low thermo-optic coefficient fiber, where optical nonlinearities in fiber lasers are dealt with by tailoring the material composition. This research building upon the active core glass is discussed further in Chapter 4.

Moving forward regarding new active glass compositions, the next steps include increasing the Yb content of the host glass even further up to 6 wt%, which will double the best efforts in our research thus far. This will include increases to both the Al and P concentrations in the material as well. Further, the Δn boundaries are increased to higher level, so the new glass should achieve a Δn at 0 relative to silica. New methods of characterization are also to be implemented which will reduce the number of preforms required for fabrication. These include using an additivity model to predict the optical performance of the glass based on compositional criteria and bulk measurements. Heat treatment and intermediate draws will also be included to evaluate the Δn of the preform prior to stack and draw to reduce variability in the final index of the active core material. Steps are also going to be taken to further reduce the amount of silica cladding around the active core, which will improve Δn uniformity in the final glass. These include acid etching to reduce the clad layers of the ground cores, as well as intermediate etching steps between stack and draw steps.

3.10 References

1. J. B. MacChesney, P. B. O'Connor, F. V. DiMarcello, J. R. Simpson, and P. D. Lazay, "Preparation of low loss optical fibers using simultaneous vapor deposition and fusion", *Proc. 10th Int'l Congress on glass*, Kyoto Japan 1974.

2. J. B. MacChesney, P. B. O'Connor, F. V. DiMarcello, J. R. Simpson, and P. D. Lazay, "A new technique for preparation of low-loss and graded index optical fibers"", *Proc. IEEE*, vol. 62, September 1974

3. John. B. MacChesney, Paul B. O'Conner. *US Patent #4,217,027*," Optical Fiber Fabrication and Resulting Products
4. A. Smith and J. Smith, "Mode instability in high power fiber amplifiers," *Optics Express 19,* 10180-10192 (2011)
5. P. D. Dragic, M. Cavillon, A. Ballato, and J. Ballato, "A Unified Materials Approach to Mitigating Optical Nonlinearities in Optical Fiber. II. A. Material Additivity Models and Basic Glass Properties," *International Journal of Applied Glass Science* **9**, 278 – 287 (2018).
6. S. Nagel, J. B. MacChesney, K. Walker, "An Overview of the Modified Chemical Vapor Deposition (MCVD) Process and Performance", *IEEE Transactaion on Microwave Theory and Techniques*, Vol. MTT-30, No. 4, April 1982.
7. R. P. Tumminelli, B. C. McCollum, and E. Snitzer, "Fabrication of high-concentration rare-earth doped optical fibers using chelates," *J. Lightwave Technol.*, vol. 8, Nov. 1990.

8. J. E. Townsend, S. B. Poole, and D. N. Payne, “Solution doping technique for fabrication of rare earth doped optical fibers,” *Electronics Let*ters, vol. 23, pp. 329–331, 1987.

9. D. J. Richardson, J. Nilsson, W. A. Clarkson, “High power fiber lasers: current status and future perspectives”, *Journal of the Optical Society of America B,* Vol. 27, No. 11, pg B63 – B92 (2010)

10. G. Vienne, J. Caplen, L. Dong, J. Minelly, J. Nilsson, D. Payne, “Fabrication and Characterization of Yb^{3+}: Er^{3+} Phosphosilicate Fibers for Lasers”, *Journal of Lightwave Technology*, Vol. 16, No. 11, November 199

11. U. Hoppe, “A structural model for phosphate glasses,” *Journal of Non-Crystalline Solids*, no. 195, pp. 138–147, 1996.

12. C. Gao, Z. Huang, Y. Wang, H. Zhan, L. Ni, K. Peng, Y. Li, Z. Jia, X. Wang, A. You, J. Wang, F. Jing, H. Lin, A. Lin, “Yb-doped Aluminophosphosilicate Laser Fiber”, *Journal of Lighwave Technology*, Vol. 34, No. 22, November 2016

13. S. Suzuki, H. McKay, X. Peng, L. Fu, L. Dong, “Highly ytterbium-doped silica fibers with low photo-darkening*”, Optics Express*, Vol. 17, No. 12, June 2009.

14. M. Engholm, P. Jelger, F. Laurell, and L. Norin, "Improved photodarkening resistivity in ytterbium-doped fiber lasers by cerium codoping," *Optics Letters*. 34, 1285-1287 (2009)

15. T. Hawkins, J. Ballato, P. Dragic, “A Unified Materials Approach to Mitigating Optical Nonlinearities in Optical Fiber. IV. Opportunities for Vapor Phase Processing” (publication in process)

16. J. Isard, “The mixed alkali effect in glass”, *Journal of Non-Crystalline Solids*. 1969;1:235-261.

17. M. Ingram, “The mixed alkali effect revisited-a new look at an old problem” *Glastech Ber*. 1994;67:151-155.

18. D. DiGiovanni, J. MacChesney, T. Kometani, “Structure and properties of silica containing aluminum and phosphorus near the $AlPO_4$ join:, *Journal of Noncrystalline Solids*. 1989;113:58-64.

19. T. F. Morse, L. Reinhart, A. Kilian, W. Risen Jr., J. W. Cipolla Jr., "Aerosol Doping Technique For MCVD And OVD," *Proc. SPIE* 1171, Fiber Laser Sources and Amplifiers, (15 February 1990);

20. L. Dong, B. Samson, *Fiber Lasers; Basics, Technology and Applications*, CRC Press, 2017.

21. J. Ballato, P. Dragic, “On the clustering of rare earth dopants in fiber lasers”, *Journal of Directed Energy* 6, pg 175 – 181 (2017)

22. K. Arai, H. Namikawa, K. Kumata, T. Honda, Y. Ishii, T. Handa, “aluminum or phosphorous co-doping effects on the fluoresence and structural properties of neodymium-doped silica glass”, *Journal of Applied Physics*, 1986.

23. P. Schultz, “Recent advances in optical fiber maerials” *Proc. 2nd. Int. Otto Schott Colloqium,* July, 1982, Akad. D. Wissenschaften, Jena.

24. N. Yu, T. W. Hawkins, T.-V. Bui, M. Cavillon, J. Ballato, P. D. Dragic, “$AlPO_4$ in Silica Glass Optical Fibers: Deduction of Properties,” *IEEE Photonics Journal* (Vol. 11, Number 5, October 2019); DOI: 10.1109/JPHOT.2019.2941487

25. S. Unger, A. Schwuchow, J. Dellith, and J. Kirchhof, “Codoped materials for high power fiber lasers – diffusion behaviour and optical properties,” *Proceedings of the SPIE*, vol. 6469, page 646913 (2007).
26. S. Jetschke, S. Unger, A. Schwuchow, M. Leich, and J. Kirchhof, “Efficient Yb laser fibers with low photodarkening by optimization of the core composition,” *Optics Express*, vol. 16, no. 20, pp. 15540-15545 (2008).
27. J. Koponen, M. Söderlund, S. Tammela, and H. Po, “Photodarkening in ytterbium-doped silica fibers,” *Proceedings of the SPIE*, vol. 5990, pp. 599008 (2005).
28. S.Kuhn, S. Hein, C. Hupel, J. Nold, N. Haarlammert, T. Schreiber, R. Eberhardt, and A. Tünnermann, “Modelling and the refractive index behavior of Al,P-doped SiO_2, fabricated by means of all-solution doping, in the vicinity of Al:P = 1:1,” *Optical Materials Express*, vol. 8, no. 5, pp. 1328 – 1340 (2018).
29. H. Presby, I. Kaminov, “Binary silica optical fibers: refractive index and profile dospersion measurements”, *Applied Optics,* Vol. 15, No. 12, December 1976
30. A. Schawlow, C. Townes, “Infrared and Optical Masers”, *Physical Review*, Vol. 112, No. 6, December 1958
31. E. Snitzer, “Optical maser Action of Nd^{+3} in a Barium Crown Glass”, *Physical Review Letters*, Vol. 7, No. 12, December 1961
32. https://www.ipgphotonics.com/en/products/lasers/high-power-cw-fiber-lasers
33. J. He, X. Liang, J. Li, H. Yu, “LD pumped Yb:LuAG Mode-Locked laser with 763 ps duration”, *Optics Express*, Vol. 17, No. 14, pg 11537 – 11542 (2009)

34. V. G. Plotnickenko, V. O. Sokolov, V. V. Koltashev, E. M. Dianov, "On the structure of phosphosilicate glasses", *Journal of Non-crystalline Solids*, Vol. 306, pg 209 – 226 (2002).
35. J. Senior, "*Optical Fiber Communications:Principles and Practice, Second Ed.*", Prentice Hall 1991.
36. A. E. Siegman, "Gain-guided, index-antiguided fiber lasers," *Journal of the Optical Society of America B*, 24, 1677-1682 (2007)
37. M. Cavillon, P. Dragic, B. Faugas, T. W. Hawkins, J. Ballato, "Insights and Aspects to the Modeling of the Molten Core Method for Optical Fiber Fabrication", *Materials* 2019, *12*, 2898.
38. P. Dragic, M. Cavillon, A. Ballato, and J. Ballato, "A Unified Materials Approach to Mitigating Optical Nonlinearities in Optical Fiber. II. A. Material additivity models and basic glass properties," *International Journal of Applied Glass Science* (2018).
39. Paek UC, Kurkjian CR. "Calculation of cooling rate and induced stresses in drawing of optical fibers", *Journal of the American Ceram Soc*iety 1975;58:330-335
40. L. Dong, H. A. Mckay, A. Marcinkevicius, L. Fu, J. Li, B. K. Thomas, and M. E. Fermann, "Extending effective area of fundamental mode in optical fibers, " *IEEE Journal of Lightwave Technology,* **27**, 1565-1570 (2009).

41. L. Dong, H. A. Mckay, L. Fu, M. Ohta, A. Marcinkevicius, S. Suzuki, and M. E. Fermann, “Ytterbium doped all glass leakage channel fibers with highly fluorine-doped silica pump cladding” *Optics Express* **17**, 8962-8969(2009).
42. L. Dong, F. Kong, G. Gu, T.W. Hawkins, J. Parsons, M. Jones, C. Dunn, M.T. Kalichevsky-Dong, K. Saitoh, B. Pulford, and I. Dajani, “Large mode area Yb-doped photonic bandgap fiber lasers,” *SPIE Photonics West*, *invited talk*, paper 9344-1, San Francisco, February 2015
43. E. Snitzer, “Cylindrical Dielectric Waveguide Modes”, *Journal of the Optical Society of America,* Vol. 51, No. 5, 1961
44. E. Snitzer, H. Osterberg, “Observed Dielectric Waveguide Modes in the Visible Spectrum”, *Journal of the Optical Society of America*, Vol. 51, No. 5, 1961
45. F. Kong, G. Gu, T.W. Hawkins, J. Parsons, M. Jones, C. Dunn, M.T. Kalichevsky-Dong, K. Wei, B. Samson, and L. Dong, “Flat-top mode from a 50 µm-core Yb-doped leakage channel fiber,” *Optics Express*, Vol. 21, No. 26, pg 32371-32376 (2013).
46. G. Gu, F. Kong, T. Hawkins, P. Foy, K. Wei, B. Samson, and L. Dong, “Measurements of Mode Losses in ~ 50 µm Core Resonantly Enhanced Leakage channel Fibers,” *Advanced Solid State Lasers Congress* AM4A.04, 2013.
47. http://www.interfiberanalysis.com/

48. R. Sims, V. Sudesh, T. McComb, Y. Chen, M. Bass, M. Richardson, A. G. James, J. Ballato, and A. E. Siegman, "Diode-pumped very large core, gain guided, index antiguided single mode fiber laser," in *Advanced Solid-State Photonics*, OSA Technical Digest Series (CD) (Optical Society of America, 2009), paper WB3.

49. B. Hatta, M. Tomozawa,,"Effect of Al_2O_3 on phase separation of SiO_2-Nd_2O_3 glasses", *Journal of. Non-Crystal Solids* 354, 3184 (2008).

50. V. McGahay, M. Tomozawa, "Phase separation in rare-earth-doped SiO_2 glasses", *Journal of. Non-Crystal Solids* 159, issue 3, (1993).

51. F. Poletti, M. Petrovich, D. Richardson, "Hollow-core photonics bandgap fibers: technology and applications, "*Nanophotonics,* 2013, 2(5-6), 315 – 340.

52. G. Gu, F. Kong, T. Hawkins, J. Parsons, M. Jones, C. Dunn, M.T. Kalichevsky-Dong, K. Saitoh, and L. Dong, "Ytterbium-doped large-mode-area all-solid photonic bandgap fiber lasers," *Optics Express* 22, 13962-13968(2014).

53. F. Kong, G. Gu, T.W. Hawkins, J. Parsons, M. Jones, C. Dunn, M.T. Kalichevsky-Dong, B. Pulford, I. Dajani, K. Saitoh, S.P. Palese, E. Cheung, and L. Dong, "Polarizing ytterbium-doped all-solid photonic bandgap fiber with ~1150µm2 effective mode area," *Optics Express* 23, 4307-4312 (2015).

54. B. Pulford, T. Ehrenreich, R. Holten, F. Kong, T.W. Hawkins, L. Dong, and I. Dajani, "400 W near diffraction-limited single-frequency all-solid photonic bandgap fiber amplifier," *Optics Letters* 40, 2297-2300 (2015).

55. G. Gu, Z. Liu, F. Kong, H. Tam, R.K. Shori and L. Dong, "Highly efficient ytterbium-doped phosphosilicate fiber lasers operating below 1020nm," *Optics Express* 23(14), 17693-17700 (2015).
56. L. Dong, F. Kong, G. Gu, T.W. Hawkins, M. Jones, J. Parsons, M.T. Kalichevsky-Dong, K. Saitoh, B. Pulford, and I. Dajani, "Large-Mode-Area All-Solid Photonic Bandgap Fibers for the Mitigation of Optical Nonlinearities," *Journal of Selected Topics in Quantum Electronics* 22, invited paper, 4900207 (2016).
57. F. Kong, G. Gu, T.W. Hawkins, M. Jones, J, Parsons, M.T. Kalichevsky-Dong, S.P. Palese, E. Cheung, and L. Dong, "Efficient 240W single-mode 1018nm laser from an Ytterbium-doped 50/400μm all-solid photonic bandgap fiber," *Optics Express* 26(3), 3138-3144 (2018).
58. F. Galeener, J. Mikkelsen, R. Geils, W. Mosby, "The relative Raman cross sections of vitreous SiO_2, GeO_2, B_2O_3, and P_2O_5", *Applied Physics Letters*, 1978

CHAPTER 4

LOW THERMO-OPTIC COEFFICIENT FIBER

4.1 Introduction and Background

This Chapter studies and advances our understanding of the material science associated with power-scaling in high power optical fiber-based lasers otherwise limited by transverse mode instability (TMI). While most fibers being designed for HEL applications are based on large mode area designs, this research continues the approach of focusing on the materials from which the optical fibers are made. Parasitic nonlinear effects such as TMI fundamentally arise from “mixed effects” in the material; i.e., coupling between optical, thermal, mechanical, etc. fields and their resultant influence on material properties. For example, In the present case, modal instabilities are associated with the material’s thermo-optic coefficient (dn/dT), which promote coupling between modes in a large mode area (LMA) fiber. More specifically, this Chapter will design, model, fabricate, and test optical fibers made using low thermo-optic core glass compositions in order to develop a fundamental understanding of glass composition on optical properties and laser performance [1].

4.2 Thermally-driven Optical Nonlinearities

The materials science of thermally driven optical nonlinearities relates to Stimulated Thermal Rayleigh Scattering (STRS), which is accepted as manifesting transverse mode instability (TMI) in LMA rare-earth doped fiber lasers operating at high optical powers [3]. LMA fiber designs are employed for most high-power fibers lasers because the optical power is spread out over a larger area thus reducing the effective intensity below a threshold value where the nonlinearities become stimulated. Generally speaking, LMA intrinsically are multimode waveguides and "effectively single mode" operation is achieved through engineering of the fiber design. As the fiber laser scales to higher power, heat is generated through non-radiative processes and is non-uniformly distributed along the fiber. This heat, through the thermo-optic effect ($dn/dT \neq 0$), then facilitates mode-coupling. Since the heat is non-uniform, the mode coupling is dynamic and leads to so-called mode instabilities [2]. Following *Dong's* formalism [3], the (nonlinear) coupling between modes, $LP_{mn} \propto g01$ goes as

$$g_{01}\chi_{mn} \propto \frac{(dn/dT)}{\rho \cdot c_p}\left(\frac{\lambda_s}{\lambda_p} - 1\right) f(\Gamma_{ml}^{-1}). \qquad (1)$$

Here, χ is the coupling coefficient where subscripts m and n are the azimuthal and radial mode numbers, respectively, associated with the linearly polarized (LP) modes in a cylindrical optical fiber; i.e., LP_{mn}, and g_{01} is the gain of the fundamental (lowest order, LP_{01}) mode. The other parameters involved in the first righthand-side term of Eqn. (1) are the thermo-optic coefficient, dn/dT, density, ρ, and specific heat, c_p. The second righthand-side term, $(\lambda_s/\lambda_p - 1)$, is the "quantum defect," which is proportional to the energetic difference between each pump and signal quantum value and represents the amount of energy that can be converted to heat through non-radiative processes. Such "quantum defect heating," is the principal source of heat generated during the operation of fiber lasers. The last term in Eqn. (1) denotes a function of the damping factor, Γ_{ml}, which is proportional to the thermal diffusivity, D, given by $D = \kappa/\rho c_p$, where κ is the thermal conductivity. For the purposes of this Dissertation, it is note-worthy that these are all materials-related factors and, therefore, the glass composition can be an effective way to attack mode instabilities.

More specifically, materially, the TMI threshold is proportional to $\rho \cdot c_p/(dn/dT)$. Additionally, the damping factor is proportional to the thermal conductivity and inversely so with heat capacity and density; though the dependencies of threshold and damping factor on heat capacity and density are different and so these factors do not cancel out. Of the factors that influence STRS, the thermo-optic coefficient, dn/dT, is the best to target materially through judicious choice of components possessing positive (SiO_2, GeO_2, Al_2O_3) and negative (P_2O_5, B_2O_3) thermo-optic coefficients, as shown in Figure 4.1 [37, 43].

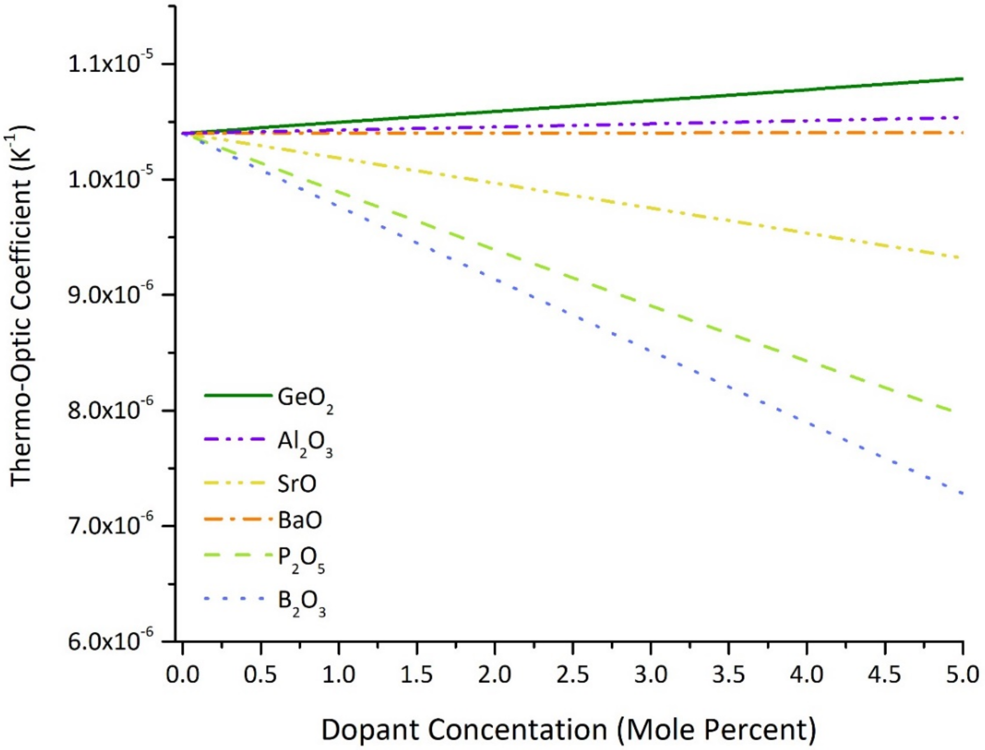

Figure 4.1: Common dopants and effect on Thermo-optic coefficient [37] [43]

4.3 Low Thermo-optic Coefficient Preform and Fiber Fabrication

Since all preforms and fibers prepared for this dissertation shared a common MCVD approach, those generalized details are provided here, but greater detail on the numerous fabrication steps are treated to a more rigorous review in Chapter 2. Initially, the objective of a low dn/dT fiber was achieved quite quickly. However, a secondary objective in order to more directly compare fiber performance was to create a preform equivalent to a commercial LMA laser fiber (i.e., Coherent's LMA-YDF-20/400 fiber). To achieve this, the initial preform recipe used to create the low dn/dT fiber had to be modified through numerous iterations. The optimal NA of the preform had to match that of the Coherent fiber. The Yb content had to be reduced, along with adjustments to the Al and P concentrations. Lastly, the boron content had to be maximized for a low dn/dT under these additional fiber design constraints. As noted above, boron, in the form of boria (B_2O_3) considerably reduces the thermo-optic coefficient when added into SiO_2 and, thus, potentially plays an important role materially reducing TMI. However, boria also reduces the refractive index of SiO_2, as does $AlPO_4$ (arising from reactions between the Al_2O_3 and P_2O_5 co-dopants), and so thoughtful understanding and tailoring of core glass composition is critical to balancing low thermo-optic while also maintaining a desirous waveguide design.

This balance between waveguide design and materials selection led to further movement away from the initial lowest dn/dT condition and led to problems with fabrication of the preforms that had to be addressed. The pre-sinter and sintering phases of the fabrication process had to be adjusted to optimize the absorption of the Yb dopant into the soot by ensuring the soot layer of the core was sufficiently porous to promote this absorption. Too dense and no Yb ions will incorporate. Too porous and soft, and the soot will not sufficiently adhere to the wall of the substrate tube. Figure 4.2 lists a series of developmental milestones for this thermo-optic fiber starting with the initial preform created (P1) which exhibited a greater than 50% dn/dT reduction, to the final fiber created that was drawn to fiber by our industrial collaborator.

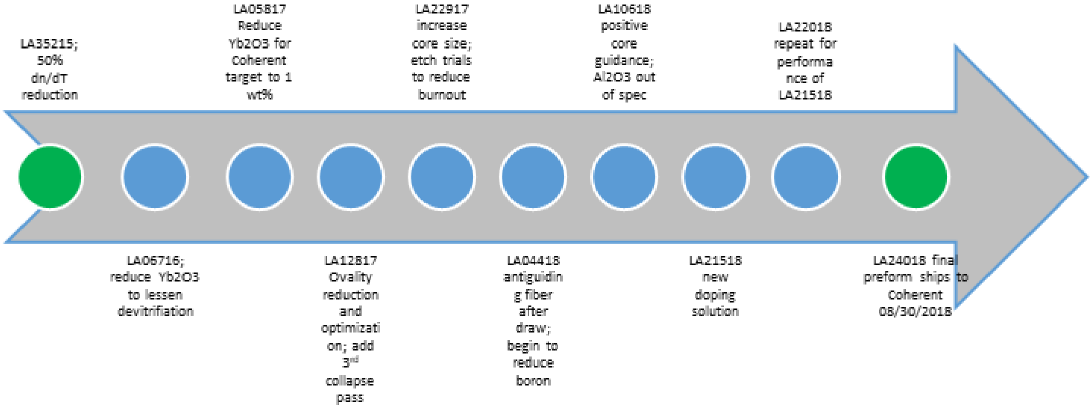

Figure 4.2: Notable milestones during creation of low thermo-optic fiber.

The research completed in Chapter 3 aided this low thermo-optic fiber materials understanding, and it served as a starting point compositionally with which to begin further research into tailoring the material properties to mitigate optical nonlinearities. Recall that in Chapter 3, a phosphosilicate glass doped with Yb and Al at elevated concentrations was created. For the low thermo-optic fiber, this served as the beginning composition to evaluate the existing behavior and properties of the glass. The influence of the materials used in the glass in Chapter 3 and how they affected both material and optical properties related to nonlinearities, (See Table I, Chapter 3).

Over the duration of this research, approximately 70 preforms were created. Many changes in the processing were done and the properties were evaluated on the bulk glass, and in some cases the preform was drawn into fiber to test and measure things such as composition or behavior of the dn/dT of the glass. MCVD properties such as presinter temperature were adjusted and evaluated. For example, in some preforms the temperature was decreased to 1150ºC from 1175ºC as the higher temperature proved to be so hot that it was increasing the density of the soot, reducing the absorption of the Yb in some preforms. In some other cases the core deposition speed increased from -33 to -36mm/min. This led to issues with the consolidation phase of fabrication, which also had to be changed by gradually decreasing the OD over a greater number of passes. To accomplish this, a third collapse pass was added to improve straightness and ovality, and the speeds of pass 1 and 2 were increased to create a more gradual diameter reduction. Each parameter change required analysis of the NA and composition relative to the targets. For example, the new collapse speeds further promoted core burnoff as the phosphosilicate soot is under elevated temperatures for longer periods of time. These changes led to a different concentration of $AlPO_4$ in the glass, which, upon drawing test fibers, resulted in the index further reducing after drawing to fiber. This is because $AlPO_4$ is an index-reducing additive to SiO_2 and, though useful for tailoring the index in highly doped glasses, can be overdone as was the case here [33, 45]. The result was an index anti-guiding fiber composition that had to be compensated for by a decrease in boron content, to raise the refractive index to promote waveguiding, which led to further study of the NA and composition after each subsequent reduction in boron. For the final preform, the Boron content, measured in flow rate, was at 20 sccm, which was down from 100 sccm for the first preforms exhibiting the best dn/dT performance. The refractive index range was sufficient to achieve an NA of 0.06, but also be positive after fiber draw. Lastly the Yb concentration in the final preform achieved a target of 1 wt % Yb_2O_3.

In this research, while the journey from starting preform to the final fiber is important, many branches off the path were for optimization and resulted in either dead ends or reverting back to previous conditions. Therefore, each preform created will not be addressed in the is writing. Rather, the first preform (P1) and the final preform (P2) are of greater concern. Some portions of this Chapter do focus on glass created that exhibited deleterious effects such as Δn decreasing from the bulk glass to the final fiber, as in Section 4.8 regarding B_2O_3 content during fiberization.

To aid in this comparison of changes from initial research of this material to the final preform and resultant fiber created, Table I summarizes relevant material properties and fiber nonlinearity measurements of P1 and P2. The benchmark preform, P1 is a composition created form research into a Yb doped aluminosilicate glass for fiber lasers (Chapter 3). This catalized the research that followed within this chapter and the mitigation of nonlinearities via material properties, such as dn/dT. It was also proven viable as an active glass host in fiber lasers [27, 46 – 51]. P2 is the resultant preform that led to the fiber results in section 4.9

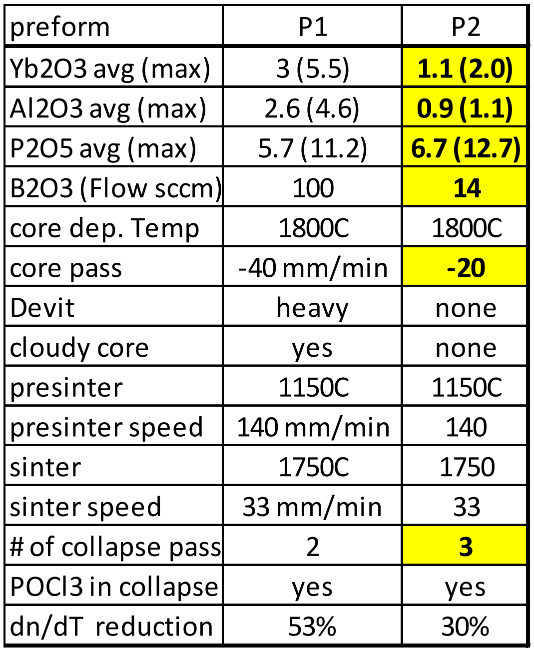

preform	P1	P2
Yb2O3 avg (max)	3 (5.5)	**1.1 (2.0)**
Al2O3 avg (max)	2.6 (4.6)	**0.9 (1.1)**
P2O5 avg (max)	5.7 (11.2)	**6.7 (12.7)**
B2O3 (Flow sccm)	100	**14**
core dep. Temp	1800C	1800C
core pass	-40 mm/min	**-20**
Devit	heavy	none
cloudy core	yes	none
presinter	1150C	1150C
presinter speed	140 mm/min	140
sinter	1750C	1750
sinter speed	33 mm/min	33
# of collapse pass	2	**3**
POCl3 in collapse	yes	yes
dn/dT reduction	53%	30%

Table 4.1: Summary of properties and nonlinearity results in low dn/dT research.

In order to explain further the digression from the initial preform that exhibited the maximum reduction in dn/dT; The earlier preform that exhibited the lowest dn/dT performance (P1, Table 4.1) also contained 3 to 4 weight % of Yb_2O_3, with a maximum at 5.5%, it possessed heavy ovality, as well as significant devitrification in the core region after preform fabrication. The devitrification was due to the high Yb content and its immiscibility in SiO_2 [16, 54] The refractive index profile (RIP) of this lowest dn/dT preform also exhibited a high degree of variation along the preform length, which needed to be addressed. Materially, this is due to lower viscosity of the glass to a purse silica composition [16]. During chemical vapor deposition, the glass is exposed to very high temperatures above the softening point of the composition of the core material. This in turn causes the P_2O_5 and B_2O_3 components to volatilize out of the glass. Further, the core is in a quasi-molten state during the collapse and consolidation phases (See Chapter 2).

This low viscosity glass will soften and deform as it is being rotated along with compositional changes due to volatilization. These issues prevented a direct comparison to a commercially available fiber from Coherent unless changed, although they did not prevent us from drawing the preform to fiber and testing. Analysis of a sample of the fiber from Coherent , as well as discussions with their scientists provided new insights into the development of the glass composition.

First, the Yb content had to be reduced to near one weight % to insure equivalent optical gain in the final fiber laser. Further, higher concentrations of Yb lead to immiscibility in SiO_2 glass, which increases phase separation in the core. This can be mitigated by increasing Al_2O_3 to improve the solubility of the rare earth, but these higher compositions would deviate from the goal of being comparable to the COTS fiber [54, 13]. Lastly, the dn/dT of the Coherent fiber was measured, and a model of expected performance was created (detailed in the next Section) based on the current data on the bulk preforms and drawn fiber. This model would help predict the dn/dT performance based on composition of the glass, as well as the bulk and fiber index. Accordingly, it provides insight into the influences of each compositional dopant on the material properties at play in TMI mitigation.

The process parameters of ovality improvement, index variation, dn/dT performance by maximization of boron content, and reduction of Yb in the glass influenced each other when changed. For example, when the ovality was improved by adjustment of the consolidation steps, the index and thus NA shifted higher to the 0.06 value needed. This was due to the increase in viscosity of the core glass by reducing the concentration of Al, Yb, and B. The less viscous glass exhibits less core burnoff from these more volatile constituents. When the Yb concentration was reduced, the consolidation conditions and amount of P_2O_5 shifted, which then had to be addressed. When the Yb was reduced, this required a decrease in Al in the glass, as less is needed to improve the solubility of the Yb into the SiO_2 host. These material concentration reductions decreased the density of the glass, and it increased the viscosity. These, in turn, affected the concentration of P2O5 retained in the core, which had to be increased to the desired level by increasing precursor flows during vapor deposition. Each parameter adjustment would either directly or indirectly change the conditions of one or more other parameter that did not need changing. Similar to Chapter 3, when a processing parameter changed via MCVD, such as precursor flow increase or decrease of $POCl_3$, for example, this has an effect on the composition of the core. This composition change affects material properties such as density, solubility of the Yb into the glass, viscosity, and refractive index (Chapter 3, Table I). Any change had to be characterized by SEM for composition and refractive index measurement.

After the ovality, devitrification, and compositions were optimized, fibers were drawn from the preforms. From a Materials Engineering standpoint, a processing parameter such as ovality must be addressed as a non-circular core does not guide light as one that is round. Further, this non-circular rod of glass will be exposed to a different thermal profile during MCVD than one that is straight. Some sections of the glass will be exposed to the burner for longer times, and this will lead to compositional non-uniformity as some species will volatilize out of the glass at different regions. Devitrification, or phase separation, in the core is another sign of compositional non-uniformity. This is especially important in active glass as fiber lasers drawn from it would have different optical properties and lasing characteristics if composition shifts between regions of the fiber. Further, the devitrification can act as a source of optical scattering or heat generation, reducing the overall efficiency of the fiber as a laser.

The initial NA and composition were consistent with the insights receive on the COTS fiber. The fibers were drawn with a 20 micron core in order to mimic the Coherent fiber used as a baseline in order for us to better understand the materials contributions of the dopants to reduce TMI while also permitting a practical fiber design. The drawn fiber was index anti-guiding due to $AlPO_4$ formation that was induced by the fiber draw process (glass heated to about 2000°C), that was not present in the bulk. While the bulk glass experiences high temperature (> 2200°C), which would promote some chemical reactions between the individual components, the draw down to the small dimensions of the fiber core (20 μm) facilitates reactions given the shortened reaction distances. This effect was confirmed by further fiber draw, as well as heat treating a preform on the lathe and then measuring the refractive index of the bulk glass and comparing the post heat treatment data to the pre-heat treatment data at the same position along the length of the preform. In Section 4.8, and Figure 4.12, this is measured in the bulk glass (preform) and then drawn to fiber. What is shown in this figure is the change in index of the core from positive (above $\Delta n = 0$) to negative Δn.

In order to solve this issue, the index had to be increased sufficiently so that the post-draw index reduction maintained a positive value. The Al_2O_3 and P_2O_5 compositions were not changed, as any adjustment to these levels would move the fiber design away from the target by modifying the indices, hence NA, of the core. The most direct approach was to modify the boron precursor gas (BCl_3) flow, hence boria concentration in the resultant glass, during preform fabrication. This flow was incrementally reduced, then each preform evaluated for composition and index change. Several fibers were drawn to a 20 micron core and tested for dn/dT performance, composition, as well as fiber refractive index. The preform and recipe that best fit the conditions of NA, ovality, minimal devitrification, Yb concentration, predicted dn/dT performance, and optimal $AlPO_4$ interaction to promote a positive index post-draw in a region shipped to Coherent for over-clad and draw.

4.4 Material Additivity Modeling

Material additivity models advanced by *Dragic* were employed to deduce idealized compositions for subsequent fabrication and testing [4, 5]. The effective dn/dT value for boria was found to be less in fiber than what had been reported for bulk glasses ($-3.5 \times 10^{-5}\ K^{-1}$) whereas values for Al_2O_3 and SiO_2 were similar in fiber form to those in the literature ($dn/dT = +1.05 \times 10^{-5}\ K^{-1}$). To better understand this effect, a geometric model was developed that included both the material contributions and those of the core / clad fiber design.

In general, a material clad by another of lower coefficient of thermal expansion (CTE) will experience its thermal expansion restricted; potentially canceling desirable negative contributions to dn/dT. This restricted expansion can be likened to a positive compression of the glass at elevated temperature; modeled by invoking the photoelastic effect (and constants). By leveraging Profs. Dragic and Ballato's previous experience, a corrected model for the refractive index as a function of temperature that takes core and cladding CTE mismatch into consideration was developed.

The additivity model assumes that thermo-optic coefficient (TOC = dn/dT) values, among other properties, are known for the glass constituents, one of which will always be silica for the cases described in this Dissertation. The additivity model (law of mixtures) is given most simply as

$$G = \sum_{i=1}^{N} g_i x_i \qquad (2)$$

where x is the additivity parameter of constituent i (such as volume percent), g is the physical property (specifically mass density ρ, refractive index n, dn/dT, etc.) of that constituent, and G is the aggregate multicomponent glass value [6]. The volume fraction occupied by each constituent has been found to be very suitable for use as x (such that $\sum_{i=1}^{N} x_i = 1$) for most calculations. The volume fraction may be rewritten in terms of the usual compositional units, such as molar % or weight % of compound.

While Eqn. (2) is suitable for bulk glass calculations, it does not consider the presence of the fiber cladding. The primary goal in this Chapter is to tailor the core composition to reduce its TOC value in order to study that effect on TMI, while the cladding is assumed to be pure silica. Each of the TOC-lowering materials described above also raises the glass coefficient of thermal expansion (CTE, α). Therefore, since

SiO_2 has a relatively low CTE, thermal expansion of the core is mechanically restricted by a much more massive and voluminous cladding that has a CTE value that is possibly an order-of-magnitude lower. Based on the discussion above, this can have a deleterious impact on the thermal expansion component of the TOC (the negative-valued contribution) and offset the reduction of the core glass TOC relative to the bulk case. To account for this, restriction in thermal expansion is treated as a secondary, positive applied pressure, and therefore the 'cladding effect' can be modeled through the photoelastic effect.

With the correction, the equation governing the refractive index therefore becomes [1] [4]

$$g_i = n_i = n_{0,i} + \frac{dn_i}{dT}(T - T_0) + \frac{dn_i}{d\varepsilon}\frac{d\varepsilon}{dT}(T - T_0) \tag{3}$$

where n_0 is the room-temperature (T_0) refractive index, dn_i/dT is the bulk TOC and the strain (ε) terms are given by

$$\frac{dn_i}{d\varepsilon} = -\frac{1}{2} n_{o,i}^3 \left[2\left(p_{12} - \nu\left(p_{11} + p_{12}\right)\right) + \left(p_{11} - 2\nu p_{12}\right) \right] \tag{4}$$

$$\frac{d\varepsilon}{dT} = -\left(\alpha_{core} - \alpha_{clad}\right) \tag{5}$$

where p_{11} and p_{12} are the Pockels photoelastic coefficients for the individual constituents, and the CTEs (linear) are for the aggregate core or cladding glass. Eqn. (4) accounts for strain in all three primary orthogonal directions. It was recently shown that the additivity model represented by Eqn. (2) is adequate for modeling the CTE as well but requiring correction [7]. In this case,

$$\alpha = \sum_{i=1}^{N} \frac{\alpha_i \rho_i y_i}{\rho} \tag{6}$$

Where, for a binary system ($i = 1,2$ with $i = 2$ representing SiO_2),

$$y_1 = \left(\frac{[1]M_1}{\rho_1 T_1} \right) / \left(\frac{[1]M_1}{\rho_1 T_1} + \frac{[2]M_2}{\rho_2 T_2} \right) \tag{7}$$

in which M is the molar mass, T represents the number of structural units per compound (T_{SiO2},T_{P2O5} = 1 while T_{B2O3} = 2), is the molar concentration (mole%) of constituents 1 or 2, and $y_2 = 1 - y_1$ [1, 2].

As can be seen in Figure 4.3, it is possible, given the selection of dopants, to achieve a fiber with an NA of 0.06 (target) while maintaining the target dn/dT. The top curve shows the refractive index of an early fiber as a function of boria content (for a fixed proportion of B_2O_3 to P_2O_5 and Al_2O_3) at both room (21.5 °C) and elevated temperature (100 °C). The position where the index remains the same is where dn/dT = 0. Although this may represent an impractically high level of B_2O_3 doping, achieving this condition was not a goal of this program. The lower curve shows the effect of cladding the fiber. For the TOC-lowering additives used throughout this program, the cladding has the effect to reduce the effective magnitude of the TOC of the additives. This requires slightly more dopant in the core when the fiber is clad versus unclad (or bulk).

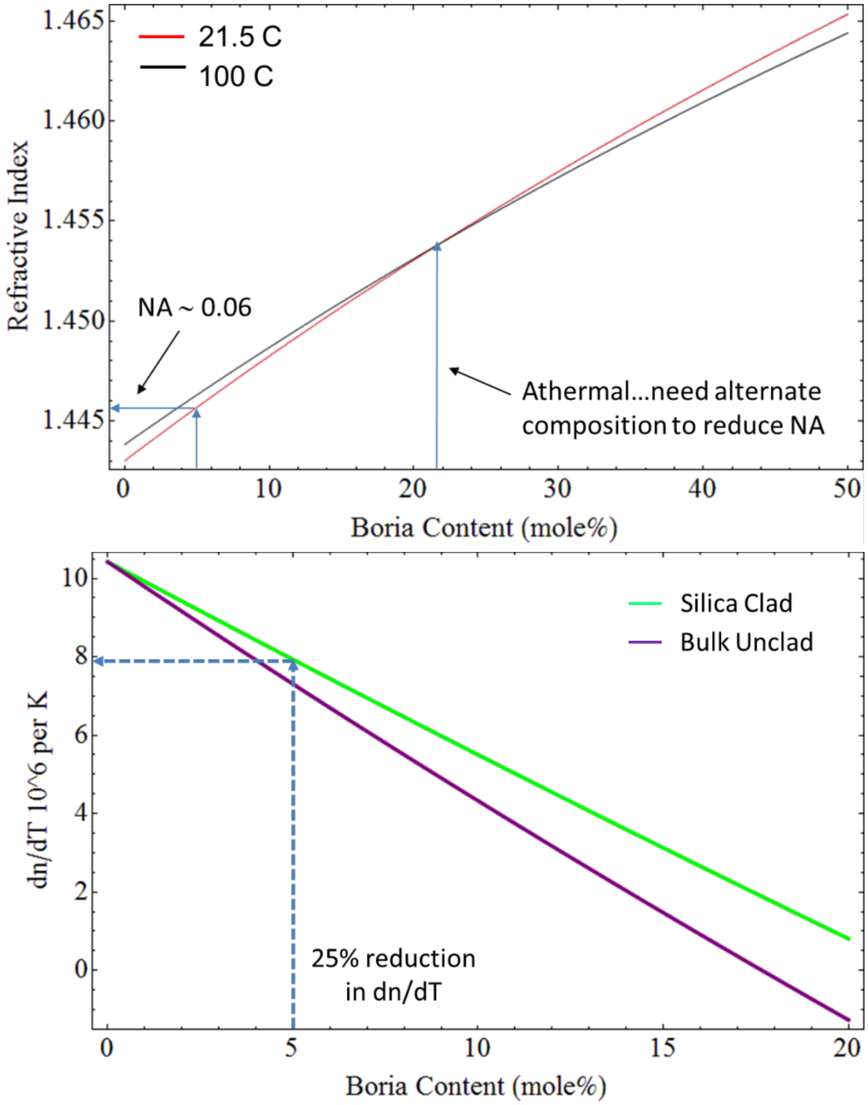

Figure 4.3: Modeled changes in refractive index (top) and thermo-optic coefficient (bottom) as a function of B_2O_3 concentration.

Fibers with a range of boria concentrations were fabricated and tested for their thermo-optic and Brillouin scattering properties. Initial results indicated that glasses in the $B_2O_3 – Al_2O_3 – SiO_2$ system were difficult to form with reasonably high boria concentrations due to the elevated consolidation temperature of the base aluminosilicate glass.

Next, phosphorus pentoxide (P_2O_5) was included in the glass formation in order to improve B_2O_3 incorporation into the glass. P_2O_5 possesses several other advantages including softening the silicate glass thus permitting consolidation at a lower temperature, which reduces B_2O_3 volatilization, reacting with Al_2O_3 in the glass to form $AlPO_4$, which lowers the refractive index relative to SiO_2 (provides compositional flexibility in fiber design), and possessing an intrinsically low thermo-optic coefficient; all of which are beneficial to this project. The initial fiber drawn preform P1 exhibited a dn/dT value 53 % lower than silica, listed in Table I of this Chapter.

4.5 Materials Effect on Brillouin Gain

There are several advantages to the use of the material system described herein, including a reduction in the Brillouin gain coefficient (BGC). This reduction is mainly the result of using boria as a co-dopant, as it increases the acoustic loss due to material absorption as it broadens the Brillouin gain spectrum. Each of the processes contributing to the measured BGC (provided later) in a fiber with target 0.06 NA are summarized as follows:

- Addition of ~ 1 wt% Yb_2O_3 broadens spectra and lowers peak frequency similarly in fibers possessing wide ranges of Al_2O_3, P_2O_5, B_2O_3, and $AlPO_4$.
- B_2O_3 reduces Brillouin gain mainly through large acoustic damping coefficient (broadens the linewidth of the Brillouin gain spectrum or BGS).
- Lower T_{draw} narrows spectrum somewhat, increasing gain. This also is related to the presence of boria in the fiber.

- Spectral broadening is moderate, thereby still allowing the use of phase modulation schemes to reduce the BGC.
- $AlPO_4$ has a p_{12} value comparable to silica, thereby canceling the gain reduction due to the presence of Al_2O_3

4.6 Further compositional change and TOC reduction

Based on the lessons learned and successes of the initial low TOC fibers, the second phase of development to be discussed in this Chapter focused on further reductions to the thermo-optic values as well as ytterbium doping. As with the initial phase of development, a variety of preforms and fibers were fabricated and tested to understand composition, structure, and property relationships.

Initial compositions consisted of ~ 4% Yb with tailored amounts of P_2O_5 + Al_2O_3 (+ B_2O_3) in order to control the NA as well as for reducing dn/dT. Figure 3.2 provides a representative compositional profile of a fiber. Elemental analysis using energy dispersive x-ray spectroscopy (EDX) does not include boron (B_2O_3) and so the precise compositional values are slightly off. Determination of the boria content was extrapolated using Brillouin measurements.

Representative fibers exhibited attenuation vales consistently < 50 dB/km at 1534 nm with a small amount of OH being present in the bottom portion of Figure 4.4. These values are consistent with industry grade fibers.

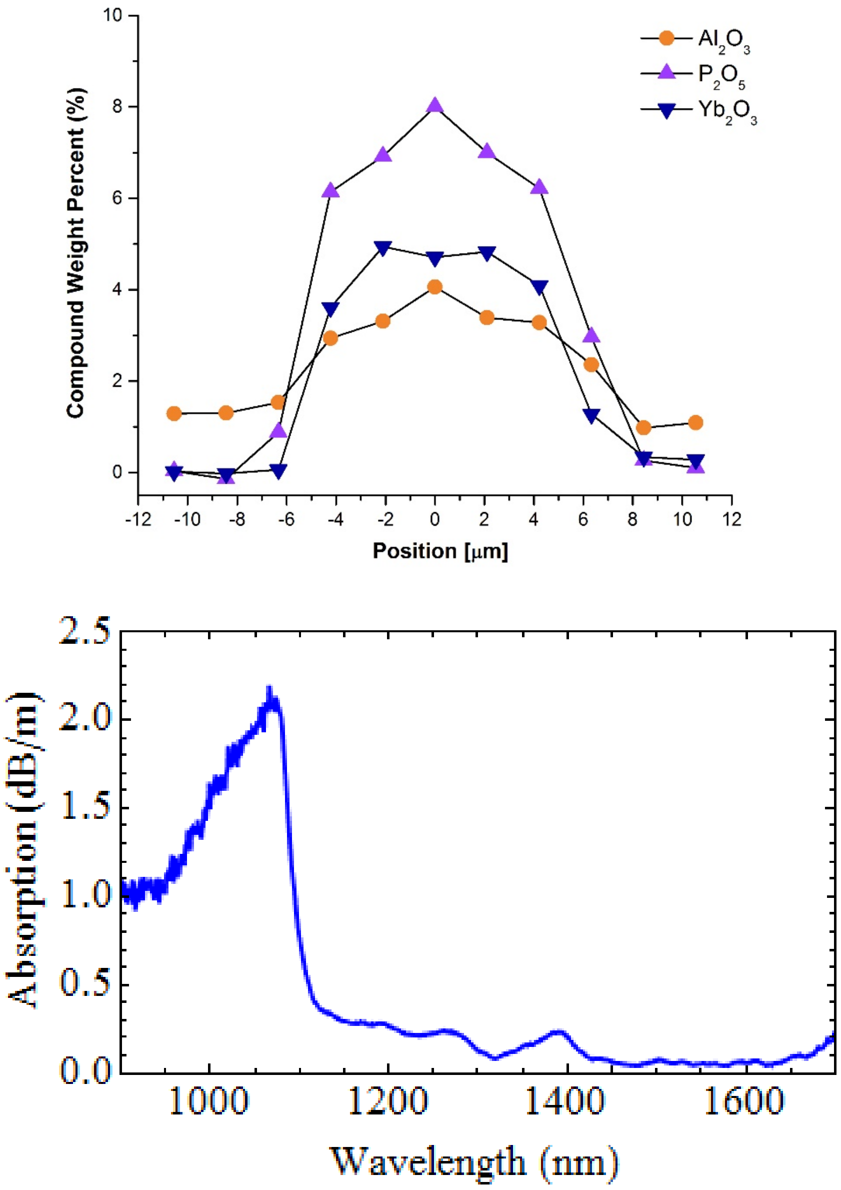

Figure 4.4: (Top) compositional and (bottom) spectral attenuation for representative fibers produced in the second development phase

Fibers were fabricated and studied based on B_2O_3 + $AlPO_4$ concentrations in order to achieve the lowest dn/dT value while maintaining an NA of about 0.06. The best fiber exhibited a measured dn/dT value of 5.5×10^{-6} K^{-1} which is ~ 53% of silica. As a point of reference, the measured dn/dT for a COTS fiber was 9.1×10^{-6} K^{-1}; ~ 12.5% lower than pure silica. A comparison is provided in Figure 4.5, where the free spectral range (FSR) vs temp is plotted. In the case of this fiber versus the COTS fiber, the lower dn/dT fiber, in blue, exhibits a longer slope over a wider temperature range. The material value for the final recipe fiber gives dn/dT = 4.5×10^{-6} K^{-1}, which is ~ 43% of silica. This data supports our strategy of targeting dn/dT materially by composition adjustments and the inclusion and maximizing B_2O_3 content.

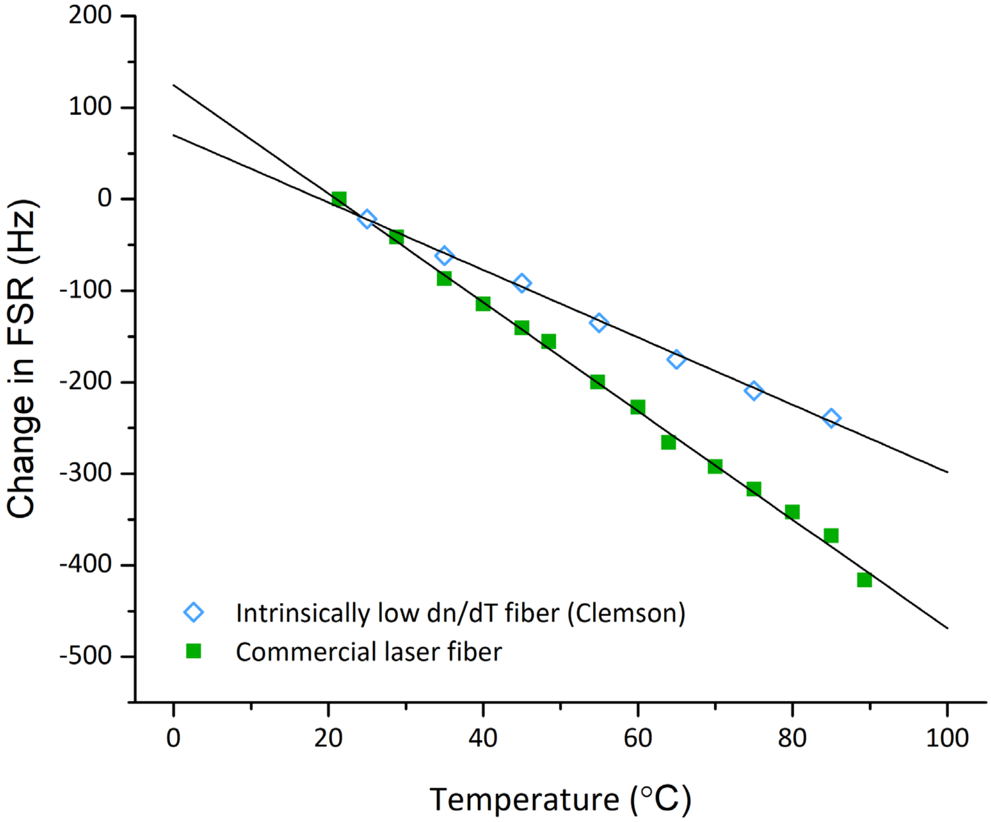

Figure 4.5: Comparison of the thermo-optic coefficient (proportional to the slope) for the program's optimized fiber (blue) and a commercial fiber-laser fiber (green), Laser free spectral range vs temp.

4.7 Brillouin Measurements

Brillouin gain characteristics are plotted in Figure 4.6. The top is from an early phase 2 fiber while the bottom is from the final low TOC fiber fabricated. The top spectrum has two features, the origins of which are currently not understood. The peak at higher frequency likely is due to the core region possessing well-formed $AlPO_4$. The other may be a region of the fiber where the material mainly is P_2O_5 with some boria, but more analysis is needed to confirm. The bottom plot shows the BGS for the final-recipe fiber (measured at 1550 nm). This BGS is much more that which was expected from such a structure, with structure originating with the presence of higher-order acoustic modes (HOAMs) [52]. These modes become significant since the fiber has a substantial central compositional dip usually found with the use of P_2O_5 or B_2O_3. To summarize the measurements and findings:

- Measured BGC = 0.4×10^{-11} m/W at 1534 nm for both fibers. However, the fiber characterized early phase 2 development had anomalous features indicative of an un-optimized fiber
- Brillouin Gain Spectrum has two peaks that decompose into two pure Lorentzian functions peaked at 9.935 GHz and 10.045 GHz with widths of 60 MHz and 125 MHz, respectively. Integrating the spectrum, BGC = $0.5\text{-}0.6 \times 10^{-11}$ m/W for the material due to the overlap of the acoustic mode with a material with varying composition across the core
- As such, lower wavelengths will have BGC closer to the material value.

- The origins of the 2 peaks are currently not known, but probably related to structure in the core and overlap with 2 different acoustic modes.
- From Brillouin, RIP, dn/dT measurements, and B_2O_3 content was estimated using the design curves shown in Figure 4.7.

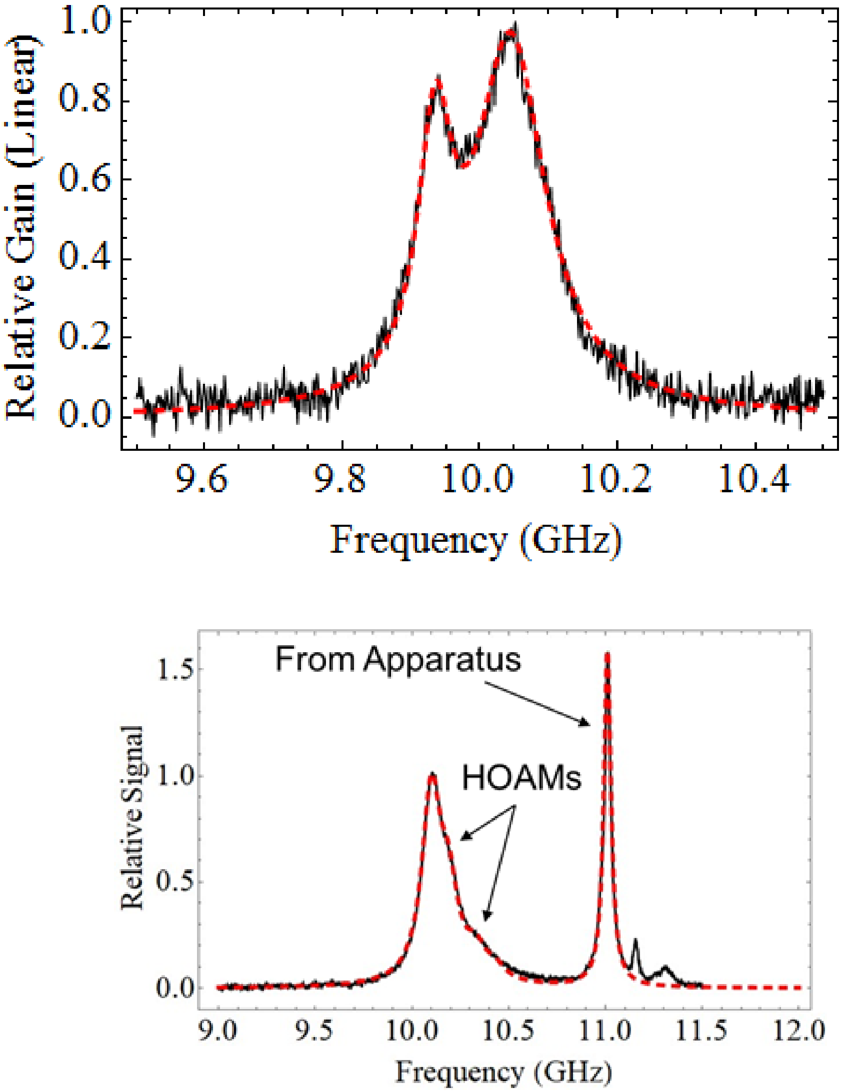

Figure 4.6: Measured BGS for (top) initial composition and (bottom) for the final recipe fiber.

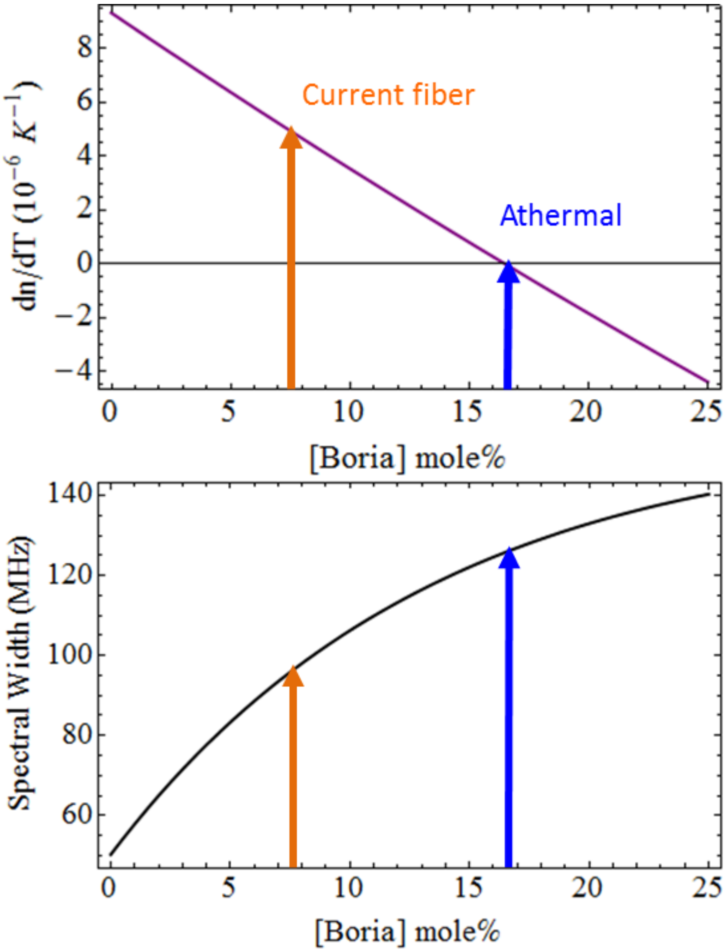

Figure 4.7: (top) dn/dT versus boria content and (bottom) Brillouin spectral width versus boria for the phase 2 compositions.

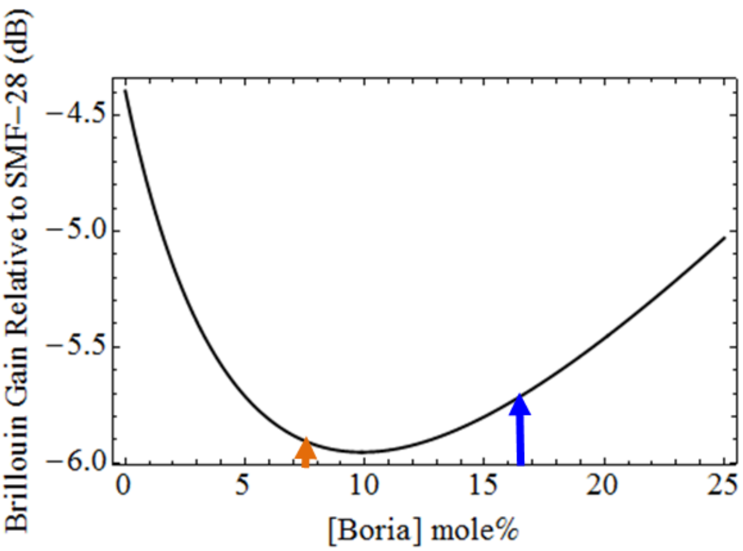

Figure 4.8: Modeled Brillouin gain coefficient as a function of B_2O_3 concentration

Figure 4.8 shows the modeled BGC for the borophosphosilicate (BPS) compositions in the portion related to creation of a fiber to compare to a COTS one. The measurements match well with the model, suggesting the composition is near the absolute minimum BGC value for this material system, where the orange arrow is that of the measured fiber. Interestingly, the composition that gives dn/dT = 0 has a BGC that is somewhat higher than the current fiber. Finally, our measurements gave slightly lower BGC values due to the presence of the structure observed in the fibers, as discussed above.

4.8 Fiberization of Low TOC fiber by Coherent

Though the original preform and fiber that did not compare to the COTS exceeded the reduction of dn/dT by over 50%, further comparison with a COTS fiber was needed. With that in mind, discussions were started with Coherent scientists, and a preform that met the design criteria of intrinsically low thermo-optic and Brillouin gain core glass sent fabricate into an LMA fiber. More specifically:

- Transition intrinsically low dn/dT, Yb-doped core material (1 wt% Yb_2O_3) to double-clad fiber design for high power testing.
- NA – very close to target 0.062
- Coherent will fabricate LMA-YDF-20/400 fiber from this Chapter's core rod for direct comparison with their commercial LMA-YDF-20/400 using our BPS core glass.

In order to achieve the desired properties to replicate the Coherent design with reduced dn/dT materials, a series of process modifications had to be made. The final optimized preform that met the necessary criteria was designated preform P2 (Table I) and shipped to Coherent. This preform was utilized in their fabrication process for our COTS fiber as best effort within their parameters. The entire length of preform was drawn to fiber.

The base composition for preform P1 (Table I) was the "jumping off point" for material research for this fiber. That composition and subsequent fibers based around that have a proven success, as is noted in Chapter 3 regarding active glass development. First, the glass was able to be created via MCVD. This is important so that optical losses can be kept very low such that the influence of the constituent materials are more easily resolved. Second, due to the highly modified composition relative to conventional laser fibers, a significant amount of Yb was able to be incorporated into the glass due to it being an aluminophosphosilicate (APS) base glass [12, 13].

The inclusion of P2O5 is known to reduce photodarkening and to improve solubility of Yb into the host glass composition. [14, 11, 38, 50]. Also due to the creation of the glass via MCVD, B_2O_3 could be readily incorporated into the glass [53]. As previously discussed elsewhere, this was an integral component in the further understanding of the tailorability of the dn/dT of this glass materially. It is also important to make changes to the target Δn to achieve a direct comparison to the COTS fiber. [15]

Compositionally from start to finish, the glass went through some significant changes as discussed in section 4.3. Figure 4.9 illustrates the trend of Yb_2O_3 from the initial glass used in preform P1, to that of the final preform sent to Coherent for drawing, P2. Starting out at around 4% and then reduced to the final target of approximately 1%. The same holds true for Al_2O_3 and P_2O_5 in the glass, which is shown in Table I for both the beginning and final preforms.

One aspect of Materials Engineering related to this glass creation involved the reduction of devitrification in the core of the preform. In Figure 4.10, there are two preforms in the picture. The upper from the end of development of the class composition, and the lower is from the beginning stages of research into the new glass composition. This cloudiness in the core is due to devitrification of the core composition, primarily from phase separation of the Yb_2O_3 in the core. The reason for this phase separation is that, at 2.5 weight percent Yb_2O_3, the system is generally unstable at the elevated MCVD processing temperature. Indeed, per Ref. [55] and [56], there is a liquid-liquid immiscibility in the Yb_2O_3 – SiO_2 system that facilities the observed phase separation even with some co-doping with Al_2O_3 and P_2O_5. Further, this effect is undesirable in the final preform. Reduction of the Yb_2O_3 and the Al2O3 alleviated much of this, however as noted previously, the changes of the composition to improve things such as the devitrification, led to additional changes in the desired refractive index and dn/dT performance by requiring adjustments to the B_2O_3 concentration as well as $AlPO_4$ role in the glass.

Recall that in Chapter 3 on the active glass development, many preforms were fabricated and redrawn together multiple times to reduce any non-uniformities between each unique preform. When the final active glass is created, any differences between each piece is on a smaller scale than the wavelength of light (tens of nanometer scale difference versus pump light of almost 1 μm). For this fiber, only a single preform is fabricated and drawn directly to fiber. This glass composition in particular can be considered highly modified compared to that of a COTS fiber, at least in the initial phases of this research. Very high concentrations of Al_2O_3, P_2O_5 and Yb_2O_3 in the glass core lead to a material that has much lower viscosity to that of its pure silica counterparts [16]. Due to this softening of the glass, the volatile P_2O_5 and B_2O_3 species are more likely to vaporize out of the core region, leaving behind a central “dip” in the refractive index profile.

This highly modified and lower viscosity glass created during MCVD also led to diameter control and straightness issues of the final glass preform. These issues were also mitigated by reduction of Yb and Al from preforms P1 to P2 (Table I) in the glass composition. Simply modifying the rate of collapse and consolidation, along with the concentration changes in the glass composition, while creating a more uniform glass, reduced the dn/dT performance away from the initial values of a 53% reduction as measured in the fibers created from P1.

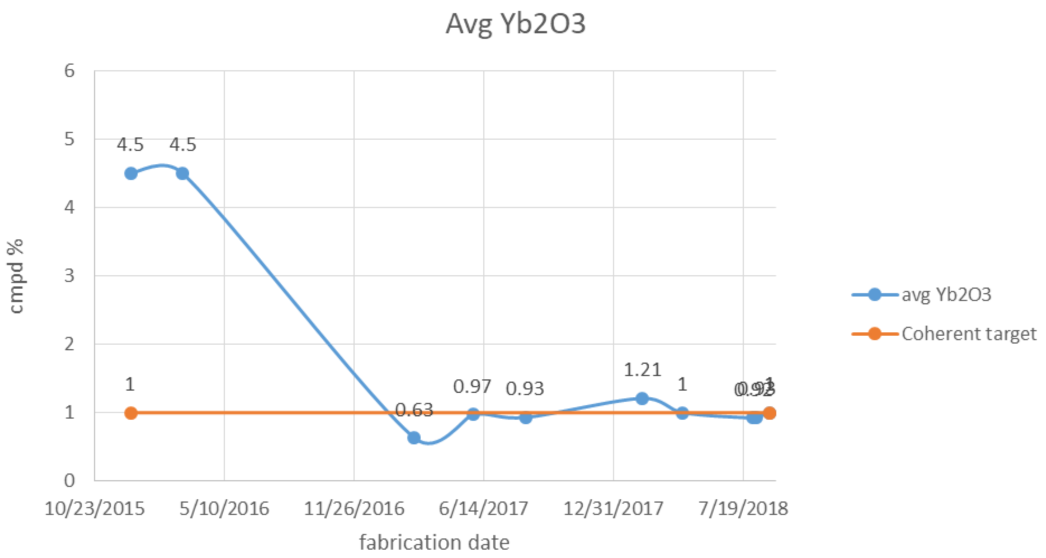

Figure 4.9: Average Yb_2O_3 concentration through process development

Devitrification Improvement

Figure 4.10: Reduction of devitrification in the core region from initial preforms (lower) to final preforms (upper).

Starting from the initial preform P1 to the final preform P2 involved changes in composition, the modifications in the preforms created were driven either by a constraint set forth to compare to the COTS fiber or due to processing variability. The beginning composition originated from the active glass development process (see Chapter 3), and the resultant glass was a combination of many pieces. From a material engineering standpoint, parameters such as ovality, straightness of the final preform, and core devitrification were changed to achieve the characteristics in a single preform necessary to provide clear insights into the materials science of these glasses and fibers. Ovality of the core was decreased along with reduction of the devitrification in the core region of the glass.

Many of the constraints and processing variabilities are interrelated since the influence of the glass constituents on glass stability, viscosity, and optical properties are all connected. Compositional changes such as reduction of Yb_2O_3, a COTS driven constraint, improved the devitrification of the core since lower Yb_2O_3 concentrations in SiO_2 shift the binary composition out of the two-phase liquid immiscibility region [55] [56]. Ovality and straightness of the preform were improved as the composition of the core, particularly the amount of P_2O_5, was reduced. Both of these fabrication properties tie back to the viscosity of the glass during MCVD. Higher P, Al and Yb decrease it, which at the elevated temperatures the substrate tube undergoes during the later stages of MCVD to fully consolidate it, allow for the core to soften and flow. Often this leads to greater ovality and straightness issues as the glass is much softer. Since the Yb and Al were decreased from preform P1 to P2 (Table I), these fabrication properties were mitigated by the compositional change. Of note, however, is that there is still ovality and nonuniformity of the core as seen in Figure 4.14 of the drawn fiber from P2. This is discussed further in the dissertation.

One parameter of note that was targeted by the COTS fiber, when achieved, led to a significant reduction in B_2O_3. Recall that the principal parameter of change for this fiber is reduction in dn/dT in Eqn (3), which is materially driven. In this case, the larger the amount of B_2O_3 in the glass, the greater the effect of reduction of dn/dT will be in the resultant fiber. During MCVD fabrication, the addition of B_2O_3 is performed via vapor phase using BCl_3, as noted in Chapter 2. This inclusion plays two roles is that it a) enables tailoring of the refractive index of the core glass (reduces index relative to SiO_2) and b) facilitates a reduction in dn/dT as well as increasing the Brillouin linewidth, which lead to a reductions in Transverse Mode Instability (TMI) and Stimulated Brillouin Scattering (SBS) [17].

During glass development via MCVD, parameters such as B_2O_3 content are not measured directly, rather they are associated with flows of BCl_3 measured in standard cubic centimeters (sccm). Further, at Clemson there is no direct measurement capability of B_2O_3 in the bulk glass in the Electron Microscope Facility. The initial glass starting with P1 was created using a maximum flow of 100 sccm, which allowed for a positive refractive index of the bulk glass and maximized the potential for dn/dT reduction as it should yield the highest possible amount of B_2O_3 in the final glass. During the continuing research and understanding how the material properties to reduce dn/dT then balance against the constraints set forth by the COTS comparison, many parameters evolved from the beginning glass to the final composition. During that time, the B_2O_3 was reduced in order to achieve a positive Δn by the COTS comparison. A significant amount of time was spent refining and balancing the properties of the glass against these constraints. In total, over 70 different preforms with various changes to the composition or MCVD recipes were created to tailor the dn/dT properties, while also achieving the target constraints set forth by the COTS comparison.

An unanticipated result of these developmental changes arose from the refining of the P_2O_5, Al_2O_3, and B_2O_3 content of the glass. Many preforms were made that met the target Δn of the bulk glass, but as we were focused on learning about the bulk glass composition, structure, and property relationships, and not final fiber properties, a number of preforms did not get drawn to fiber. Only certain ones were deemed suitable to fiberize and evaluate the optical properties and performance. During this portion, it was determined that the set of development parameters that were performing admirably from a bulk standpoint also seemed to meet the criteria for a well-made fiber laser, they were in fact anti-guiding after being drawn to fiber [18].

To illustrate this effect, several preforms were drawn to fiber to evaluate this change in Δn that arose after fiber draw, in order to determine a maximum amount of B_2O_3 that can be added to the glass and still achieve a positive core refractive index. As the B_2O_3 could not be measured directly, a series of preforms with gradually reducing flows of BCl_3 were created then drawn to fiber. The Δn of the bulk glass was measured prior to draw, then the fiber was drawn to a target core size of 20 microns. Once the fiber was drawn, the Δn was measured by Interfiber Analysis using a Transverse Interferometry method.

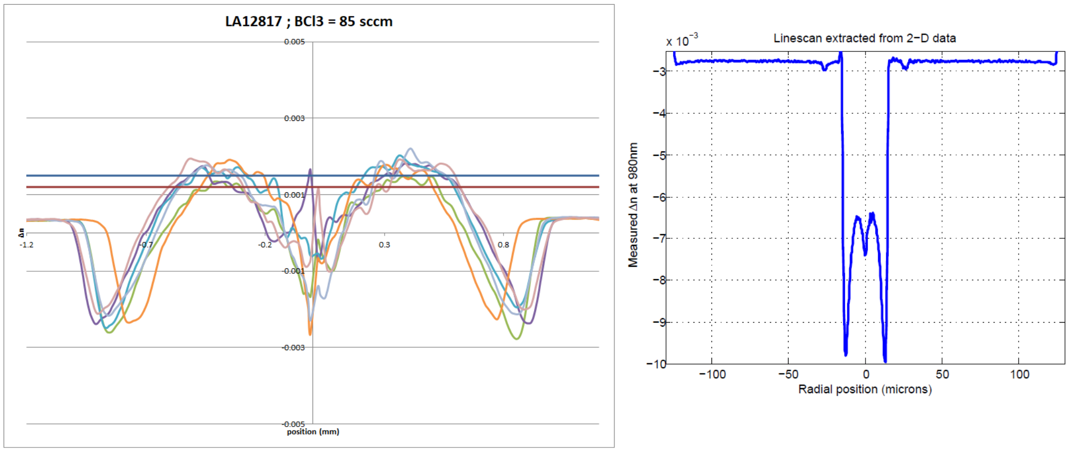

Figure 4.11: Preform LA12817 (left) vs fiber DB22617 (right) RIP comparison.

Looking at Figure 4.11 on the left, is the selection region of the preform chosen for draw into fiber. On the right is the resultant fiber drawn from it, which is DB22617. It is clear that the core region of the preform has a positive Δn, while the resultant fiber does not have a core with a positive index. The entire core region shifted down to a negative Δn when further heat treatment was applied via fiber draw, which is done at 1925°C. This led to a series of preforms being fabricated using identical parameters of creation via MCVD except changes in BCl_3 flows. Materially this is due to the difference in coefficients of thermal expansion of the core versus the clad. The core during draw exhibits lower viscosity due the presence of B_2O_3 and P_2O_5. After heat treatment, or draw, the core is put under stress which changes the index of the glass [57 – 59].

Using two different groups of preform recipes (LA12817 and LA22917 bases respectively), multiple preforms were created with stepwise reductions in BCl_3 flows. These preforms were then characterized and selected regions were drawn into fibers. The LA22917 groups were used for the final preform (LA24018) as this group of bulk preform material achieved the best performance to compare to the COTS fiber based on the maximum possible BCl_3 flows achieved to create a final fiber with a positive Δn. The RIP of the two preform groups are in Figure 4.12 below. The principal difference is that the overall RIP of the LA22917 family are more positive. This is due to increased amount of $POCl_3$, resulting in index-raising P_2O_5, during the collapse and close portion of MCVD preform fabrication.

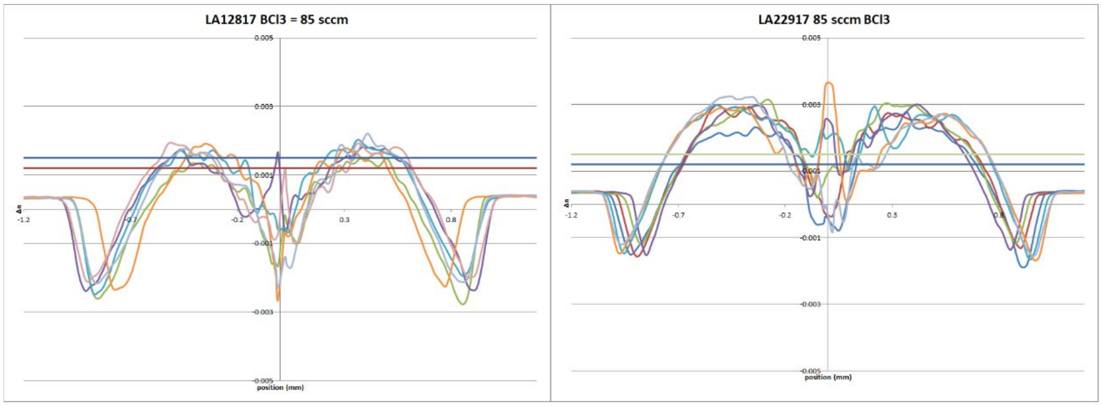

Figure 4.12: Comparison of the LA12817 and LA22917 preform groups or families.

Once the LA22917 family of bulk glass recipes were chosen, the series of preforms were made at differing rates of BCl_3 flows starting at 85 sccm down to 20 sccm. This evolution on the Δn of the fiber is illustrated more clearly in Figure 4.13. From left to right, top to bottom, the core index increases until positive at 20 sccm. The resultant preform after some additional trial and characterization was preform LA24018, was sent to Coherent for fabrication into fiber.

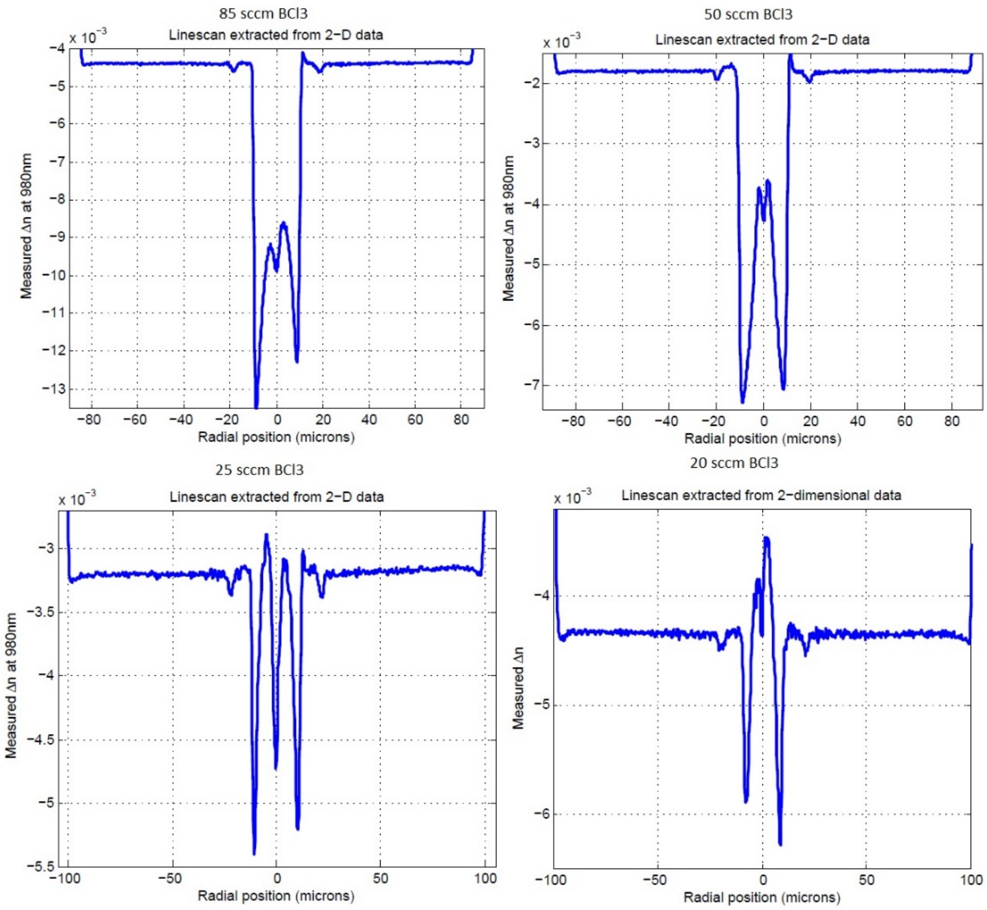

Figure 4.13: Index changes of fibers vs boron flows.

4.9 Fiber Characterization, Performance, and Power Scaling

A total of 762 meters of fiber were fabricated by Coherent using the low TOC final preform P2. This total length was divided into six separate spools of varying lengths. During proof testing after fiber draw, multiple breaks occurred, as the new fiber did not meet the standard manufacturing specification of 100 to 120kpsi by Coherent. The proof testing level was lowered to 68 kpsi and approved by Clemson during the process. Table II lists the spool identification and corresponding length of each.

Spool ID	Fiber Length (meters)
04A	105
08A	215
14A	62
16A	62
17A	123
19A	195

Table 4.2: Spool ID and corresponding lengths for final phase 2 fibers.

Further characterization of the fibers was completed using collaborative partners to fully evaluate the fiber performance. The University of Illinois completed the dn/dT, attenuation, Brillouin, and fiber refractive Index. Fibers were also sent to the (Mid Sweden University, Sundsvall, Sweden) to measure photodarkening of the fibers. Lastly, the Air Force Research Lab (AFRL) completed the power scaling, SBS and TMI threshold measurements.

Samples from all six spools were tested for refractive index profile. Several meters from each spool were tested by Interfiber Analysis using a fiber interferometry technique [8]. The profile of each of the six spools is in Figure 4.14. the most obvious feature is that all but spools 4 and 19 are non-uniform. Not only is it apparent that the shape of the core is not consistently round throughout the length of the fibers, but the refractive index within each core region is not uniform. This index non-uniformity does seem to follow the pattern in the RIP as well, which is readdressed in Figure 4.14. The tip of the preform at 20mm would correspond to spool 4, and the end of the final spool 19 would correspond closer to the 200mm scan position. Using the above fiber RIP, the focus for fiber testing shifted to spools 4 and 19, as they exhibited a more uniform fiber index profile.

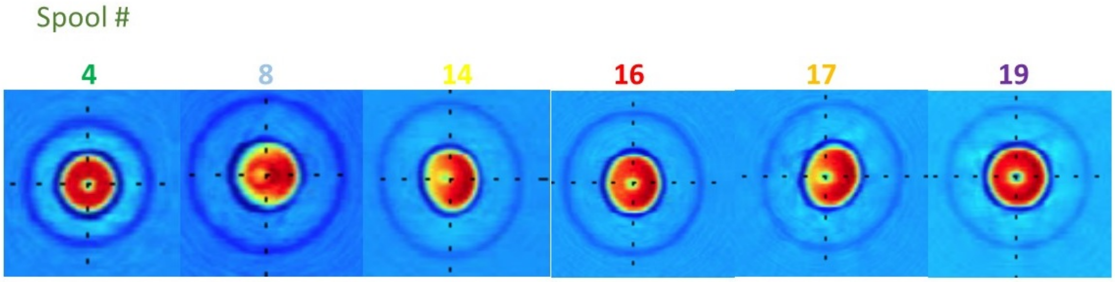

Figure 4.14: Fiber refractive indices.

further analysis of this variability led back to the RIP of the preform itself, which contained variations in both the index and shape at scan positions throughout the preform. Even in the middle, there are anomalous spikes of refractive index, where other positions have a larger dip or burnout of the central region. All these differences were known prior to sending to Coherent. The end goal was to have a full length of fiber, or fibers, fabricated from the entire preform. Once fabricated, the optimal length of fiber would be chosen for further testing. The failure during proof testing seemed to be serendipitous in that a series of discrete spool lengths were received from different regions along the length of the preform. Using the fiber refractive index in Figure 4.14, all but spools 4 and 19 were eliminated from the candidate pool for further test and analysis.

4.10 Fiber Performance and Characterization

Following on the elimination of the spools, the next step was to determine the Mode Field Diameters (MFD) and proximity to the cutoff wavelength for both spools 4 and 19 [9, 10]. Standard MFD calculations were completed at Illinois. Regarding spool 4, guidance was effectively single mode at a wavelength of 1064nm. However, the LP_{01} + LP_{11} modes were very near the cutoff wavelength for guidance, and the MFD was calculated to be 15.7 microns at 1064nm. This would make this spool less useful for power scaling measurements because of the relatively small core size, hence reduced threshold for nonlinearities. For spool 19, the same calculations yield an MFD closer to the commercial counterpart which was the ultimate goal of comparison for this fiber. The commercial fiber from Coherent (LMA-YDF-20/400-VIII) exhibit an MFD of 21.6 μm at 1064nm. These are for modes LP_{01} + LP_{11} + LP_{02} + LP_{20}. For spool 19, those same modes exhibit an MFD of 20.0 μm at 1064nm, which make it an ideal match for further testing against the baseline commercial fiber.

Spool 19 was shipped to Air Force Research Lab (AFRL) for power scaling due to the availability of high-power narrow linewidth sources not available at Clemson or Illinois, their expertise in high power fiber laser systems, and willingness to assist in the research. Spool 19 was further evaluated for the cladding absorption wavelength range, which was forwarded to AFRL for the set up for power scaling. Figure 4.15 indicates the peak cladding absorption at 975nm for this fiber. This value is necessary as the fiber created by Coherent was designed to operate in a double-clad configuration [20, 21]

The majority of current high-power fiber laser systems utilize the double clad configuration of pumping the fibers, and the ones created for this research are no exception. In conventional fibers, the high index core is surrounded by a lower index clad. This lower index cladding glass is then encased in a high index coating. This single clad configuration enables guidance in the core region of the glass as the light is effectively coupled there [22]. In a double clad configuration, however, a lower index outer cladding surrounds the glass clad around the core. This new secondary cladding located on the outside of the fiber laser promotes guidance inside the first cladding, which in this case is glass. This index difference between the outer and now inner cladding operates on the same principals as a single clad fiber, and the difference promotes guidance [23]. Figure 3.18 illustrates these differences. On the left, the cross-sectional guidance mechanisms for cladding pumped fibers are illustrated. On the right, a cross sectional representation of the refractive indices of single clad and double clad fibers are shown in the upper and lower portions, respectively.

The index of the outer cladding is chosen to achieve a specific numerical aperture (NA) which is larger than that of the internal core of the fiber laser. In the case of the fiber created in this research, the core diameter is 20 microns, with an overall final fiber diameter, including the first glass cladding, of 400 microns. In the cases of fibers, especially that of fiber lasers, the NA is a measure of the angle of acceptance of the angle of incident light that will guide within a region of the fiber. This value is based on the refractive index of the materials, typically the core and clad. In the double clad configuration created for this fiber, the target NA of the clad was 0.46 while the NA of the core was approximately 0.06. The benefit of larger NA values for the clad in double clad configurations is improved coupling efficiency of the pump light to the cladding glass. The lower index secondary cladding makes this possible, and it improves the efficiency in which the fiber core can be pumped by enabling a larger area, or greater angle of acceptance, of the incoming pump light [24]. These larger dimensions and double clad configurations have also enabled less efficient stacked diode sources to be used, as well as compensate for poor beam quality from both diode sources and fiber pump sources [25].

This resultant fiber also is considered a Large Mode Area (LMA) design, as well as the COTS comparison fiber. As large clad diameter fibers have become the norm for fiber laser delivery, the increasing need for higher power and shorter lengths also increased. The larger clad configuration enable a larger overall fiber core to be used in the final fiber laser. The fiber design criteria created for this research had a core of approximately 20 microns inside an overall clad OD of 400 microns. By comparison, a singlemode fiber only has a core of approximately 8 microns with a 125 micron fiber OD. A common double clad arrangement is in Figure 4.16

The LMA design enables few mode or single mode operation within a larger OD core in a fiber laser [26]. due to the lower NA of the core versus first inner cladding, the absence of larger number of modes improves power delivery. This also leads to greater power scaling due to higher order mode suppression, as well as the reduction of some optical nonlinearities [27].

The research surrounding this glass and resultant fiber was created with the focus on the active optical component being the rare earth (RE) Yb. This was driven primarily by the focus of modern high-power fiber laser systems using Yb, as well as improved the ability to create a fiber to directly compare to a COTS fiber. Ytterbium ions in silica are readily incorporated via MCVD and solution doping. The Yb system consists of two primary energy levels for the 980 nm upconversion, which is a quasi-3 level transition. The energy level diagram for Yb for the 980nm upconversion and emission is can be seen in Figure 19 [29]. Since this fiber is Yb doped, it is important to understand and verify the peak cladding absorption wavelength, as this is a LMA fiber that is being cladding pumped with a Yb core for lasing. For this fiber, the peak absorption is 975nm, which is optimal for pumping a Yb doped fiber via the cladding.

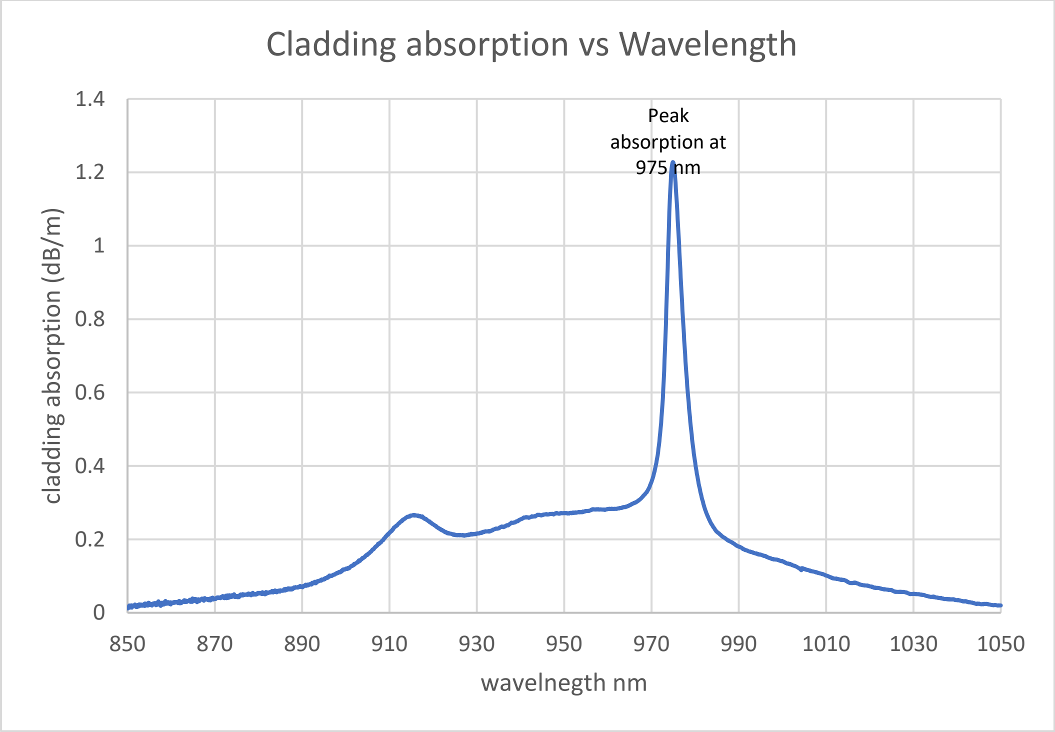

Figure 4.15: Cladding absorption vs Wavelength

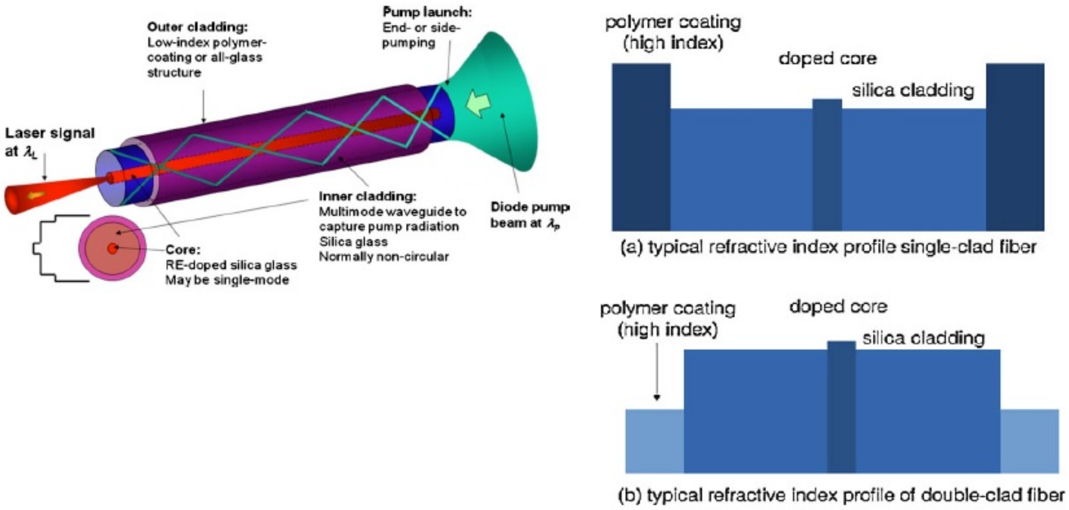

(a) typical refractive index profile single-clad fiber

(b) typical refractive index profile of double-clad fiber

Figure 4.16: Cladding pumped fiber (left); Δn of single vs double clad fiber (right) [12] [19]

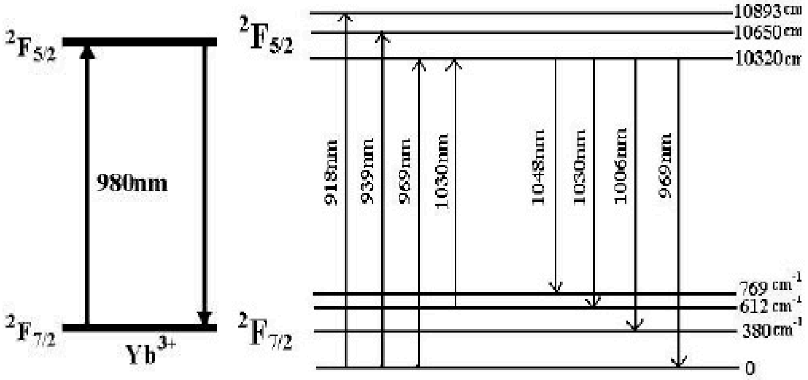

Figure 4.17: Yb “two level” and Stark energy levels [28]

The Brillouin spectra of spool 19 was also measured and the resultant data is in Figure 4.18. For comparison, a commercial fiber was measured to evaluate the change in the Brillouin performance of spool 19 to that of a COTS fiber. The notable features in the plot indicate that the resultant spectra for spool 19 has a Brillouin gain that is both lower and more broad than its commercial counterpart. Both are favorable for high power fiber lasers. For there to be a reduction in SBS, a number of properties can affect it. Density increase of the glass, ρ, will decrease the BGC. Further, what is indicated in Equation 8 for spool 19 is that the spectral linewidth, $\Delta\nu_B$, has broadened, also decreasing the BGC. Lastly, the acoustic velocity V_a, and the Pockels Coefficent p_{12} are both increased and decreased, respectively by Al_2O_3 inclusion in the material (Chapter 1, Table I).

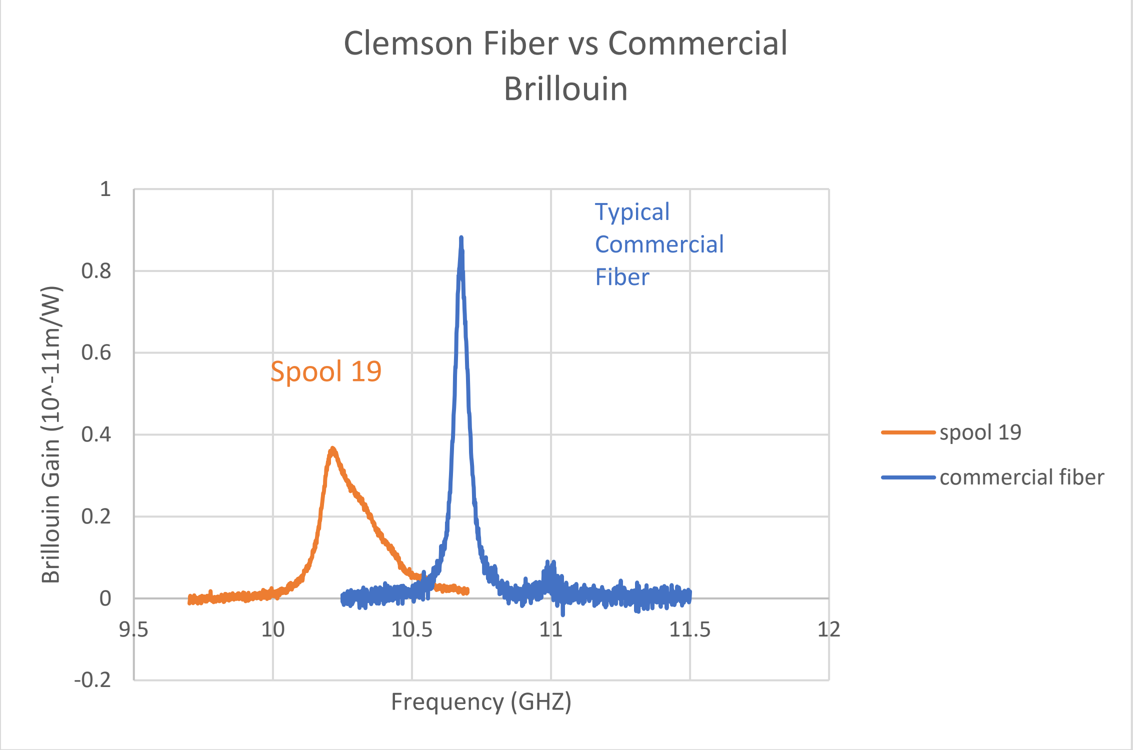

Figure 4.18: Spool 19 Brillouin spectra vs common commercial fiber.

Since further characterization was focused on Spool 19, the optical performance relative to the compositional changes or improvements are all centered around this length of fiber. A primary focus for creating a new fiber with a new composition that can directly change dn/dT, and thus parasitic nonlinearities, is the effect on SBS.

When discussing high power fiber laser systems and their corresponding limitations on maximizing output power, SBS is often of the greatest interest. Of the list of nonlinearities that inhibit power systems, SBS has the lowest threshold of the nonlinearities in narrow linewidth system, such as fiber lasers, which is why it is typically considered the principal limiter on power scaling [1]. In simplest terms, SBS is the generation of an acoustic wave in the opposite direction of the optical guidance within the fiber. The Stokes wave is backward propagating in the fiber, and was discovered in

1964[30]. As it is the lowest threshold of occurrence in the nonlinearities, increases in the threshold yield some of the greatest improvements in fiber laser performance [31].

The primary equation for the Brillouin Gain Coefficient (BGC) is as follows:

$$g_B = \frac{2\pi^2 n^7 p_{12}^2}{c\lambda_p^2 \rho_0 \nu_A \Gamma_B} \qquad (8)$$

Where g_B is the BGC, n is the material refractive index, p_{12} is the photoelastic coefficient, c is the speed of light, ρ is density, υ_A is the acoustic velocity and Γ_B is related to the Brillouin linewidth as $\upsilon_B/2\Pi$ [30, 31]. For spool 19 compared to a COTS fiber in Figure 4.18, the overall spectral range of frequencies is broad, and the full width at half max FWHM is greater than in the COTS fiber. This relates back to the υ_B term in the above equation. As it is inversely proportional to g_B, the reduction is greater in the BGC.

Materially, several properties contribute to this broadening and peak reduction of the Brillouin Gain Spectrum in Figure 4.18. First, the contribution of Al_2O_3 in the glass, along with the development of $AlPO_4$, inhibit the acoustic portion of SBS, thereby increasing the threshold [32, 33]. The further addition of B_2O_3 in the glass to tailor n and to reduce dn/dT has the additional benefit of broadening the linewidth, and the inclusion of Yb_2O_3 as our principal source of lasing, also broadens the spectra [34].

The dn/dT of the fiber was also measured of spool 19. Recall from Section 4.4 of modeling that dn/dT is principal material parameter of this research to reduce these parasitic nonlinearities such as SBS and TMI. By reducing the dn/dT, the thresholds of these parasitics can be further reduced. In this case, there is a reduced Thermo optic coefficient in the regions of doped core, which is favorable for the resultant fiber performance. The connection to the materials in this work is related to Equation (1) where dn/dT is the most effective to target to reduce TMI by increasing the threshold where it occurs. Different materials that combine both positive and negative TOC can be used in a single composition to achieve a significant reduction in dn/dT. Materials that increase it are present in this glass, such as SiO_2 and Al_2O_3. The presence of P_2O_5, $AlPO_4$ and B_2O_3 act to reduce it [1, 33]. As previously mentioned the TOC = dn/dT using the additivity model by Ballato and Dragic.

While SBS threshold reduction is a benefit to the development and understanding of this material as a host for fiber lasers, it is not the initial focus of the materials science for this glass composition. The primary focus is to reduce TMI materially, and by using the thermo-optic coefficient (TOC) or dn/dT, that can be accomplished. Contributing factors to this reduction are the formation of $AlPO_4$ as noted in reference [33]. However, a larger factor for dn/dT reduction is the formation of B_2O_3 in the glass. As noted in [3] the source of TMI primarily comes from STRS during lasing. This is most common in LMA fibers such as the ones created in this work, where the core is sufficiently large as to be multimoded when the power is above a certain threshold [1, 35, 36]

Fiber lasers that use compositions similar to the one created in this work, which is a borophosphosilicate (BPS) fiber doped with Al_2O_3 and Yb_2O_3, are known for exhibiting low photodarkening. The mechanism of photodarkening is a loss of optical power over time as a fiber laser is used. This is particularly an issue in high power system using in CW or continuous wavelength systems. This material feature is most common in fiber lasers doped with Yb, as the effect of photodarkening reduces the lifetime the fiber laser can be used [38]. A key benefit of increasing Yb concentration in a fiber laser is that it reduces the necessary length of the fiber itself to create the laser cavity, reduces the contribution by optical nonlinearities, and reduces the overall size of the final device.[39] However with increased concentrations of Yb comes a higher rate of photodarkening (PD) in double clad fiber configurations, as the power increases. What results as the photodarkening increases is a decrease in output power by the fiber laser over time.

The photodarkening performance of spool 19 was measured by collaborators at Mid-Sweden University. A standard PD test was used and loss over time was measured using a 630nm source, and the fiber was fusion spliced to a standard 125 micron fiber for launch conditions. The PD measurement was done over 100 hours for both fibers.

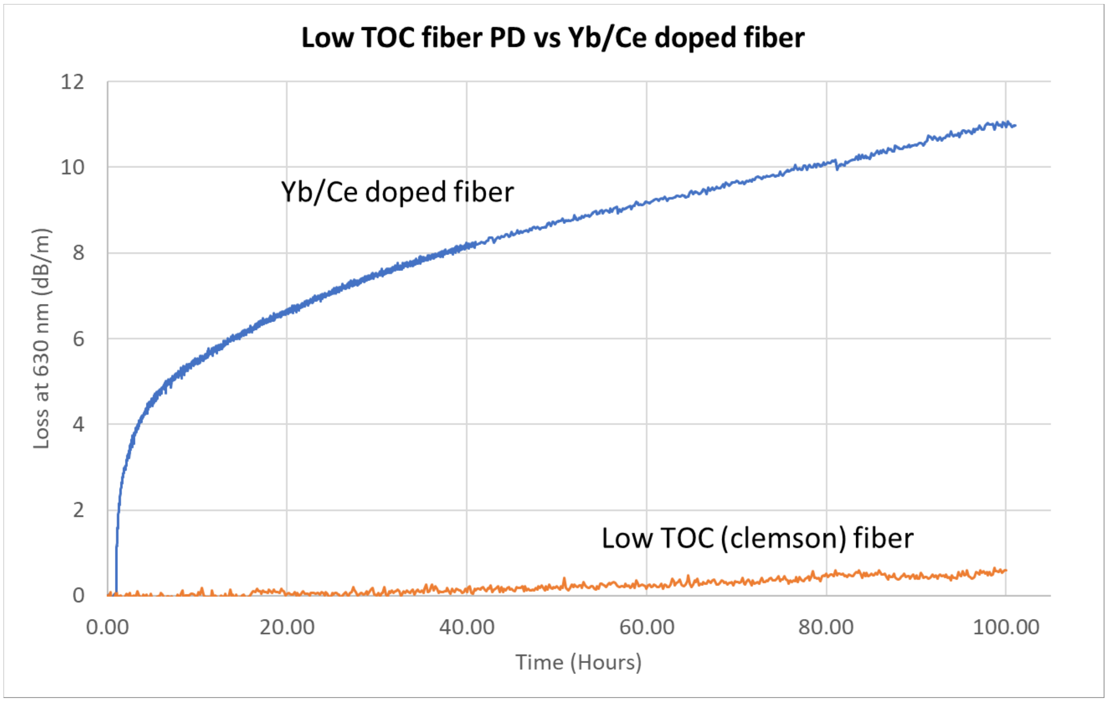

Figure 4.19: Photodarkening measurements spool 19 vs Yb/Ce fiber

For the resultant measurement of Spool 19, the measured spectrum contains more noise relative to the Yb/Ce fiber. This is due to the multimode nature of the fiber and core size, as well as the fact that the losses are very low even for a BPS fiber. Prior to the more accepted use of BPS glass as fiber laser hosts, Cerium doping was common to improve PD over time in Yb fiber laser systems [41]. In this reference, the first author, Engholm, tested the fiber on Spool 19 and compared it to his Yb/Ce doped fiber listed in the publication as a way of comparing the fiber created in this research to a conventional Yb doped fiber laser. What is shown is due to the properties of the BPS glass performance of this composition, the PD is extremely low. The Yb/Ce fiber in Figure 4.19 exhibits higher losses than the BPS fiber of Spool 19 at a maximum of approximately 10 dB/m at 100 hours. By comparison, without the addition of Ce in the host glass for that fiber to mitigate the PD, losses would exceed 300 dB/m with the same concentration of Yb. Photodarkening is further reduced with the including of Al_2O_3 in the host BPS glass, which is present in both fibers, as it increases solubility of the RE and previous research believe it to reduce clustering of the RE ions in the glass [42]. This further supports the research and materials science of the glass created in this work as a beneficial choice of host for high power fiber lasers.

Collaborators at AFRL used the preceding information to optimize the test setup for power scaling spool 19 under optimal conditions. Using the data collected for the various fiber performance characteristics, the power scaled fiber was twelve meters long. The fiber was coiled at 10cm to filter out the higher order modes. What was found during initial testing was that the fiber exhibited multimode performance up to 1040 Watts. At that point, there was strong mode beating, or instabilities, so testing was stopped. Using the provided fiber RIP, an in-house mode field and bend loss solver simulation was performed. That data indicated that even a 6cm coil, the fiber length will not be single mode. The mode solver estimated approximately 5 modes present based on the provided fiber RIP. No instability was seen in the output signal of the fiber laser until approximately 1kW. This instability is currently attributed to HOM interference with the LP_{01} and LP_{11} modes, since there up to 3 additional modes that can be guiding based on the refractive index data. What is also difficult to assess is that since a COTS fiber from Coherent has not been tested under the same conditions, it is difficult to tell that the comparison fiber will have the same issues during power scaling.

Initial scaling tests were completed at a spectral linewidth of 10GHz, but then also narrowed to 5 and 1GHz, respectively. Thermal load on the fiber was measured during the scaling at 10GHz and estimated to be up to 35°C in the fiber at 1kW, while the fiber is being cooled on the plate to mitigate degradation due to thermal load in the fiber. Table 4.3 is a summary of the SBS and TMI Thresholds at the 1, 5, and 10 GHz spectral widths for testing, respectively. TMI is not reached until 1.1 kW at 10GHz, which is lower than expected considering that the fiber always guides 2 modes even when coiled. This higher than expected TMI threshold validates the including of B_2O_3, which reduces the TOC and, as modeled, increases the onset of TMI, as the amount of B_2O_3 in the glass and fiber was maximized when formulating the material. Further, the ability to reach a peak power of 1.1 kW supports the dopant level used of approximately 1% Yb_2O_3 in the glass. Creating a composition around a BPS glass in which the refractive index was tailored to the desired NA and using a double clad fiber design, further enabled the ability to reach higher powers. The NA target was achieved by controlling the amount of Al_2O_3, B_2O_3 and P_2O_5 in the glass.

Spectral Width	**SBS Threshold**	**TMI Threshold**
1 GHz	246 W	Not Reached
5 GHz	868 W	Not Reached
10 GHz	Not Reached	1099 W

Table 4.3: SBS and TMI Thresholds vs power and spectral width.

For the final fiber on spool 19, the lasing efficiency was also measured over the available pump power range. This graph is in Figure 4.20. The resultant fiber exhibits an overall efficiency of approximately 70% overall. This is quite good considering the design constraints, artifacts such as core burnout and asymmetry within the core region.

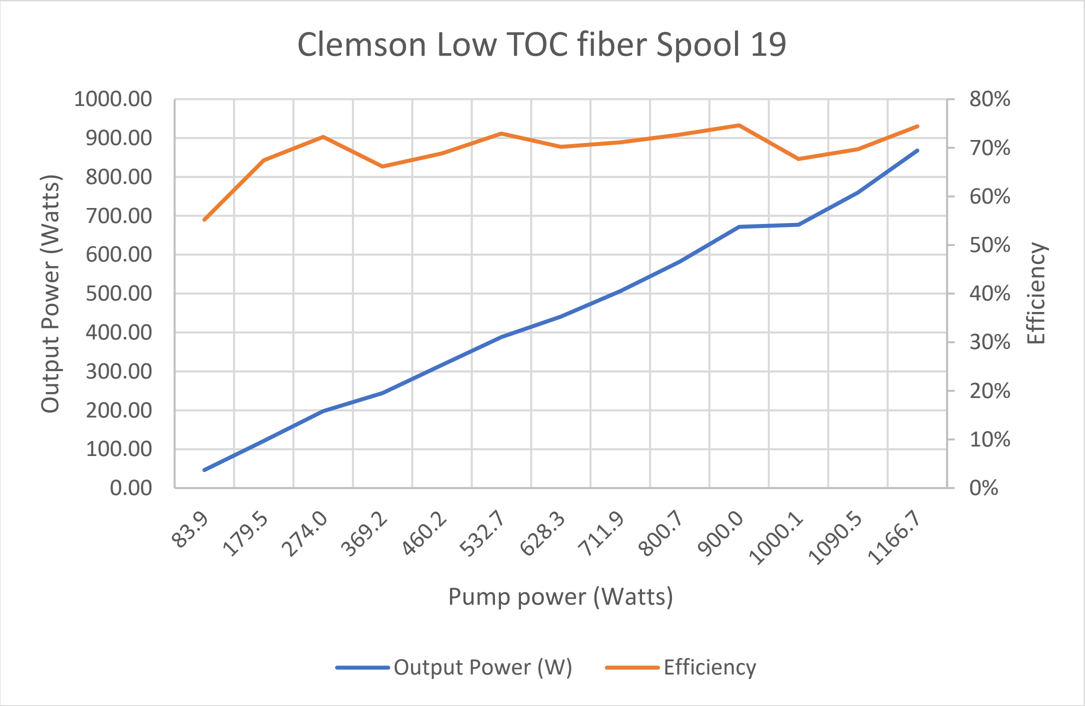

Figure 4.20: Spool 19 Lasing Efficiency

4.11 Summary on Test Results and Development

When the final preform was fabricated and subsequently shipped to Coherent for fiber fabrication, one of the goals for the final fiber was to be as close to a duplication of the target COTS fiber by Coherent (20-400-VIII). The creation of this base composition focused on using Yb and Al doped BPS glass which would achieve in increased TMI threshold given the material improvements and understanding of how

Further goals for this fiber development and understanding were to successfully power scale a single fiber up to 1 kW, which was successful. Along with the power scaling, photodarkening was not observed in any of the fibers that were fabricated, which continues to validate of using a BPS base glass composition for high power fiber lasers [11]. The overall development process yielded a greater understanding of the material interactions between standard fabrication methods of MCVD and the ability to tailor properties of the resultant glass. For example, by modeling the B_2O_3 concentration as well as P_2O_5, an initial glass composition yielded a greater than 50% reduction in dn/dT at 4.5×10^{-6} K^{-1}. A new composition of BPS was created that was able to successfully be fabricated into a fiber via commercial partner collaboration (Coherent). This fiber exhibited a reduced dn/dT, power output of up to 1 kW with approximately 70% efficiency, and no observed photodarkening with standard testing. Compositionally, this is a result of the B_2O_3 in the host glass and fibers, as the dn/dT is proportional to TMI. Higher amounts of boria in the glass, when also coupled with P_2O_5, further drive the onset of the TMI threshold higher. These compositional changes also had the added benefit of reducing SBS in this fiber.

4.12 Future Work

The fiber developed and studied in this Chapter had several constraints placed on the research and material understanding surrounding the compositional development of the glass. This was due to a primary goal of the research to compare the final fiber to a COTS fiber from Coherent. Compromises were made to tailor the material to as closely match that of the Coherent partner fiber.

One of the primary items to focus on is composition. Early preforms contained higher concentrations of Yb, which would improve lasing by allowing for shorter lengths of fibers to be used as the laser cavity. Along with Yb, an increase of both P_2O_5 and B_2O_3 will continue to reduce photodarkening and further reduce dn/dT, respectively. These will continue to reduce the contribution to the parasitic nonlinearities such as SBS and TMI as well. Further research using Raman Spectroscopy to understand the composition in the presence of $AlPO_4$ is also warranted.

A greater focus on reducing processing inconsistencies would also be carried out. One of the major concerns is core burnout in this BPS glass, which is a common issue. Understanding how the burnout reduction in a single preform would also further the overall amount of laser fiber that can be created. In Chapter 3 on active glass composition, this burnout is avoided by multiple stack and draw steps of the core glass. To achieve similar results in a single preform, these issues need to be addressed, along with ovality and straightness of the finished preform. Also, stability of the core glass was addressed for the COTS fiber comparison. Draw knowledge and understanding of the materials developed over the years has shown that a significant amount of phase separation in the core material can be tolerated and still create a useful fiber laser. With this in mind, a “non-uniform” glass may actually be a beneficial fiber if it exhibits the properties desired for a specific fiber laser. Creating a fiber with a larger core diameter and a lower delta n could also mitigate some of the limitations measured of the TMI and SBS thresholds

Regarding the behavior of the fiber as a laser, restrictions in the current fiber that was created may be addressed by the fundamental characteristics. Creating a glass that performs as a fiber laser over shorter lengths will improve characteristics such as the SBS performance. A new glass composition and resultant fiber should exhibit greater control over the core geometry. One issue with the current fibers that were created is that the core is not consistent through the different spools, which is evident in the fiber RIPs that were measured. The increased MCVD understanding and how the fabrication method influences these material properties will benefit new fibers created from the new compositions.

4.13 References

1. J. Ballato, M. Cavillon, and P. D. Dragic, “A Unified Materials Approach to Mitigating Optical Nonlinearities in Optical Fiber. I. Thermodynamics of Optical Scattering” *International Journal of Applied Glass Science* 9, 263 – 277 (2018).
2. A. Smith and J. Smith “Mode instability in high power fiber amplifiers,” *Optics Express* 19, 10180 – 10192 (2011).
3. L. Dong “Stimulated thermal Rayleigh scattering in optical fibers,” *Optics Express* 21, 2642 – 2656 (2013).
4. P. D. Dragic, M. Cavillon, A. Ballato, and J. Ballato, “A Unified Materials Approach to Mitigating Optical Nonlinearities in Optical Fiber. IIA. Material Additivity Models and Basic Glass Properties,” *International Journal of Applied Glass Science* 9, 278 – 287 (2018).
5. P. D. Dragic, M. Cavillon, A. Ballato, and J. Ballato, “A Unified Materials Approach to Mitigating Optical Nonlinearities in Optical Fiber. II. B. The Optical Fiber, Material Additivity and the Nonlinear Coefficients,” *International Journal of Applied Glass Science* 9, 307 – 318 (2018).
6. J. Ballato and P. Dragic, “Rethinking Optical Fiber: New Demands, Old Glasses,” *Journal of the American Ceramic Society* 96, 2675 – 2692 (2013).
7. M. Cavillon, P.D. Dragic, and J. Ballato, “Additivity of the coefficient of thermal expansion in silicate optical fibers,” *Optics Letters* 42, 3650 – 3653 (2017).
8. http://www.interfiberanalysis.com/

9. M. Artiglia, G. Coppa, P. Di Vita, M. Potenza, A. Sharma, “Mode Field diameter Measurements in Single-Mode Optical Fibers”, *Journal of Lightwave Technology*, Vol. 7, No. 8, August 1989.
10. K. Petermann, “constraints for Fundamental-Mode Spot size for Broadband Dispersion-compensated Single Mode Fibres”, *Electronics Letters*, Vol, 19, No. 19, September 1983.
11. M. Engholm, L. Norin, “Preventing photodarkening in ytterbium-doped high power fiber lasers; correlation to the UV-transparency of the core glass”, *Optics Express*, Vol. 16, No. 2, January 200
12. D. J. Richardson, J. Nilsson, W. A. Clarkson “High power fiber lasers: current status and future perspectives”, *Journal of Optical Society of America B*. Vol, 27, No. 11, November 2010.
13. J. Ballato, P. Dragic, “On the Clustering of Rare earth Dopants in Fiber Lasers”, *Journal of Directed Energy*, No. 6, Pg 175-181 Spring 2017
14. S. Suzuki, H. McKay, X. Peng, L. Fu, L. Dong, “Highly ytterbium-doped silica fibers with low photo-darkening”, *Optics Express*, Vol. 17, No. 12, June 2009.
15. H. M. Presby, I. P. Kaminow, “Binary silica optical fibers: refractive index and profile dispersion measurements”, *Applied Optics*, Vol. 15, No. 12, December 1976.
16. G. Vienne, J. Caplen, L. Dong, J. Minelly, J. Nilsson, D. Payne, “Fabrication and Characterization of Yb^{3+} : Er^{3+} Phosphosilicate Fibers for Lasers”, *Journal of Lightwave Technology*, Vol. 16, No. 11, November 1998

17. P. Law, P. Dragic, “Wavelength dependence of the Brillouin spectral width of boron doped germanosilicate optical fibers”, *Optics Express*, Vol. 18, No. 18, August 2010.
18. A. E. Siegman, Y. Chen, V. Sudesh, M. Richardson, M. Bass, P. Foy, W. Hawkins, J. Ballato, “Confined propagation and near single-mode laser oscillation in a gain-guided, index antiguided optical fiber”, *Applied Physics Letters*, 89, 251101, 2006.
19. X. Yu, B. sun, J. Luo, E. Lee, “Optical Fibers for High-Power Lasers”, *Handbook of Optical Fibers*, Springer Nature Singapore Pte Ltd, 2018.
20. H. Po, E. Snitzer, R. Tumminelli, et al, “Double clad high brightness Nd fiber laser pumped by GaAl/As phased array” *Optical Fiber Communication Conference*, Paper #PD7, 1989.
21. E. Snitzer, H. Po, F. Hakimi, R. Tumminelli, B. C. McCollum, “Double Clad Offset Core Nd Fiber Laser”, *Polaroid corporation*, PD5-1, 1988.
22. L. Zenteno, “High-Power Double-Clad Fiber Lasers”, *Journal of Lightwave Technology*, Vol. 11, No. 9, September 1993.
23. J. Senior, *Optical Fiber Communications Principles and Practice, Second Edition*, Prentice Hall, 1992.
24. https://www.nufern.com/pam/optical_fibers/909/LMA-YDF-20/400-VIII/
25. J. D. Minelly, R. I. Laming, J. E. Townsend, W. L. Barnes, E. R. Taylor, K. P. Jedrzejewski, and D. N. Payne, "High-gain fiber power amplifier tandem-pumped by a 3-W multistripe diode," in *Digest of Conference on Optical Fiber Communication*, Vol. 5 of 1992 OSA Technical Digest Series (Optical Society of America, 1992), paper TuG2.

26. L. Dong, B. Samson, *Fiber Lasers; Basics, Technology and Applications*, CRC Press, 2017.
27. L. Dong, F. Kong, G. Gu, T. Hawkins, M. Jones, J. Parsons, M. Kalichevsky-Dong, K. Saitoh, B. Pulford, I. Dajani, “Large-Mode-Area All-Solid Photonic Bandgap Fibers for the Mitigation of Optical Nonlinearities”, *IEEE Journal of Selected Topics in Quantum Electronics*, Vol. 22, No. 2, March 2016.
28. J. He, X. Liang, J. Li, H. Yu, X. Xu, Z. Zhao, Z. Xu, “LD Pumped Yb:LuAG mode-locked lser with 7.63 ps duration”, *Optics Express*, Vol. 17, No. 14, July 2009
29. R. Selvas, J. Sahu. L. Fu, J. Jang, J. Nilsson, A. Grudinen, K. Yla-Jarkko, S. Alam, P. Turner, J. Moore, “High-power, low-noise, Yb-doped, cladding-pumped, three-level fiber sources at 980nm”, *Optics letters*, Vol. 28, No. 13, July 2003.
30. G.P. Agrawal, *Nonlinear Fiber Optics*, (Academic Press, 1995), Ch. 9
31. J. Ballato, P. Dragic, “Glass: The Carrier of Light – A Brief History of Optical Fiber”, *International Journal of Applied Glass Science,* 7 [4]4 413-422, 2016, DOI:10.1111/ijag.12239
32. M. Li, J. Wang, S. Gray, A. Liu, J. Demerrit, A. ruffin, A. Crowley, D. Walton, L. Zenteno, “Al/Ge co-doped large mode area fiber with high SBS threshold”, *Optics Express*, vol. 15, No. 13, 2007
33. N. Yu, T. W. Hawkins, T. Bui, M. Cavillon, J. Ballato and P. D. Dragic, "AlPO4 in Silica Glass Optical Fibers: Deduction of Additional Material Properties," in *IEEE Photonics Journal*, vol. 11, no. 5, pp. 1-13, Oct. 2019, Art no. 7103913. doi: 10.1109/JPHOT.2019.2941487

34. P. D. Dragic, "Brillouin Gain Reduction Via B $_{2}$O $_{3}$ Doping," in *Journal of Lightwave Technology*, vol. 29, no. 7, pp. 967-973, April1, 2011. doi: 10.1109/JLT.2011.2107502
35. Arlee V. Smith and Jesse J. Smith, "Mode instability in high power fiber amplifiers," *Optics Express* 19, 10180-10192 (2011)
36. Jauregui, C., Limpert, J. & Tünnermann, A. High-power fibre lasers. *Nature Photon* 7, 861–867 (2013) doi:10.1038/nphoton.2013.273
37. M. Cavillon, C. Kucera, T. Hawkins, J. Dawson, P. Dragic, J. Ballato, “A unified material approach to mitigating optical nonlinearities in optical fiber. III. Canonical examples and materials road map.” *International Journal of Applied Glass Sciences*. 2018; 9: 447- 470.
38. M. Engholm, L. Norin, “Preventing photodarking in ytterbium-doped high power fiber lasers; correlation to the UV-transparency of the core glass”, *Optics Express*, vol. 16, No. 2, 2008
39. Bertrand Morasse, Stéphane Chatigny, Éric Gagnon, Carl Hovington, J-Philippe Martin, J-Philippe de Sandro, "Low photodarkening single cladding ytterbium fiber amplifier," *Proceedings SPIE 6453, Fiber Lasers IV: Technology, Systems, and Applications*, 64530H (20 February 2007); https://doi.org/10.1117/12.700529]
40. R. Paschotta, J. Nilsson, P. Barber, J. Caplan, A. Tropper, D. Hanna, “Lifetime quenching in Yb-doped fibres”, *Optics Communications*, Vol. 136, Issue 5-6, pg 375-378

41. M. Engholm, P. Jelger, F. Laurell, and L. Norin, "Improved photodarkening resistivity in ytterbium-doped fiber lasers by cerium codoping," *Optics Letters* 34, 1285-1287 (2009)
42. T. Haruna, J. Iihara, K. Yamaguchi, Y. Saito, S. Ishikawa, M. Onishi, T. Murata, "Local structure analyses around Er3+ in Er doped fiber with Al co-doping," *Optics Letters*, 14 (23), 11036-11042 (2006)
43. P. Dragic, M. Cavillon, J. Ballato, "Materials for optical fiber lasers: A Review", *Applied Physics Reviews*, 2018.
44. T. Hawkins, J. Ballato, P. Dragic, "A Unified Materials Approach to Mitigating Optical Nonlinearities in Optical Fiber. IV. Opportunities for Vapor Phase Processing" (publication in process)
45. D. DiGiovanni, J. MacChesney, T. Kometani, "Structure and properties of silica containing aluminum and phosphorus near the $AlPO_4$ join:, *Journal of Noncrystalline Solids*. 1989;113:58-64.
46. L. Dong, F. Kong, G. Gu, T.W. Hawkins, J. Parsons, M. Jones, C. Dunn, M.T. Kalichevsky-Dong, K. Saitoh, B. Pulford, and I. Dajani, "Large mode area Yb-doped photonic bandgap fiber lasers," *SPIE Photonics West*, *invited talk*, paper 9344-1, San Francisco, February 2015
47. G. Gu, F. Kong, T. Hawkins, J. Parsons, M. Jones, C. Dunn, M.T. Kalichevsky-Dong, K. Saitoh, and L. Dong, "Ytterbium-doped large-mode-area all-solid photonic bandgap fiber lasers," *Optics Express* 22, 13962-13968(2014).

48. F. Kong, G. Gu, T.W. Hawkins, J. Parsons, M. Jones, C. Dunn, M.T. Kalichevsky-Dong, B. Pulford, I. Dajani, K. Saitoh, S.P. Palese, E. Cheung, and L. Dong, "Polarizing ytterbium-doped all-solid photonic bandgap fiber with ~1150μm2 effective mode area," *Optics Express* 23, 4307-4312 (2015).
49. B. Pulford, T. Ehrenreich, R. Holten, F. Kong, T.W. Hawkins, L. Dong, and I. Dajani, "400 W near diffraction-limited single-frequency all-solid photonic bandgap fiber amplifier," *Optics Letters* 40, 2297-2300 (2015).
50. G. Gu, Z. Liu, F. Kong, H. Tam, R.K. Shori and L. Dong, "Highly efficient ytterbium-doped phosphosilicate fiber lasers operating below 1020nm," *Optics Express* 23(14), 17693-17700 (2015).
51. F. Kong, G. Gu, T.W. Hawkins, M. Jones, J, Parsons, M.T. Kalichevsky-Dong, S.P. Palese, E. Cheung, and L. Dong, "Efficient 240W single-mode 1018nm laser from an Ytterbium-doped 50/400μm all-solid photonic bandgap fiber," *Optics Express* 26(3), 3138-3144 (2018).
52. P. Dragic, P. Law, Y. Liu, "Higher Order Modes in Acoustically Antiguiding Optical Fiber", *Microwave and Optical Technology Letters*, Vol. 54, No. 10, October 2012.
53. S. Wemple, D. Pinnow, T. Rich, R. Jaeger, L. Van Uitert, "Binary SiO2 – B2O3 glass system: Refractive index behavior and energy gap considerations", *Journal of Applied Physics*, Vol. 44, No. 12, December 1973
54. B. Hatta, M. Tomozawa,,"Effect of Al_2O_3 on phase separation of SiO_2-Nd_2O_3 glasses", *Journal of. Non-Crystal Solids* 354, 3184 (2008).

55. Y. Murakami, H. Yamamoto, “Phase Equilibria and Properties of Glasses in the $Al_2O_3 – Yb_2O_3 – SiO_2$ System”, *Journal of the Ceramic Society of Japan*, 101, 1993.
56. H. Yamamoto, K. Akiyama, T. Hirata, Y. Murakami, “Dependence of Yb_2O_3/SiO_2 Molar Ratio on High-Temperature Characteristics of Gas Pressure Sintered Si_3N_4”, *Journal of the Ceramic Society of Japan*, 113, 2005
57. R. Sammut, P. Chu, “axial Stress and its Effect on Relative strength of Polarization-Maintaining fibers and Preforms”, Journal of Lightwave Technology, Vol. 3, No. 2, 1985
58. C. Kim, Y. han, B. Lee, W. Han, U. Paek, Y. Chung, “Induction of the refractive index change in B-doped optical fibers through relaxation of the mechanical stress”, Optics Communications, Nov. 2000
59. K. Brugger, “Effect of Thermal Stress on Refractive Index in Clad Fibers”, Applied Optics, Vol. 10, No. 2, 1971

CHAPTER FIVE

CONCLUSIONS AND FUTURE WORK

5.1 Conclusions

The purpose of this Dissertation was to study the material science and engineering necessary to create high power fiber lasers from Yb-doped aluminophosphosilicate glasses. In that goal, we were successful. Both processes (materials engineering) and compositions (materials science) were thoughtfully developed based on the understanding gained leading to the realization of active and low nonlinearity fibers via MCVD.

Using the material properties and known commercial methods of vapor phase deposition, in excess of 100 preforms were fabricated and thoroughly studies in terms of composition and select physical and optical properties that exhibited uniform composition and refractive index profiles. These materials were made active using approximately 1 wt% Yb in all cases. The compositions were judiciously tailored to exhibit a refractive index closely matched the refractive index of silica despite having, in some cases, quite extreme compositions. This was achieved through studying and understanding how dopants into silica, such as Al_2O_3, P_2O_5, and B_2O_3 influence, both individually and collectively (e.g., $Al_2O_3 + P_2O_5 \rightarrow AlPO_4$) the index in a way that still affords a high degree of accuracy in the bulk preform. Further, understanding the behavior of the formation of $AlPO_4$ allowed for predictive control over the index. These oxides were also found to exhibit favorable characteristics needed for high power fiber laser applications, such as low photodarkening and improved solubility of rare earths into the glass.

Using rigorous criteria for material and optical selection, based on the understanding of glass composition, structure, and properties, a series of optimized preforms were created, stacked, and drawn into a cane. This process was shown to allow for the mitigation of variations of composition and index between the preforms to be reduced to a scale below the wavelength of the intended pump and signal light. This allows for the material to appear optically uniform to the light propagating in the fiber. Using the developed active glass (AC1), a laser fiber was created and evaluated in order to understand the interplay between core composition, fiber design, and laser performance. However, this glass did not exhibit the desired composition, rare earth concentration, and, most importantly, target refractive index. This was found to be due to variations during the stack and draw process as well as compositional shifts that further reduced the index and diluted the core with additional silica, thus reducing overall Yb concentration in the active core glass.

Following this testing and optical characterization, which confirmed the lower concentrations and refractive index, respectively, a new compositional goal was created, based on understanding composition / property trends, to compensate for the Yb concentration and low refractive index difference. New bulk preforms were fabricated using the same rigorous characterization criteria for the composition and index. Once created, these preforms underwent the same stack and draw process. This new active glass (AC2) was also characterized. The new Yb concentrations in the composition exhibited high lasing performance with the ability to be scaled in excess of 400W with single-frequency bean quality in a single fiber. B_2O_3 was shown not only to lower the refractive index of the glass, but also to facilitate a more uniform profile in the final AC2 glass. This is due to its effect on the host glass by lowering viscosity as well as index. The material understanding of how to create and tailor $AlPO_4$ in the AC2 glass further increased the uniformity and control of the refractive index. Also, using the properties of the Al_2O_3 and P_2O_5 to lower the immiscibility barrier and improve Yb solubility into silica, considerable increases the doping level was achieved, while also creating a stable glass that could be drawn multiple times into canes and fibers.

Using the knowledge and understanding gained during the research for the active glass in chapter 3, the resultant preform composition and material properties, such as the ability to include high concentrations of Yb for lasing, and B_2O_3 for the reduction of dn/dT, were the ideal inroad to create a glass that exhibited low optical nonlinearities in a high-power fiber laser by using the material properties to mitigate them.

The creation of the low thermo-optic base composition focused on using Yb and Al doped into a boro-phospho-silicate (BPS) glass for achieving increased TMI threshold. The overall development process yielded a greater understanding of the material interactions between standard fabrication methods of MCVD and the ability to tailor properties of the resultant glass. For example, by modeling the B_2O_3 concentration as well as P_2O_5, an initial glass composition yielded a greater than 50% reduction in dn/dT at $4.5 \times 10^{-6}\ K^{-1}$. This new BPS composition, which was studied and developed for low thermo-optic and other (e.g., Brillouin) nonlinearities, was fabricated and sent to a commercial partner (Coherent), who fabricated a double clad fiber replicating once of their commercial fibers (20-400-VIII).

This fiber, with core composition developed through this Dissertation and drawn into a double clad configuration by Coherent, was power-scaled to Defense-relevant levels (> 1 kW) by collaborators at the Air Force Research Laboratory (Albuquerque, NM). Testing these fibers at > 1 kW was a goal of this Dissertation since, at these levels, the full picture becomes clear as to the relationship between glass composition, fiber design, and laser performance. Along with the power scaling, photodarkening was not observed in any of the fibers that were fabricated, which continues to validate of using a BPS base glass composition for high power fiber lasers [11]. This fiber exhibited a reduced dn/dT, power output of up to 1 kW with approximately 70% efficiency, and no observed photodarkening with standard testing. Compositionally, this is a result of the B_2O_3 in the host glass and fibers, as the dn/dT is proportional to TMI. By reducing the concentrations of Yb, and Al, and using the properties of B_2O_3 in the borophosphosilicate glass, the TMI threshold, an optical nonlinearity, can be increased materially. This will lead to higher lasing powers by using material science and understanding of the properties of the glass to mitigate this and other parasitic nonlinearities. Higher amounts of boria in the glass, when also coupled with P_2O_5, further drive the onset of the TMI threshold higher. These compositional changes also had the added benefit of reducing SBS in this fiber.

5.2 Future Work

With regard to the further development of advanced active glass compositions, the next steps include increasing the Yb content of the host glass to > 6 wt%, which will double the best efforts in our research thus far, as long as this does not detrimentally influence photodarkening or parasitic upconversion. This will necessitate understanding the limits of both increases in Al_2O_3 and P_2O_5 doping into the silica as well. Further, the Δn boundaries are increased to higher level, so the new glass should achieve a Δn at 0 relative to silica. New methods of characterization are also to be implemented which will reduce the number of preforms required for fabrication. This new material understanding, as well as can be used to change the properties to mitigate these nonlinearities and improve lasing powers and efficiencies in fiber, can be included in future glass research. These new characteristics of research include using Dragic's additivity model to predict the optical performance of the glass based on compositional criteria and bulk measurements. Heat treatment and intermediate draws will also be included to evaluate the Δn of the preform prior to stack and draw to reduce variability in the final index of the active core material. Steps are also going to be taken to further reduce the amount of silica cladding around the active core, which will improve Δn uniformity in the final glass. These include acid etching to reduce the clad layers of the ground cores, as well as intermediate etching steps between stack and draw steps.

Materially, the understanding of the behavior of the glass and dopants to form a stable glass can be applied to other rare earths to create new active core materials. Thulium is the largest area of new materials research regarding fiber lasers. This active glass composition is suited to incorporate larger concentrations than what has currently been shown in silica via MCVD. Further, the unique approach of stack and draw to scale down the material differences between preforms, thus making the active glass appear optically uniform, has not, to our knowledge been completed.

This active glass also has the capability to be an exact index match to silica, making it possible to use in a variety of new fiber laser designs. Using the knowledge gained from these Yb doped materials, and how the incorporation of excess silica during stack and draw is vital to future success. New ways to increase the dopant concentration, or reduce dilution, must be used. Further, a deeper understanding of the behavior of B_2O_3 and $AlPO_4$ in the glass during further heat treatments via stack and draw, need to be quantified. These materials also require a further study into their effect on final compositions and dopant levels during creating of the preforms.

Additionally, the fibers created for and studied for the mitigation of optical nonlinearities placed several constraints on the research and material understanding surrounding the compositional development so as to allow for comparison to modern industrial standards of fiber lasers. Without these boundary conditions for future research, several possibilities open up.

One of the primary items to focus on is composition. Early preforms contained higher concentrations of Yb, which would improve lasing by allowing for shorter lengths of fibers to be used as the laser cavity. Along with Yb, an increase of both P_2O_5 and B_2O_3 will continue to reduce photodarkening and further reduce dn/dT, respectively. These will continue to reduce the contribution to the parasitic nonlinearities such as SBS and TMI as well. Research not presented in this Dissertation, but that has built upon the work, is indicating that composition is exhibiting properties of laser cooling [1]. This is an exciting potential for future generations of fiber lasers, as heat is a limiting factor or the catalyst for limitations on power scaling due to thermally induced nonlinearities. A new fiber that both mitigated heat and had higher threshold onset of TMI or SBS is an exciting potential area of research!

A greater focus on reducing processing inconsistencies would also be carried out. One of the major concerns is core burnout in this BPS glass, which is a common issue. Understanding how the burnout reduction in a single preform would also further the overall amount of laser fiber that can be created. In Chapter 3 on active glass composition, this burnout is avoided by multiple stack and draw steps of the core glass. To achieve similar results in a single preform, these issues need to be addressed, along with ovality and straightness of the finished preform. Also, stability of the core glass was addressed for the commercially-off-the-shelf (COTS) fiber comparison. Draw knowledge and understanding of the materials developed over the years has shown that a significant amount of phase separation in the core material can be tolerated and still create a useful fiber laser. With this in mind, a "non-uniform" glass may actually be a beneficial fiber if it exhibits the properties desired for a specific fiber laser. Creating a fiber with a larger core diameter and a lower Δn could also mitigate some of the limitations measured of the TMI and SBS thresholds. Further research using Raman spectroscopy will also be used to increase the material understanding of the compositions that exhibit high concentrations of $AlPO_4$.

Regarding the behavior of the fiber as a laser, restrictions in the current fiber that was created may be addressed by the fundamental characteristics. Creating a glass that performs as a fiber laser over shorter lengths will improve characteristics such as the SBS performance. A new glass composition and resultant fiber should exhibit greater control over the core geometry. One issue with the current fibers that were created is that the core is not consistent through the different spools, which is evident in the fiber RIPs that were measured. The increased MCVD understanding and how the fabrication method influences these material properties will benefit new fibers created from the new compositions.

5.3 References

1. J. Knall, P. Vigneron, M. Engholm, P. Dragic, N. Ju. J. Ballato, M. Bernier, M. Digonnet, “Laser cooling in a silica optical fiber at atmospheric pressure” *Optics Letters,* 2020.